Shape Coexistence and Collectivity in Neutron-Deficient Mercury Isotopes

Thesis submitted in accordance with the requirements of the University of
Liverpool for the degree of Doctor in Philosophy, by

Andrew Petts

Oliver Lodge Laboratory
Department of Physics

September 2010

This thesis is dedicated to Philippa Marley. A constant source of inspiration.

I feel nothing but pride; thats all I do feel. An empty pride, a hopeless vanity, a dreadful arrogance, a stupefyingly futile conceit... but at least its something to hang on to.

- Peter Cook as Sir Arthur Streeb-Greebling in Why Bother?

Abstract

Recoil Distance Doppler Shift measurements of ^{182}Hg have been performed at the University of Jyväskylä utilising the Köln plunger device. Lifetimes of excited yrast states up to the 10^+ state have been measured. The 2^+, 4^+, 6^+, 8^+ and 10^+ states were found to have lifetimes of 41(3) ps, 35.7(15) ps, 8.2(5) ps, 2.9(3) ps and 1.2(3) ps respectively. The high collectivity of the states with $I^\pi \leq 4^+$ indicate their prolate deformed character. In ^{182}Hg the 2^+ yrast state was deduced to be a strong admixture of the coexisting prolate and oblate structures.

Coulomb excitation measurements of ^{182,186}Hg performed at REX-ISOLDE using the MINIBALL HPGe array examine the quadrupole moment and transitional matrix elements associated to the 2^+_1, 2^+_2 and 4^+_1 states in ^{182}Hg and the 2^+_1 state in ^{186}Hg. The spectroscopic quadrupole moment of the 2^+_1 state in ^{182}Hg measured -0.45 eb, indicating prolate deformed character. Conversely, the 2^+_1 state in ^{186}Hg was found to be oblate from the spectroscopic quadrupole moment of +1.74 eb. Transitional matrix elements for both ^{182}Hg and ^{186}Hg were found to be in agreement with those from lifetime measurements.

Acknowledgements

I would like to firstly show my gratitude to Professor Peter A. Butler for his supervision of this thesis and allowing me the opportunity to participate in his experimental program.

The post-doctoral research fellows I have been fortunate enough to have at my disposal I owe my deepest thanks to. First of all Dr. Marcus Scheck for his constant advice, input and friendship during the Coulex analysis and his proof-reading of this thesis. His strict adherence to the Reinheitsgebot is admirable, though misguided! An extra thankyou for the blutwurst. Secondly Dr. Tuomas Grahn for his tutoring in the methods of lifetime analysis and allowing me the chance to analyse my first data set.

Mr Liam Gaffney I thank for his hard work on the 'other' Hg nuclei and questions which made me think "is this correct?"

Dr. David Joss deserves thanks for proof-reading this work and making vital suggestions.

Dr. Jarno van der Walle and Dr. Emmanuel Clement I thank for guidance on the analysis of the Coulex data and my initial MINIBALL training.

Dr. Nigel Warr I thank for his part in my MINIBALL training and his help with GOSIA problems.

My gratitude to the Warsaw group for the GOSIA training they provided. In particular Dr. Magda Zielinska who has throughout my PhD answered many GOSIA related questions and helped my reach my "Eureka!" moment with the code.

A special thankyou to my family, in particular my mother, who have always been proud and never expectant. Finally I would like to say a massive thankyou to the woman who this thesis is dedicated to.

Contents

List of Figures

List of Tables

Chapter 1

Introduction

The periodic table of elements currently lists 118 elements based upon the number of protons they possess. The elements are arranged in such a way as to group certain elements with common properties together. For example, if one looks to group 8 in the periodic table, elements known as the Nobel gases are listed. These elements are all inert and contain a full outer electron shell configuration. Elements listed in group 1 of the periodic table, the alkali metals, all contain an outer electron shell housing a solitary electron and are extremely reactive with water, forming hydroxides. It is the configuration of electrons into discrete shells that predominantly give an element its chemical properties.

Each element listed in the periodic table has isotopes, nuclei possessing the same number of protons but a differing number of neutrons. Approximately 300 of these isotopes are stable. This is only a small fraction of the 3000 plus nuclei that have been observed in the laboratory and an even smaller fraction of the number of predicted nuclei. Figure 1.1 shows observed and predicted nuclei represented schematically in accordance to proton and neutron number much in the same way as the periodic table. Just like the periodic table certain regions of the nuclear chart have certain common observable properties. If one heads towards the proton drip line, that is the theoretical line defined by the proton separation energy being equal to zero one will observe the phenomenon of proton emission. Going to the other side of the chart to the neutron drip line - defined

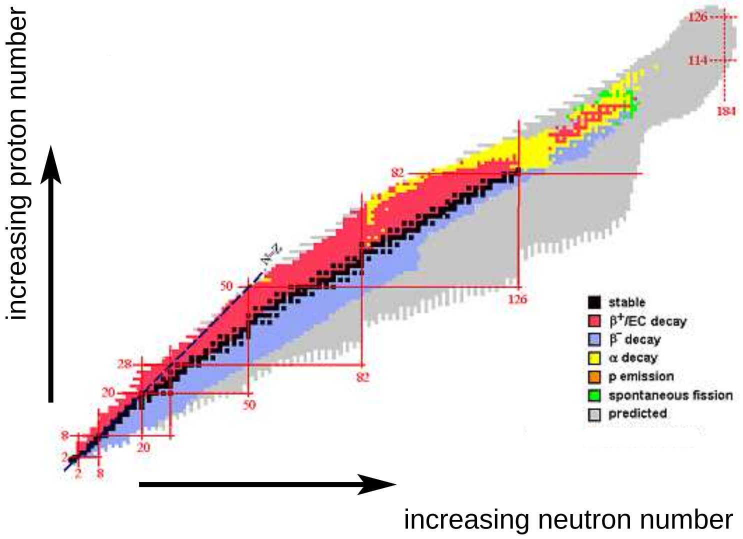

Figure 1.1: Schematic representation of the nuclear chart. Shell closures are numbered and indicated with a red line. [Pau]

by the neutron separation energy being equal to zero one will observe phenomena such as neutron halos and neutron skins. When one looks in regions of the nuclear chart where a nucleus lies near a closed proton or neutron shell, a so-called magic number, a near-spherical shape to the nucleus will be observed. Analogous to the electron configuration being the predominant factor in chemical properties, it is the configuration of the nucleons in discrete energy shells that give a nucleus certain observable properties and behaviours. Of particular interest in this thesis is how the configuration of the constituent nucleons in the discrete energy shells plays a significant role in the resulting macroscopic shape of the nucleus.

With radioactive ion beam facilities such as REX-ISOLDE now well established a much larger proportion of these nuclei are accessible for experimental study. This opens up the possibility to observe and study a wide range of nuclear phenomena, including shape coexistence, in regions of the nuclear chart that were previously inaccessible and to test the nuclear models that predict such phenomena.

1.1 Nuclear Properties and Models

The atomic nucleus consists of subatomic particles know as protons and neutrons. These particles are confined to a minuscule radius of $\approx 10^{-15}$ m. The proton has a positive charge and the neutron is charge neutral. A strong nuclear force must bind the nucleus together to overcome the repulsive effects of the Coulomb interaction between protons.

It is understood that the strong nuclear force acts over a short range. With the size of nuclei being so small and the effects of the strong force neglegable at the atomic scale a short range force is the only reasonable conclusion. The size of a nucleus can be estimated to be approximately $\mathrm{R} = \mathrm{R_0 A^{1/3}}$ which can give a good estimate of the range of the strong nuclear force. R_0 is taken to be 1.2 fm and A represents the atomic number of the nucleus under consideration.

With the observation that the mass of an atomic nucleus is less than the sum of its constituent parts, evidence for a saturated force can be inferred. The 'missing mass' of the nucleus is equated to the binding energy of the nucleus. Binding energy is defined as the energy required to separate the nucleus completely into individual protons and neutrons. A plot of binding energy per nucleon as a function of mass can be seen in many texts, for example [Kra88]. The well-known plot reaches a maximum around ^{56}Fe and then flattens to an approximate value of 8 MeV. This is clear evidence that the strong nuclear force saturates. The strong nuclear force would continue to increase with mass number if this were not the case.

Evidence for a shell structure to the nucleus, comparable to the shell structure of electrons in an atomic system, can be obtained from the separation energies for different nuclei. The proton separation energy, *S(p)*, is defined as the energy required to remove one proton from the nuclear volume to infinity. Similarly the neutron separation energy, *S(n)*, is defined as the energy required to remove one neutron from the nuclear volume to infinity. If one were to increase the number of neutrons with respect to the number of protons for a certain nucleus *S(n)* would decrease and *S(p)* increase. If one were to decrease the number of neutrons with respect to the number of protons for a certain nucleus *S(p)* would decrease and *S(n)* increase. Certain numbers of protons and neutrons in a nucleus cause a dramatic increase in separation energy. These numbers are *2,8,20,28,50,80,126* and are known as *magic numbers* and represent a full, closed shell.

The shell model has been most successful in predicting properties such as level energies for nuclei near closed shells where a spherical nucleus is observed. For nuclei in the mid-shell regions of the nuclear chart where more deformed structures reside nucleon-nucleon interactions cannot be described by a mean field approximation and the shell model breaks down. A macroscopic viewpoint must be taken to describe the collective effects observed for these mid-shell nuclei. In the proceeding sections properties and models relating to the onset of deformation are discussed with the intention of leading to a discussion of shape coexistence in the light mercury region of the nuclear chart.

1.1.1 Deformation

The general shape of a nucleus can be expressed in terms of spherical harmonics according to the equation

$$R(\theta,\phi) = c(\beta_\lambda)R_0\left[1 + \sum_{\lambda=1}^{\lambda=\infty}\sum_{\lambda=-\mu}^{\lambda=\lambda}\alpha_{\lambda\mu}Y_{\lambda\mu}(\theta,\phi)\right], \tag{1.1}$$

where R(θ,ϕ) represents a radius vector from the origin to the surface, R$_0$ is the radius of a sphere which has equal volume to the nucleus. The factor c(β_λ) ensures volume conservation, $\alpha_{\lambda\mu}$ is the deformation parameter and $Y_{\lambda\mu}(\theta,\phi)$ a spherical harmonic of order λ, with λ classifying the multipole order. $\lambda = 1$ corresponds to a dipole, $\lambda = 2$ corresponds to a quadrupole and $\lambda = 3$ corresponds to an octupole. For quadrupole deformation Equation 1.1 becomes

$$R(\theta,\phi) = c(\beta_\lambda)R_0\left[1 + \sum_{\mu=-2}^{2}\alpha_{2\mu}Y_{2\mu}(\theta,\phi)\right]. \tag{1.2}$$

When the principle axis are made to coincide with the nuclear axis the five coefficients reduce to two as $a_{22} = a_{2-2}$ and $a_{21} = a_{2-1} = 0$. The standard parameters

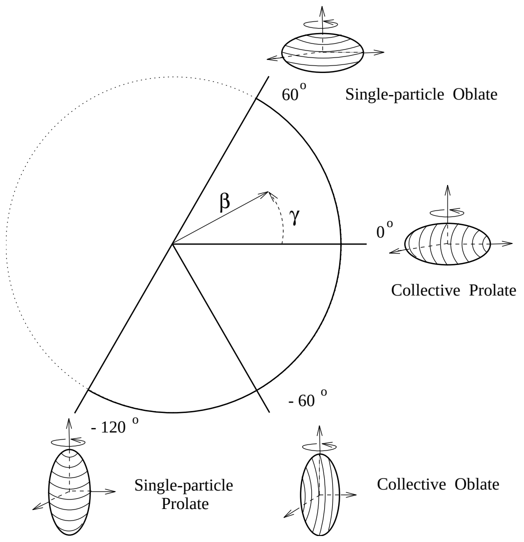

Figure 1.2: Resulting nuclear shapes for deformation parameters β and γ using the Lund convention.[Pau]

to describe quadrupole deformation are thus

$$\begin{aligned} a_{20} &= \beta \cos \gamma \\ a_{22} &= \frac{1}{\sqrt{2}} \beta \sin \gamma \end{aligned} \tag{1.3}$$

where β is a measure of the deviation from the surface of a sphere and γ is a measure of the deviation from axial symmetry.

A common convention to describe the range of shapes for $\lambda = 2$ in terms of the β and γ variables is the Lund convention [ALL$^+$76]. Figure 1.2 shows the various shapes that result from quadrupole deformation and places them in the (β - γ) plane. In this convention the relationship between β, γ and the nuclear radii can be observed from the change in nuclear radius in Cartesian coordinates as a function of β and γ. The increments along the three principle axis are defined as

$$\begin{aligned} \delta R_1 &= R_0 \sqrt{\frac{5}{4\pi}} \beta \cos\left(\gamma - \frac{2\pi}{3}\right), \\ \delta R_2 &= R_0 \sqrt{\frac{5}{4\pi}} \beta \cos\left(\gamma + \frac{2\pi}{3}\right), \\ \delta R_3 &= R_0 \sqrt{\frac{5}{4\pi}} \beta \cos \gamma. \end{aligned} \tag{1.4}$$

Or when taken together

$$\delta R_k = R_0\sqrt{\frac{5}{4\pi}}\beta\cos\left(\gamma + \frac{2\pi}{3}k\right) \qquad k = 1, 2, 3. \tag{1.5}$$

From this convention it can be stated that if $\gamma = 0$, then $\mathrm{R}_1 = \mathrm{R}_2$. If R_3 is then less than R_0 the nucleus will be *oblate*. If R_3 is greater than R_0 the nucleus will be *prolate*.

1.1.2 Rotation

With a deformed nucleus rotation is a possible form of collective excitation. This is not possible with a spherical nucleus as any rotation about an axis of symmetry produces results which are indistinguishable. To a first approximation the energy associated with rotational excitation of a nucleus can be calculated classically. The classical formula for the energy of a rotating rigid body states

$$E = \frac{1}{2}\Im\omega^2 \tag{1.6}$$

where $\Im$ is the moment of inertia and ω the rotational frequency. With the rotational frequency being related to the moment of inertia by the formula

$$\omega = \frac{I}{\Im}, \tag{1.7}$$

where I is the total angular momentum, consisting of the rotational angular momentum, $\vec{R}$ of the nucleons about the axis of symmetry and the individual intrinsic angular momentum of valance nucleons, $\vec{J}$ such that

$$I = \vec{R} + \vec{J}. \tag{1.8}$$

Equation 1.6 then becomes

$$E = \frac{I^2}{2\Im}. \tag{1.9}$$

For a quantum mechanical system $I^2 = \hbar^2 I(I+1)$ so that Equation 1.9 becomes

$$E = \frac{\hbar^2}{2\Im}I(I+1). \tag{1.10}$$

This gives a characteristic pattern to the energy levels and a useful experimental signature for rotational bands being the ratio of the $E_{4^+}/E_{2^+} \approx 3.33$.

For a spherical rigid body the moment of inertia is defined as

$$\Im_{rig} = \frac{2}{5}MR^2, \tag{1.11}$$

where M is the mass of the rigid object and R the radius of the rigid object. Allowing the nuclear radius to be $R = R_0 A^{\frac{1}{3}}$ the rigid moment of inertia for a spherical nucleus is therefore

$$\Im_{rig} = \frac{2}{5}A^{\frac{5}{3}} m_n R_0^2, \tag{1.12}$$

where R_0 is 1.2 fm, A the number of nucleons and m_n the mass of a nucleon. Apply this to an ellipsoidal shape the moment of inertia can be expressed as

$$\Im(\varepsilon) \approx \left(1 + \frac{3\varepsilon}{4}\right)\Im(sphere), \tag{1.13}$$

where ε is the eccentricity of the ellipsoid. The moment of inertia defined in the above equations is a *static* moment of inertia. With the nucleus being only an approximation to a rigid body, the true values for the moment of inertia are often considerably less than the rigid body value [Cas90]. The nucleus is usually considered a rigid core surrounded by valence nucleons. With this description in mind two moments of inertia must be defined to fully describe the rotation of the nucleus. When one assumes maximum alignment on the x-axis so that $I_x \approx I$ The *kinematic* moment of inertia can be defined as

$$\Im^{(1)} = \left(\frac{dE}{dI_x}\right)^{-1}\hbar^2 = \hbar\frac{I_x}{\omega} \tag{1.14}$$

and the *dynamic* moment of inertia as

$$\Im^{(2)} = \left(\frac{d^2E}{dI_x^2}\right)^{-1}\hbar^2 = \hbar\frac{dI_x}{d\omega} \tag{1.15}$$

with the kinematic moment of inertia being due to the motion of the system and the dynamic moment of inertia a response of the system to an external force. The transition energy in a rotational band can be related to the kinematic moment of inertia through Equation 1.10 producing the relation

$$E_\gamma = \frac{\hbar^2}{2\Im}(4I - 2) \tag{1.16}$$

and the dynamic moment of inertia related to the difference in consecutive γ rays though the equation

$$\Delta E_\gamma = \frac{4\hbar^2}{\Im^{(2)}}. \tag{1.17}$$

1.1.3 The Liquid Drop Model

With the knowledge that the nuclear force is a strong, attractive force within a short range and repulsive at distances below ~ 0.7 fm analogies with the behaviour of molecules in a liquid can be made. The Van der Waals interactions between molecules in a liquid exhibit the same properties of a short range attractive force with a repulsive core. This leads to the simplest collective nuclear model, the liquid drop model. The liquid drop model reproduces certain nuclear properties by comparing the nucleus to a non-rotating, charged liquid drop. A liquid drop in the absence of external fields will adjust its shape to that of a sphere and minimise the surface tension energy. The liquid drop is assumed to be incompressible and therefore the density remains constant regardless of radius. The model assumes a short range attractive force that becomes repulsive at shorter distances. Surface nucleons are assumed to be less bound as the number of interacting neighbour nucleons is diminished. The key result from this approximation to the nuclear force is the semi empirical mass formula or the Weizsäcker formula for total nuclear binding energy [Wei35]

$$B(Z, A) = a_v A - a_s A^{\frac{2}{3}} - a_c \frac{Z^2}{A^{\frac{1}{3}}} - a_A \frac{(A - 2Z)^2}{A} + \delta(Z, A), \tag{1.18}$$

where Z is the number of protons and A the total number of nucleons. Energy is expressed in units of MeV. It can be seen that the first term on the right hand side in the Weizsäcker formula represents the volume energy. As the nuclear force saturates nucleons only interact with neighbouring nucleons causing the

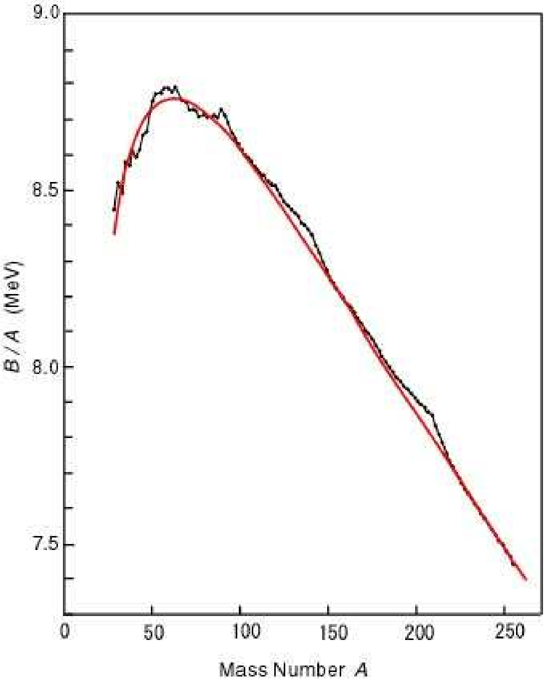

Figure 1.3: Binding energy as a function of A. Solid red line represents theoretical values from the Weizsäcker formula whilst black circles represent experimentally obtained values for binding energy.[Rea]

binding energy to be proportional to the nuclear volume. The second term is the surface term. This corrects the volume term for the fact that not all nucleons are surrounded equally. The number of nucleons near the surface of the liquid drop will be proportional to the surface area and will be surrounded by fewer nucleons than those nearer the centre. The third term that corrects the volume term is the Coulomb term. As the protons in the nucleus are charged there is an electrostatic potential that must be resolved. The Coulomb term must be subtracted from the volume term to account for the natural repulsion that occurs due to the protons having the same charge. The next term in the Weizsäcker formula is the symmetry term. This term is a consequence of the Pauli exclusion principle and is sometimes referred to as the isospin term. It expresses the charge-symmetric nature of the nucleon-nucleon force which has the consequence that in the absence of a Coulomb potential the most stable configuration for a nucleus is N=Z. The final term in the Weizsäcker formula is the pairing term. Nucleons prefer to form spin zero pairs in the same spatial state to minimise energy. An increase in binding energy occurs due to the overlap of the spatial wave functions. This leads the nucleons to be in closer approximation and therefore within the range of the nuclear force for a greater period of time. The value of δ is dependent on the make-up of the nucleus and is different for odd-odd, even-even and odd-even nuclei giving

$$\delta = \begin{cases} +a_p A^{-\frac{4}{3}} & even - even \\ 0 & even - odd \\ -a_p A^{-\frac{4}{3}} & odd - odd \end{cases}$$

Even-even nuclei therefore have an increased stability due to the pairing term.

With the Weizsäcker formula being semi-empirical A and Z dependencies are derived from theory but the coefficients are experimentally defined. Typical values for the coefficients are listed below

$$\begin{aligned} \mathrm{a}_v &\approx 15.8\,\mathrm{MeV} \\ \mathrm{a}_s &\approx 18.0\,\mathrm{MeV} \\ \mathrm{a}_c &\approx 0.72\,\mathrm{MeV} \\ \mathrm{a}_A &\approx 23.5\,\mathrm{MeV} \\ \mathrm{a}_p &\approx 34\,\mathrm{MeV}. \end{aligned}$$

It can be seen in Figure 1.3 that with these coefficients the theoretical values are in good agreement with experimental measurements. Some values deviate slightly at certain mass values indicating a more fundamental description is required. The values where the deviation is strongest are around values such as A=208, A=132, A=100, A=56 etc. These are the masses of doubly magic nuclei i.e nuclei with both closed proton and neutron shells. The binding energy plot therefore indicates a shell-like structure to the nucleus. As this model is almost entirely classical it is no surprise that quantised energy levels are not reproduced fully with this method.

1.1.4 The Nuclear Shell Model

Due to the limitations of the liquid drop model a new description and understanding of the nucleus is required. The shell model describes the nucleus as a series of shells that nucleons occupy, much in the same way as electrons are ordered in an atomic system. It attempts to explain the phenomena such as the the discrepancy in binding energies and two particle separation energies observed at certain nuclear masses. In short it attempts to explain the magic numbers. The liquid drop model fails in this respect.

The shell model uses a *mean field* force to explain the nucleon interactions. The basic assumption of the shell model is that a nucleon moves in a potential which is the average of the effect of all other nucleons and varies smoothly. The nuclear potential is then

$$V_i(r_i) = \left\langle \sum_j V(r_{ij}) \right\rangle, \tag{1.19}$$

where V is the potential of the interaction between nucleons of a distance r_{ij} apart. The Hamiltonian therefore is of the form

$$H = \sum_i T_i + \sum_{ij} V(r_{ij}), \tag{1.20}$$

where T_i is the associated kinetic energy of the interacting nucleons. The form of the central potential in Equation 1.19 is of utmost importance to the shell model. Several potentials have been used in an attempt to recreate the magic numbers with varying success. Figure 1.4 shows the form of some of the potentials used. The square well potential and the harmonic oscillator potential are both successful in reproducing the first three magic numbers, 2, 8 and 20, though the form of these potentials are both physically unreasonable for the description of the nuclear potential. The square well potential has well understood solutions but the potential has a much sharper edge than the actual nuclear potential. The nuclear potential approximates the charge and matter distribution, falling to zero beyond the mean radius. The harmonic oscillator potential on the other

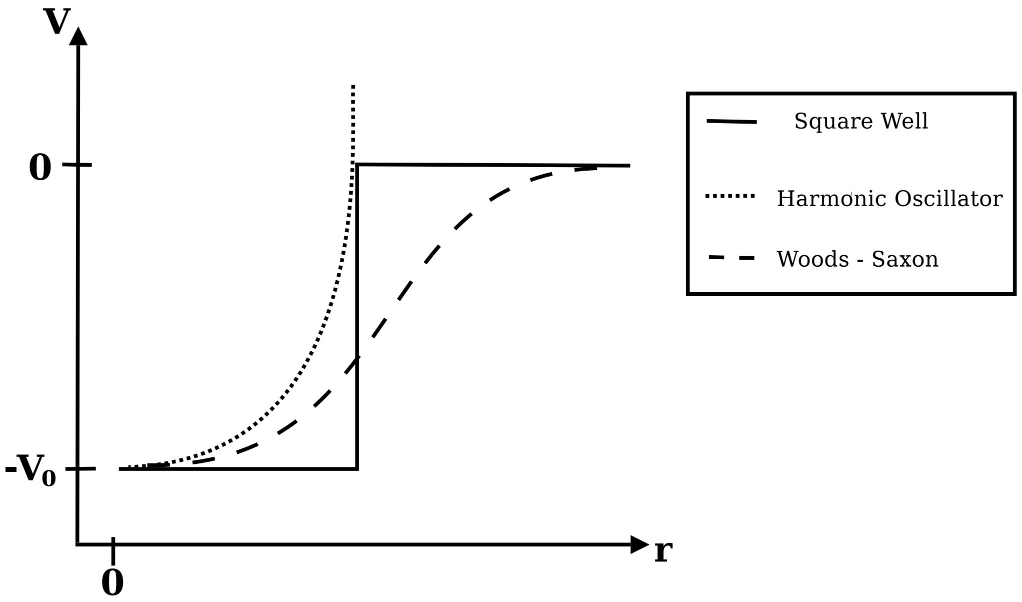

Figure 1.4: Forms of the potential used in the shell model. The square well, harmonic oscillator and Woods-Saxon potentials are illustrated for the purpose of comparison.

hand is not sharp enough. A successful potential will be an intermediate between the square well potential and the harmonic oscillator potential. An often used potential is the Woods-Saxon potential which takes the form

$$V(r) = \frac{-V_0}{1 + exp[(r - R_0)/a]}, \tag{1.21}$$

where R_0 is the average nuclear radius and a the thickness of the diffuse nuclear surface. The solutions from the Woods-Saxon potential closely approximate those found with the harmonic oscillator potential, though the ordering of some levels has changed giving a more realistic account of the experimentally observed order. Figure 1.5 shows a comparison of levels obtained with each potential and the magic numbers obtained. It can be seen that the Woods-Saxon potential alone cannot reproduce the higher magic numbers. To fully reproduce the experimentally observed magic numbers the form of the potential must be modified. A spin-orbit effect much similar to the interaction in atomic physics that lifts the degeneracy of electron levels is used, though in the case of the nucleus an electromagnetic interaction does not cause this effect.

Levels in Figure 1.5 are labelled with $\boldsymbol{j}$, the total angular momentum and $\boldsymbol{l}$ the

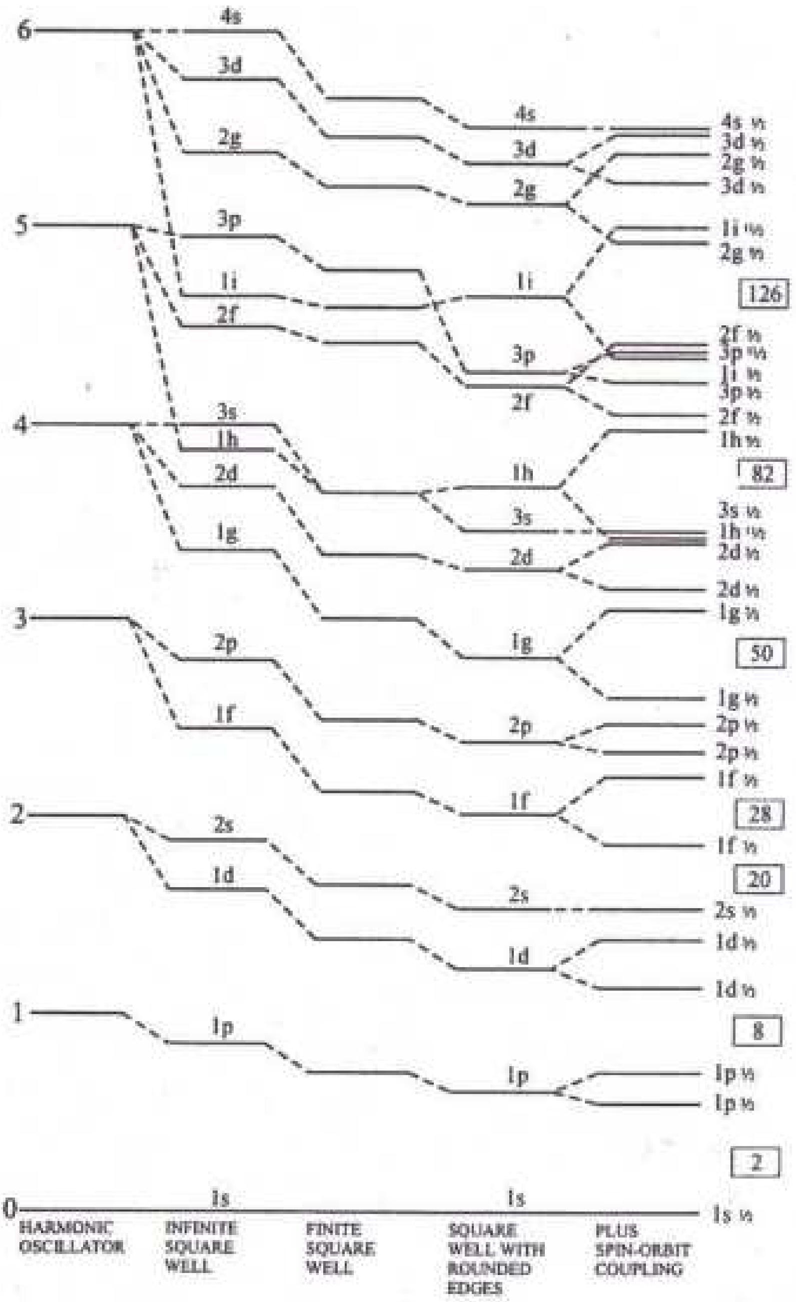

Figure 1.5: Derived states using various shell model potentials [Fel53]. The evolution to a more realistic result can be observed when the Wood-Saxon potential is used and the spin-orbit interaction incorporated.

orbital angular momentum. ***l*** takes its spectroscopic form and where the numbers 0,1,2,3,4,5 are represented by the letters s, p ,d ,f, g and h. The total angular momentum, ***j*** is the sum of the coupling of the orbital angular momentum, ***l*** and the intrinsic angular momentum of a nucleon, ***s***. The Woods-Saxon potential is modified to incorporate the spin-orbit interaction [May49, HJS49] that is a consequence of this coupling and becomes

$$V(r) = \frac{-V_0}{1 + exp[(r - R_0)/a]} + W(r)\mathbf{l} \cdot \mathbf{s}, \tag{1.22}$$

where *W(r)* is a function of the radial position. With the spin-orbit interaction degeneracy of levels is lifted as the total angular momentum of a level, j can be l $\pm\frac{1}{2}$. The position of levels is also modified. The energy separation of these levels is directly proportional to ***l*** and j + $\frac{1}{2}$ states will lie lower in energy than j - $\frac{1}{2}$ states. As can be seen in Figure 1.5 this gives rise to states with a higher value of ***l*** at a lower energy than a state with a lower ***l*** value. These states are known as *intruder states*. With the modification of level positions that the spin-orbit interaction produces the experimental magic numbers can now be reproduced using the modified Woods-Saxon potential. This model predicts the levels of light nuclei close to these magic nuclei well. As one heads towards mid-shell nuclei the model starts to falter. A modification of the shell model is then required.

1.1.5 The Nilsson Model

Since the shell model is unable to describe deformed nuclei far from closed shells, a new model is required that incorporates a deformed nuclear potential. One such model that incorporates such a potential is the Nilsson Model [Nil55] which uses as its base a deformed harmonic oscillator potential. With z axial symmetry the Nilsson Hamiltonian can be written as

$$H = \frac{-\hbar^2}{2m} \bigtriangledown^2 + \frac{m}{2}\left(\omega_x^2 x^2 + \omega_y^2 y^2 + \omega_z^2 z^2\right) - C \cdot l \cdot s - D \cdot (l^2 - \langle l^2 \rangle_N). \tag{1.23}$$

The $l^2 - \langle l^2 \rangle_N$ reflects the flattening of the nuclear potential at the centre of the nucleus. The coefficients C and D account for the strength of the $l{\cdot}s$ spin-orbit interaction and the $l^2 - \langle l^2 \rangle_N$ term respectively and therefore control the shape of the potential enabling the reproduction of the observed sequence of energy levels. It is useful to express the one-dimensional oscillator frequencies, $\omega_{x,y,z}$ in terms of the deformation parameter ε so as

$$\begin{aligned} \omega_x^2 &= \omega_0^2 \left(1 + \frac{2}{3}\varepsilon\right), \\ \omega_y^2 &= \omega_0^2 \left(1 + \frac{2}{3}\varepsilon\right), \\ \omega_z^2 &= \omega_0^2 \left(1 - \frac{4}{3}\varepsilon\right), \end{aligned} \tag{1.24}$$

where ω_0 is the oscillator frequency in a spherical potential.

The asymptotic quantum numbers are often used to describe the Nilsson orbitals. The description of the Nilsson orbitals take the form

$$\Omega^\pi \left[N n_z \Lambda\right] \tag{1.25}$$

where Ω is the projection of the single particle total angular momentum along the axis of symmetry, N the principle quantum number, n$_z$ the oscillator quanta projected along the z-axis, π the parity of the state and Λ the projection of the orbital angular momentum along the z-axis. With Ω being the sum of Λ and Σ, where Σ is the intrinsic single particle spin along the z-axis we can define Ω as

$$\Omega = \Lambda \pm \frac{1}{2}, \tag{1.26}$$

as Σ can only take values $\pm\frac{1}{2}$. We can determine the parity of a state, π from the principle quantum number N using the relation

$$\pi = (-1)^N. \tag{1.27}$$

The principle quantum number N also allows the constraint of Λ to discrete values. If N is odd then $(n_z + \Lambda)$ must also be odd. If N is even then $(n_z + \Lambda)$ must also be even. A plot of the Nilsson orbits is shown in Figure 1.6, taken from [SZF02]. It can be seen at $\varepsilon = 0$ the orbitals are *2j+1* degenerate. This degeneracy is lifted with the onset of deformation. It is observed from this plot that for a

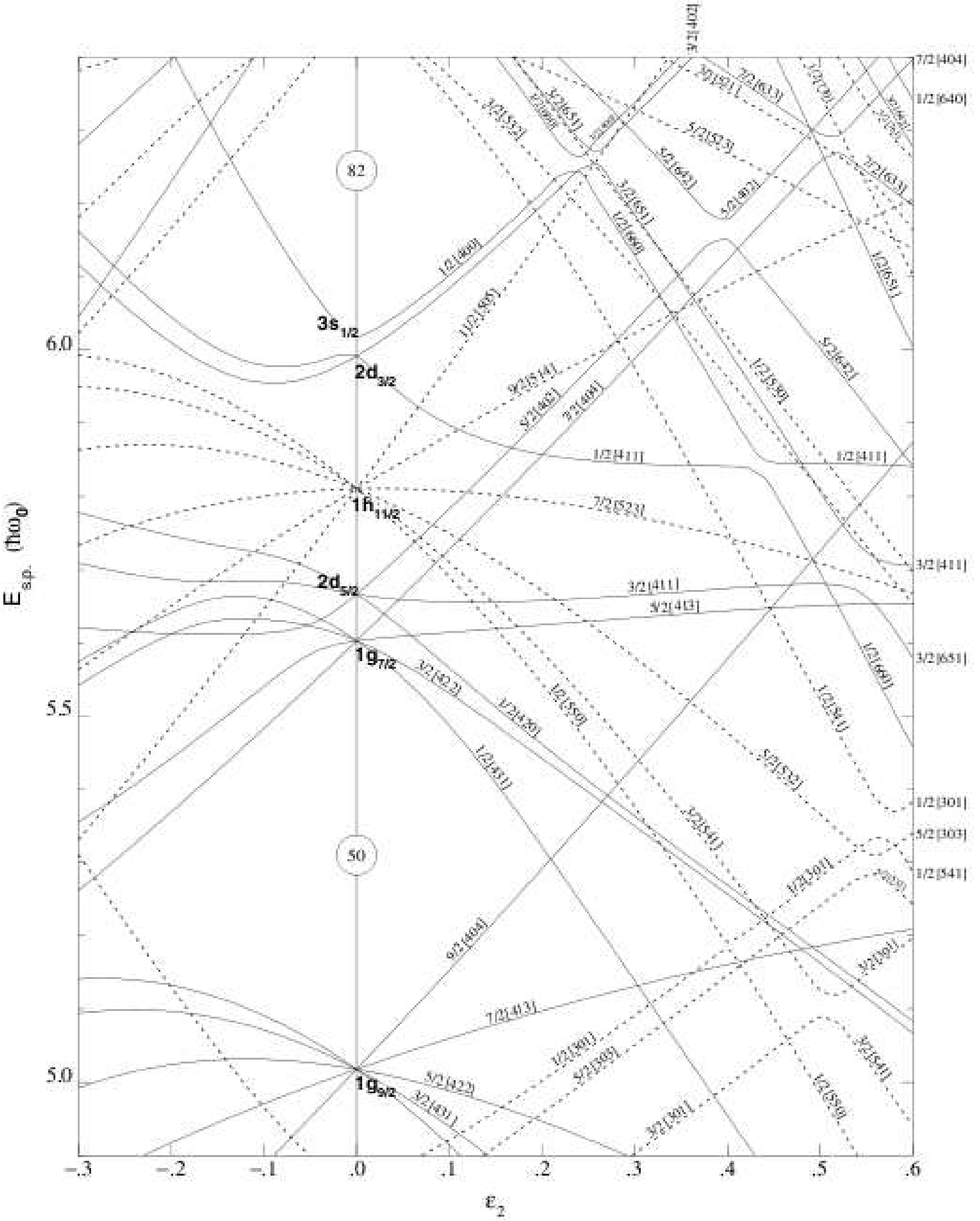

Figure 1.6: Nilsson diagram for $50 \leq Z \leq 82$ showing single particle energy versus deformation.[Sch02]

nucleus with prolate deformation low Ω orbits will have lower energies and high Ω orbits will have higher energies. The converse being true for oblate nuclei. With the projection of the total nuclear angular momentum along the axis of symmetry being K, which is equal to Ω for a nucleus with a single valence nucleon, we can denote the angle between the orbital plane and the axis of symmetry to be

$$\theta = \sin^{-1}\left(\frac{K}{j}\right). \tag{1.28}$$

For high K values, θ changes greatly leading to rapid changes in energy as deformation increases. This can lead to two orbits with the same quantum numbers approaching each other. The Pauli exclusion principle ensures that no two Nilsson levels with the same value of Ω and π can cross. As orbits with the same values of Ω and π are driven closer together, due to the onset of deformation, the Pauli exclusion principle cause the orbits to repel. At the inflection point wave functions interact and strong multi-state mixing occurs.

1.2 Shape Coexistence and Collectivity in the Hg Region

In certain regions of the nuclear chart a subtle re-arrangement of a few nucleons close to the Fermi surface can have dramatic effects on the shape of the nucleus. When nucleons close to the Fermi surface are promoted across a shell gap for instance the nucleus will re-arrange itself and find a new minimum in the nuclear potential that often corresponds to a different shape or a drastic change in deformation. An often quoted experimental signature for such a phenomenom is the appearance of low-lying 0^+ states [WHN$^+$92] on which the rotational bands of the differing shapes are built. A recent example that typifies shape coexistence in the Hg region of the nuclear chart is the case of ^{186}Pb [AHD$^+$00]. In this nucleus the first two excited states have been assigned 0^+ states. They are assumed to be the band heads of oblate and prolate rotational configurations competing with the spherical ground state of the nucleus. In the case of light Hg isotopes shape

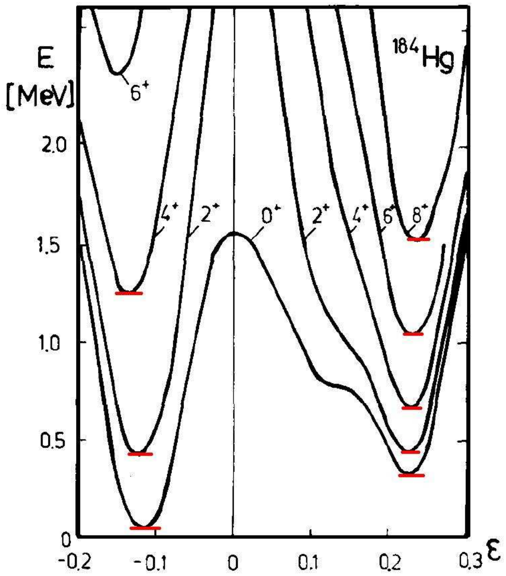

Figure 1.7: Plot of level energy vs deformation for ^{184}Hg. Two distinct minima can be seen at approximately -0.15 and 0.25, associated with the oblate and prolate configurations. [Naz93]

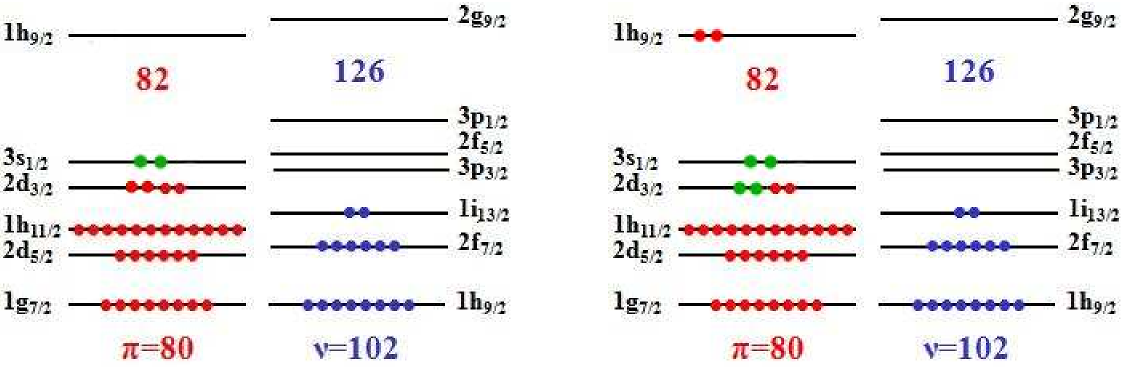

Figure 1.8: Particle configuration for ^{182}Hg. The left panel shows the microscopic *0p-2h* configuration of the *oblate* structure of the ground state band. The right panel shows the excitation of two protons across the *Z=82* shell gap, leading to the *2p-4h* configuration of the *prolate* structure. Holes are represented in green, neutrons in blue and protons in red.

coexistence was first observed when isotope shift measurements revealed a sharp change in energy between ^{187}Hg and ^{185}Hg [BHK^{+}72]. Consequently this was interpreted as being due to a change in nuclear shape from a weakly deformed oblate band to a more deformed prolate band [FP75]. To further support this case, charge radii measurements have revealed a weak oblate character for the ground states of even mass Hg isotopes down to A=182 [UBD^{+}86]. As one heads towards the N=104 mid-shell Hg isotopes further evidence of a change in nuclear shape is given in the form of the level energy sequences. Level energies built on the weakly deformed oblate band remain roughly constant until in ^{188}Hg when intruder states from the prolate band cross the yrast line [JHM01]. α-decay studies of the light Hg isotopes have revealed 0_2^+ intruder states for nuclei as neutron deficient as ^{182}Hg. These states have been interpreted as being of the same nature as the mother Pb nuclei due to the α-decay hindrance factors. This has caused the mid-shell Hg intruder structures to be interpreted as being due to the excitation of protons across the Z=82 shell gap [WBD^{+}94] and to the potential energy surface associated with prolate structure [Naz93]. Figure 1.8 shows schematically the oblate and prolate particle configurations predicted for the light Hg isotopes.

Lifetime measurements in the region lend support to the coexistence of nuclear shapes in the isotope chain. Lifetime measurements of yrast states in ^{186}Hg reveal that the 2^+ and 6^+ yrast states have considerably different deformations. The low-lying 2^+ yrast state has a measured deformation of $|\beta| \approx 0.13$ whilst the 6^+ yrast state a value of $|\beta| \approx 0.27$ [PDS73]. The isotope ^{184}Hg shows similar behaviour. Lifetime measurements of this nucleus [MRH^{+}86] show that the yrast 2^+ state has a deformation of $|\beta| \approx 0.15$ and the subsequent 4^+ and 6^+ yrast states a deformation of $|\beta| \approx 0.22$ and $|\beta| \approx 0.28$ respectively. If the potential energy as a function of deformation has two minima, this transformation can be simply explained. Lower yrast states would be confined to a potential well located at a small deformation. Higher yrast states would be located at the second minima where the deformation is greater. Figure 1.7 shows the case for ^{184}Hg, but can be seen as representative of the neutron deficient Hg isotopes. The 2^+

yrast state is located in the minima associated with a weak, oblate deformation whereas the higher yrast states are located in the more deformed prolate minima. As one descends the isotopic chain to the neutron midshell, it becomes unclear as to whether the prolate or oblate 2^+ state is yrast as the prolate intruder states become lower in energy. It is an aim of this work to answer this. With evidence to suggest shape coexistence in the light Hg region in abundance, it is of great interest to obtain direct measurements of the nuclear shapes in the region. This thesis reports the results of a method that allows direct, model-independent measurements of nuclear shapes. This is the reorientation effect in Coulomb excitation measurements, which has been used for over 50 years to obtain direct measurements of nuclear shapes. With the advancement of facilities such as REX-ISOLDE it is now possible to re-employ this powerful technique to heavier radioactive nuclei. The Coulomb excitation of ^{182,184,186,188}Hg will for the first time give direct measurements of the electric quadrupole matrix elements in the low-lying states of these nuclei. This will allow for the unambiguous assignment of nuclear shape to the observed states in these nuclei.

1.3 Coulomb Excitation and Lifetime Measurements

Two complementary techniques have been employed to obtain direct measurements of the transition and quadrupole matrix elements in low-lying states of light Hg isotopes. Lifetime measurements allow for the the transition matrix elements of excited states to be obtained. This allows the magnitude of the deformation to be inferred, though no sign to the deformation can be assigned. Coulomb excitation allows one to study a nucleus outside of the influence of the strong nuclear force. The level excitation can be solely attributed to the influence of the electromagnetic force, which is well understood [Ald75]. The bombarding energy is set low enough so the colliding nuclei are far enough apart that there is no influence from the strong nuclear force. This allows for model-independent analysis of the excited states, as the only nuclear properties entering into the analysis are the static and dynamic electric multipole moments of the nuclei. This enables the extraction of the sign of the quadrupole moment and allows for the assignment of a shape to the excited nuclear state. One measures both the static and dynamic multipole moments with Coulomb excitation. Lifetime measurements provide a measurement of the dynamic multipole moment and a value for the magnitude of the deformation. The two methods are complementary in that they provide a check for each analysis.

1.4 Organisation of Thesis

Chapter 1 discusses basic concepts and models in nuclear physics and outlines shape coexistence in the Hg region. Chapter 2 details the theory of Coulomb excitation and the the methods used for lifetime measurements, namely the Recoil Distance Doppler Shift (RDDS) method and the Differential Decay Curve Method (DDCM). Chapter 3, experimental techniques and facilities describes the theory behind γ-ray spectroscopy and details the important aspects of the REX-ISOLDE facility and Jyväskylä Accelerator laboratory. Chapters 4 and 5 detail the analysis techniques and results obtained for lifetime measurements performed at Jyväskylä, and the Coulomb excitation experiment performed at REX-ISOLDE, respectively. A discussion of the two sets of results and conclusions are presented in Chapter 6.

Chapter 2

Coulomb Excitation and Lifetime Measurements

To fully understand and interpret the results presented in Chapter 4 and Chapter 5 the relevant theory and techniques used to obtain the results are discussed in this chapter. The first half of the chapter deals with the extensive theory of Coulomb excitation and the experimental method itself. The second half of this chapter discusses the experimental techniques, and the associated theory, employed in lifetime measurements of excited nuclear states. Let us begin with Coulomb excitation.

2.1 Coulomb Excitation

In this section the theoretical aspects of Coulomb excitation will be outlined along with an overview of the experimental technique itself. A brief overview of the classical theory of elastic scattering along with collision parameters involved in inelastic scattering will be presented. As the experiment discussed in Chapter 5 was performed at low, sub Coulomb barrier energies, a description of *safe* Coulomb excitation will be given. Matrix elements and the importance of the electric quadrupole moment are discussed in regards to determining nuclear shape. A much more detailed description of the theories presented this section

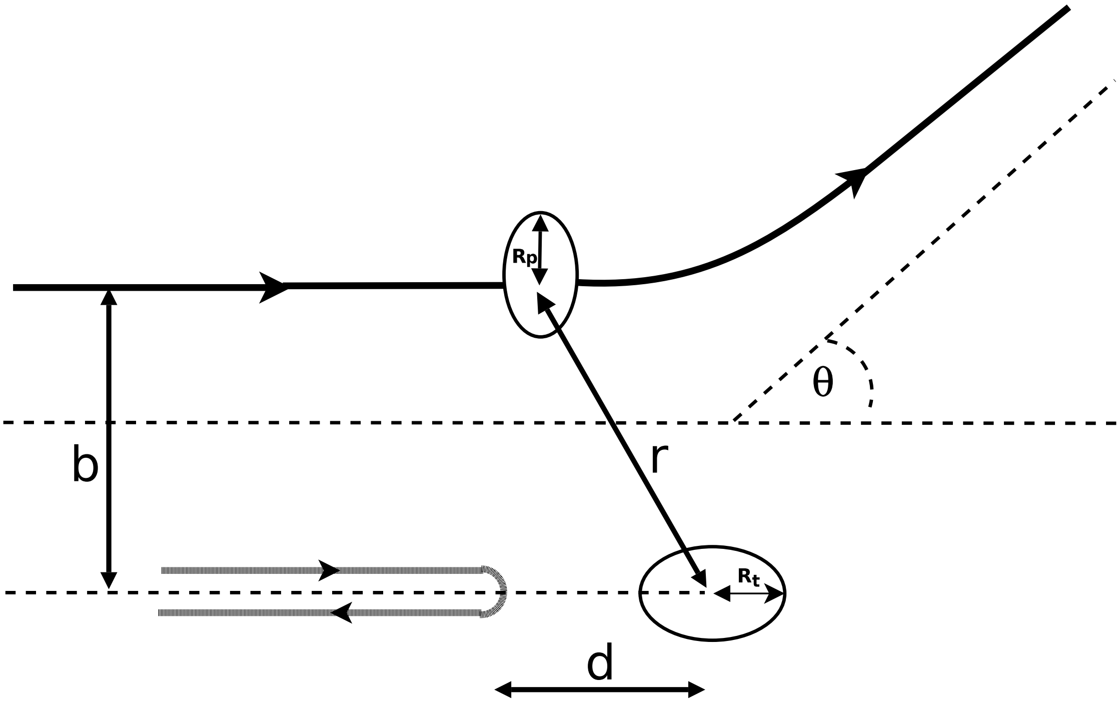

Figure 2.1: Trajectory of a particle undergoing Rutherford scattering. The impact parameter, b, the centre of mass scattering angle, θ, and the distance between the nuclear centre of masses, r, are indicated on the diagram. The distance of closest approach, d, is also indicated along with the projectile and target radii, R_p and R_t, respectively.

can be found in references such as [ABH$^+$56, AS64, Ald75].

2.1.1 Rutherford Scattering

The nucleus consists of both neutral and charged particles. Because of this the nucleus has a distribution of electric charge that means it can be studied by the Coulomb scattering of charged particles. This may be via collisions of an elastic or inelastic nature. An elastic scattering process conserves kinetic energy and is known as *Rutherford* scattering. An inelastic scattering process does not conserve kinetic energy as part of this energy is transferred to excite the nucleus into an higher energy level. The scattering process, which is common to both elastic and inelastic scattering, is shown schematically in Figure 2.1.

The interaction of the two particles will obey Coulomb's Law, which is expressed in terms of the charge of the projectile, Z_pe, the charge of the target,Z_te, and the distance between the two interacting particles, r. The force experienced, F, is therefore

$$F = \frac{1}{4\pi\varepsilon_0}\frac{Z_p Z_t e^2}{r^2}. \tag{2.1}$$

The hyperbolic trajectory of the scattered particle shown in Figure 2.1 is a direct result of the inverse square law that is embedded in Equation 2.1. If the projectile nucleus approaches the target nucleus along a straight line in the absence of the Coulomb force, the distance between the target and projectile nuclei would be b, the *impact parameter*. With the Coulomb force diminishing as $1/r^2$, at large distances the projectile particle has negligible Coulomb potential energy. The incident particle's total energy, E_p, can therefore be attributed to its kinetic energy

$$E_p = \frac{1}{2}mv^2, \tag{2.2}$$

where m is the mass of the incident particle and v is its velocity. This equation holds in non-relativistic circumstances when $v \ll c$. The corresponding angular momentum relative to the target nucleus is

$$\mid \mathbf{r} \times m\mathbf{v} \mid = mvb. \tag{2.3}$$

When passing close to the target nucleus the projectile reaches a minimum distance which depends upon the impact parameter b. The absolute minimum this distance may be is shown in Figure 2.1 to be d and occurs in a head on collision when $b=0$. In this case the projectile comes to rest before reversing its motion. At this point all kinetic energy is exchanged for Coulomb energy

$$\frac{1}{2}mv^2 = \frac{1}{4\pi\varepsilon_0}\frac{Z_p Z_t e^2}{d^2}, \tag{2.4}$$

where d is defined as the *distance of closest approach*. At intermediate points along the trajectory the energy of the projectile is part kinetic, part Coulomb potential energy.

As the Coulomb potential is symmetric, so to is the scattering process about the beam axis. The scattering process is therefore independent of azimuthal angle ϕ. This process does have a large dependence on the polar scattering angle θ.

Using a classical treatment it can be shown that the differential scattering cross section can be expressed in terms of the polar angle

$$\frac{d\sigma_R}{d\Omega} = \left(\frac{Z_p Z_t e^2}{4\pi\varepsilon_0}\right)^2 \left(\frac{1}{4E_p}\right)^2 \frac{1}{sin^4(\frac{\theta}{2})} \tag{2.5}$$

Equation 2.5 is known as the *Rutherford cross section.* It can be seen that the scattering cross section decreases with increasing scattering angle and projectile energy whilst the nuclear charge increases the cross section. These relations play an important part in target selection and the analysis discussed in Chapter 5.

2.1.2 Collision Parameters

The semi-classical approximation describes the motion of the colliding nuclei in terms of classical hyperbolic orbits. The excitation process is dealt with in a quantum mechanical framework. To justify the use of a semi-classical approximation three collision parameters are considered and discussed below: the *Sommerfeld parameter,* η, the *adiabaticity parameter,* ξ and the *excitation strength parameter,* χ.

The Sommerfield Parameter

In Coulomb excitation the monopole-monopole interaction, $Z_p Z_t e^2/r$ has a dominant influence on the trajectory of the colliding particles. The strength of the modification to the trajectory of charged particles caused by the Coulomb interaction is measured by the dimensionless Sommerfeld parameter, defined as the ratio of half the distance of closest approach, $d = Z_p Z_t e^2/\hbar v$, to the de Broglie wavelength of the projectile at infinity, $\lambda = \hbar/m_0 v$

$$\eta = \frac{d}{2\lambda} = \frac{Z_p Z_t e^2}{\hbar v} \tag{2.6}$$

where $Z_p e$ and $Z_t e$ are the projectile and target charge respectively, and v is the relative velocity of target and projectile. If the Sommerfeld parameter is small ($\eta \ll 1$) the Coulomb field will not modify the wavefunction of the projectile significantly and a plane wave approximation may be used. For energies below the Coulomb barrier the Coulomb force is sufficiently strong to keep the projectile from the range of the strong nuclear force. Under this condition $\eta \gg 1$ and the projectile can be considered to follow a classical trajectory. A semi-classical approximation is therefore valid if $\eta \gg 1$. In the case of the light Hg isotopes scattering on Cd discussed in Chapter 5 a typical value for η, assuming a value of $\beta \approx 0.04c$ would be $\eta \approx 686$.

The Adiabaticity Parameter

The semi-classical approximation neglects the fact that the projectile nucleus loses energy to the target nucleus during the collision process. The excitation energy is defined as $\Delta E_{if} = E_i - E_f$ and cannot be included in an accurate manner due to the exact point of transfer being unknown. For the classical trajectory to be valid it is important that this energy loss does not alter the hyperbolic orbit significantly. It is therefore a condition of the semi-classical approximation that

$$\frac{\Delta E_{if}}{E_{cm}} \ll 1, \tag{2.7}$$

where E_{cm} is the centre of mass energy $\frac{1}{2}m_0 v^2$.

The excitation of an initial state $|i\rangle$ to a final state $|f\rangle$ though the influence of a time dependent electromagnetic potential, $V(\boldsymbol{r}(\boldsymbol{t}))$ may only occur if the collision time, τ, is shorter than, or of the same order of magnitude as the nuclear period, Δt, characteristic of the transition. Δt being defined as $\hbar/\Delta E_{if}$. The product of the nuclear frequency, $\Delta E_{if}/\hbar$ and the collision time, τ, define the adiabaticity parameter

$$\xi = \frac{\tau \Delta E_{if}}{\hbar} = \frac{\tau}{\Delta t}. \tag{2.8}$$

For a state $|i\rangle$ to be excited to state $|f\rangle$, the value of ξ must be of the order or smaller than unity. We therefore have a condition for the validity of the semi-classical approximation to hold of

$$\xi \leq 1. \tag{2.9}$$

As the collision time can be estimated to be the time it takes for the projectile to travel a distance of the order

$$d(\theta) = a\left(1 + \frac{1}{\sin\left(\frac{1}{2}\theta\right)}\right), \tag{2.10}$$

where *d(θ)* is the distance of closest approach for a centre of mass scattering angle, θ. a is half the distance of closest approach in a head on collision and thus defined as

$$a = \frac{1}{2}d = \frac{1}{2}\frac{Z_pZ_te^2}{m_0\nu^2}. \tag{2.11}$$

It can then be shown [Ald75] that the ratio of $\Delta E_{if}/E_{cm}$ can be written in terms of the adiabaticity parameter, ξ and the Sommerfeld parameter, η giving

$$\frac{\Delta E_{if}}{E_{cm}} = \frac{2\xi}{\eta}. \tag{2.12}$$

If the conditions $n \gg 1$ and $\xi \ll 1$ are met then the condition described in Equation 2.7 must also be fulfilled. It can be seen in Equation 2.12 that a large value of η could allow for a value of $\xi \gg 1$ and still have the condition described in Equation 2.7 fulfilled. However with large values of ξ the excitation probability falls exponentially.

From Equation 2.12, a limit to the achievable excitation energy through Coulomb excitation can be obtained. Assuming the condition that $\xi \ll 1$, it can be seen that the excitation energy limit is of the order of ∼1 MeV for low-energy Coulomb excitation experiments. In considering the work presented in Chapter 5, a typical value for the adiabaticity parameter would be $\xi \approx 0.81$ and is therefore fully compliant with conditions described in Equation 2.9 and Equation 2.12.

The Excitation Strength Parameter

The magnitude of the excitation probability has a dependence on the strength of the interaction. A measure of the multipole interaction strength is given by the dimensionless quantity, the excitation strength parameter. This parameter, dependent on the multipole order L, is defined in terms of the reduced matrix element,$\langle I_i||\mathcal{M}(E2)||I_f\rangle$ coupling the initial state $|i\rangle$ to the final state $|f\rangle$

$$\chi(\mathcal{M}\lambda) = \frac{\sqrt{16\pi}(L-1)!}{(2L+1)!!} \cdot \frac{Z_p e}{a^L \hbar v} \cdot \frac{\langle I_f||\mathcal{M}(E2)||I_i\rangle}{\sqrt{2I_i+1}} \tag{2.13}$$

$\chi(\mathcal{M}L)$ is a measure of the number of quanta exchanged during the collision to the excited state. For lesser values of $\chi(\mathcal{M}L)$ the probability that quanta are exchanged remains small. For larger values of $\chi(\mathcal{M}L)$ the state will be strongly excited, provided $\xi \leq$1.

For certain multipole orders $\chi(\mathcal{M}L)$ can be estimated using the approximation

$$\chi(\mathcal{M}L) \approx \frac{V(\mathbf{r}(\mathbf{t}))\tau}{2\hbar} \tag{2.14}$$

where τ is the collision time and *V(**r**(**t**))* is the time-dependent potential. Upper limits for values of $\chi(\mathcal{M}L)$ are listed below [Ald75]

$$\begin{aligned} \chi(E1) &\approx 10 \\ \chi(E2) &\approx 10 \\ \chi(E3) &\approx 0.5 \\ \chi(M1) &\approx 0.1 \end{aligned} \tag{2.15}$$

It can be seen that the values of $\chi(\mathcal{M}L)$ for higher multipole orders are two orders of magnitude smaller, indicating that these higher multipoles result in little excitation of the final state. As they are much less important than L = 1,2 multipoles they can, to a very good approximation be neglected in Coulomb excitation calculations.

As $\chi(\mathcal{M}L)$ measures the number of quanta of angular momentum transferred during the collision process, another condition for the validity of the semi-classical approximation can be gained. In order to continue to describe the trajectory of the colliding nuclei in a classical manner the angular momentum transferred to the target nucleus from the projectile, Δl must be significantly lower than the orbital angular momentum, l i.e $\Delta l \ll l$. This leads to the restriction

$$\frac{\chi(L)}{\eta\tau} \ll 1. \tag{2.16}$$

If this is not fulfilled the transferred angular momentum will have a significant effect on the trajectory of the nuclei and the semi-classical approach will no longer be valid.

2.1.3 Safe Coulomb Excitation

With increasing energy comes increasing probability for Coulomb excitation. It is therefore desirable to have the highest beam energy possible to increase the chances of successful Coulomb excitation. To be confident that the process remains purely electromagnetic, it must be ensured that the colliding particles remain outside the range of the strong nuclear force. To ensure this condition the *distance of closest approach*, *2a*, defined in Equation 2.11, must exceed the sum of the radii of the nuclei plus an addition safety distance Δ_s.

$$2a > R_p + R_t + \Delta_s \tag{2.17}$$

Δ_s accounts for the range of the nuclear force and the surface diffuseness of the nuclear distribution. A review of experimental data on Coulomb-nuclear interference effects [Cli86] found that the nuclear contribution occured at a level of less than 0.1% when using a value of $\Delta_s = 5\,\text{fm}$, when assuming a nuclear radius given by $R = 1.2A_i^{1/3}$. Using this value of Δ_s a "safe" Coulomb excitation criteria can be obtained with regards to the distance of closest approach.

$$2a > \left[R_0\left(A_p^{1/3} + A_t^{1/3}\right) + 5\right] \tag{2.18}$$

with a value of $R_0 = 1.2\,\text{fm}$ used in this work. The value of Δ_s can now be used to obtain a limit on the beam energy to ensure "safe" Coulomb excitation. The Coulomb barrier can be defined by the following equation

$$E_{cb} = \frac{1}{4\pi\varepsilon_0}\frac{Z_pZ_t}{R_{int}}\left(1 + \frac{A_p}{A_t}\right) \tag{2.19}$$

R_{int} being the interaction radius. The interaction radius for safe Coulomb excitation must be defined using the values of Δ_s and r_0 given above

$$R_{int} = R_0\left(A_p^{1/3} + A_t^{1/3}\right) + \Delta_s = 1.2\left(A_p^{1/3} + A_t^{1/3}\right) + 5 \tag{2.20}$$

taking $1/4\pi\varepsilon_0 = 1.44\,\mathrm{MeV{\cdot}fm}$ a limiting beam energy for safe Coulomb excitation can be taken as

$$E_{scb} = 1.44 \cdot \frac{Z_p Z_t}{1.2\left(A_p^{(1/3)} + A_t^{1/3}\right) + 5}\left(1 + \frac{A_p}{A_t}\right) MeV. \tag{2.21}$$

For "safe" Coulomb excitation the main criteria is therefore that the lab energy of the impinging beam is less than the energy defined by Equation 2.21. In the case of the experiments discussed in Chapter 5, a beam energy of $\sim$ 515 MeV can be clearly seen to be "safe", as the limiting energy was in the region of $\sim$ 825 MeV.

2.1.4 First Order Perturbation Theory

First order perturbation theory allows a simple, yet comprehensive picture to be obtained describing excitation amplitudes and probabilities for projectile Coulomb excitation. In this description the differential Coulomb excitation cross section, $\left(\frac{d\sigma}{d\Omega}\right)_n$, can be written in terms of the Rutherford cross section,$\left(\frac{d\sigma}{d\Omega}\right)_R$, defined in Equation 2.5, and the parameter P_n

$$\left(\frac{d\sigma}{d\Omega}\right)_n = P_n \left(\frac{d\sigma}{d\Omega}\right)_R, \tag{2.22}$$

where P_n is the probability of excitation to the state $|n\rangle$. With the excitation of nuclear levels being described in a classical sense by the time-dependent electromagnetic field induced by the motion of the projectile passing the target nucleus, the excitation amplitude can be found from the solutions of the time-dependent Schrödinger equation

$$i\hbar\frac{\partial}{\partial t}|\psi(t)\rangle = \left(H_0^{(p)} + H_0^{(t)} + W(p,t) - \frac{Z_p Z_t}{r} \cdot \frac{e^2}{4\pi\epsilon_0}\right)|\psi(t)\rangle, \tag{2.23}$$

with $H_0^{(p)}$ being the ground-state projectile Hamiltonian, $H_0^{(t)}$ the ground state target Hamiltonian and *W(p,t)* the electromagnetic interaction between target and projectile. A quantum mechanical expansion of the electromagnetic interaction between target and projectile can be expressed as the sum of three factors;

a monopole-monopole interaction, *W_{EE}(p,t)*, a monopole-multipole interaction, *W_{EM}(p,t)* and a multipole-multipole interaction, *W_{MM}(p,t)* leading to

$$W(p,t) = W_E(p,t) + W_{EM}(p,t) + W_{MM}(p,t). \tag{2.24}$$

The semi-classical approach to Coulomb excitation reduces the monopole-monopole interaction to classical kinematics. This interaction does not contribute to the excitation of the nucleus but rather determines the nuclear orbit. The multipole-multipole interaction is weak with respect to the monopole-multipole interaction and so can be neglected. The monopole-multipole interactions for heavy ion collision can be strong, due to the strength being proportional to the respective electric monopole moment of either target or projectile nuclei allowing for magnetic excitation to occur. It is therefore the solutions to a time-dependent Schödinger equation with a monopole-multipole potential between target and projectile, *V(**r**(t))*, that determine the excitation probabilities, P_n. The solutions of this equation, describing target and projectile excitation therefore take the form

$$i\hbar\frac{\partial}{\partial t}|\psi^{(t)}\rangle = (H_0^{(t)} + V(\mathbf{r}(t))|\psi^{(t)}\rangle, \tag{2.25}$$

and

$$i\hbar\frac{\partial}{\partial t}|\psi^{(p)}\rangle = (H_0^{(p)} + V(\mathbf{r}(t))|\psi^{(p)}\rangle. \tag{2.26}$$

The potential *V(**r**(t))* can be expanded as a multipole series of electric and magnetic matrix elements [Ald75]

$$V(\mathbf{r}(t)) = \sum_{L=1,\mu}^{\infty} \frac{4\pi Z_{p(t)}e}{2L+1}(-1)^L \overline{S_{\sigma L}}(t)\mathcal{M}(\sigma,-L), \tag{2.27}$$

where $\overline{S_{\sigma L}}(t)$ is the time-dependent collision function and $\mathcal{M}(\sigma,-L)$ is the multipole transition operator for electric or magnetic transitions. This allows for the excitation probabilities to be directly linked to the transition matrix elements of the studied nucleus. To aid in the solution of Equations 2.25 and 2.26 it is assumed that collision and excitation occur much more rapidly than the decay of the excited state. With collision times in the order of $\sim 10^{-20}$ - 10^{-19} seconds [Cli86], the *sudden approximation* is valid as lifetimes of excited states in the nuclei studied in this thesis are of the order of picoseconds. Using this approximation and solving Equations 2.25 and 2.26 at time $t = +\infty$, the time at which collisions have ended, a solution can be obtained containing a sum of excitation amplitudes, $a_n = \langle n|\psi(+\infty)\rangle$ when assuming nuclear eigenstates $|n\rangle$ for n excited states. The eigenvalues of these states are then defined by

$$\begin{aligned} H_0^{(p)}|n\rangle &= E_n^{(p)}|n\rangle, \\ H_0^{(t)}|n\rangle &= E_n^{(t)}|n\rangle. \end{aligned} \tag{2.28}$$

By summing and averaging over initial and final magnetic substates the probability of excitation to the energy state $|n\rangle$ is then $P_n = |a_n|^2$ which has the solution

$$P_n = \left| \frac{1}{i\hbar} \int_{-\infty}^{+\infty} \langle n|V(\mathbf{r}(t))|0\rangle e^{i\Delta Et/\hbar} dt \right|^2 \tag{2.29}$$

with ΔE being the change in energy from initial to final state. By taking into consideration the fact that ΔE is small in relation to the total energy and the fact that the collision time is much shorter than the lifetimes of the excited states then a simplification to Equation 2.29 can be performed giving

$$P_n = \left| \langle n| e^{\frac{1}{i\hbar}\{\int_{-\infty}^{+\infty} V(\mathbf{r}(t))dt\}} |0\rangle \right|^2 . \tag{2.30}$$

2.1.5 Coulomb Excitation Cross Section

So as one can evaluate the matrix element in Equation 2.29, and therefore determine the differential and absolute cross sections, a multipole expansion of $V(\boldsymbol{r}(t))$ must be performed. Using the expansion of $V(\boldsymbol{r}(t))$ shown in Equation 2.27 it can be seen that $V(\boldsymbol{r}(t))$ contains both electrostatic and magnetic components. The Coulomb excitation cross sections arising from the electic and magnetic components must be considered separately and are given for each order EL by

$$\sigma_{EL} = \left(\frac{Z_p}{\hbar v} \cdot \frac{e^2}{4\pi\epsilon_0} \right)^2 a_0^{-2L+2} B(EL; I_i \rightarrow I_f) f_{EL}(\xi) \tag{2.31}$$

with

$$f_{EL}(\xi) = \int_{\theta_1}^{\theta_2} \frac{df_{EL}(\theta,\xi)}{d\Omega} \cdot d\Omega. \tag{2.32}$$

$f_{EL}(\xi)$ is the Coulomb excitation function for electric excitations and is integrated over the solid angle covered by the particle detector, with θ_1 and θ_2 being the minimum and maximum angles respectively.

Similarly, the excitation due to the magnetic interaction is determined by

$$\sigma_{ML} = \left(\frac{Z_p}{\hbar c} \cdot \frac{e^2}{4\pi\epsilon_0} \right)^2 a_0^{-2L+2} B(ML; I_i \rightarrow I_f) f_{ML}(\xi) \tag{2.33}$$

with

$$f_{ML}(\xi) = \int_{\theta_1}^{\theta_2} \frac{df_{ML}(\theta, \xi)}{d\Omega} \cdot d\Omega \tag{2.34}$$

and is the analogue of $f_{EL}(\xi)$ for the magnetic interaction. If one compares Equation 2.31 with Equation 2.33 a noticeable difference is the fact that the magnetic interactions are suppressed by a factor of $\left(\frac{v}{c}\right)^2$ compared to the electric excitations. With REX-ISOLDE able to supply beams with a maximum energy of $\sim$3 MeV/u, a maximum value of $\left(\frac{v}{c}\right)$ would be $\approx$0.08, meaning the magnetic interactions would be only 0.6% the strength of the corresponding electric interaction. For this reason the electric excitations are by far the most dominant excitation mechanism in the experiments described in Chapter 5.

From Equation 2.31 and Equation 2.33 it follows that in first order perturbation theory the Coulomb excitation cross section is directly proportional to the reduced transition probability

$$\sigma_{\mathcal{M}L} \propto B(\mathcal{M}L; I_i \rightarrow I_f). \tag{2.35}$$

If one therefore measures the Coulomb excitation cross section a value of $B(\mathcal{M}L)$ can be obtained. In the case of an *E2* transition from a 0^+ ground state to an excited 2_1^+ state the Coulomb excitation cross section would yield the $B(E2; 0_1^+ \rightarrow 2_1^+)$ value for the corresponding transition. From this value the magnitude of the deformation parameter, β_2 can be obtained allowing for a measure of the quadrupole deformation. The lifetime of the excited state can also be deduced from the measured Coulomb excitation cross section through the $B(E2; 0_1^+ \rightarrow 2_1^+)$ value. This will be discussed in § 2.1.6.

2.1.6 Electromagnetic Transitions and the Quadrupole Moment

The electric quadrupole moment of a nucleus quantifies the extent to which the nuclear charge distribution deviates from spherical symmetry. The spectroscopic quadrupole moment Q_s is defined as,

$$Q_s = \langle I, M = I|\widehat{Q}|I, M = I\rangle, \tag{2.36}$$

and the quadrupole operator is given by,

$$e\widehat{Q_s} = \int \rho_e(r) r^2 (3\cos^2\theta - 1) \cdot d\tau, \tag{2.37}$$

in terms of the charge-density distribution $\rho_e(r)$. In the special case of a spherical nucleus, then on average,

$$x^2 = y^2 = z^2 = r^2\cos^2\theta = \frac{r^2}{3},$$

and thus the integrand in Equation 2.37 vanishes, therefore a spherical nucleus has a quadrupole moment of zero.

The quantity Q_s, frequently termed the *spectroscopic* quadrupole moment or the *static* quadrupole moment, represents the diagonal element of the spherical electric quadrupole tensor, given by,

$$eQ_0 = \left(\frac{16\pi}{5}\right)^{1/2} \frac{1}{\sqrt{2I+1}} \langle II20|II\rangle \langle I||\mathcal{M}(E2;\mu = 0)||I\rangle. \tag{2.38}$$

The rotational model allows for the observed excitations of a deformed nucleus to be explained in terms of a collective rotation involving all nucleons. It is assumed that the *transitional* and *static* quadrupole moments are equal. The reduced transitional matrix element is then related to the transitional quadrupole moment, Q_t by the relation

$$\langle I_f||\hat{m}L||I_i\rangle = \sqrt{\frac{5}{16\pi}} \cdot \sqrt{2I_f+1} \cdot \langle I_f K L 0|I_i 0\rangle Q_t \tag{2.39}$$

with $\hat{m}L$ being the electromagnetic multipole operator. Within this model one can relate the static quadrupole moment, Q_s to the reduced diagonal matrix element according to

$$\langle I||\hat{m}L||I\rangle = \sqrt{\frac{5}{16\pi}} \cdot \sqrt{2I+1} \cdot \langle IKL0|I0\rangle Q_s \tag{2.40}$$

The spectroscopic quadupole moment can also be defined in terms of the reduced diagonal matrix element such that

$$Q_s = \sqrt{\frac{16\pi}{5}} \frac{1}{\sqrt{2I+1}} \langle IIL0|II\rangle\langle I||\hat{m}L||I\rangle. \tag{2.41}$$

The spectroscopic quadrupole moment measured in the laboratory frame of the rotating nucleus is related to the intrinsic quadrupole moment Q_0, which would be observed in the frame of reference whereby the nucleus is at rest, according to,

$$Q = \frac{3K^2 - I(I+1)}{(I+1)(2I+3)} \cdot Q_0. \tag{2.42}$$

In even-even nuclei, the ground state band has $K = 0$ and therefore $\pm Q \rightarrow \mp Q_0$; a prolate nucleus has a negative Q and positive Q_0 value, whereas an oblate deformation is characterised by a positive Q and negative Q_0.

When a nucleus has undergone Coulomb excitation it is, by definition, in an excited state. This excited state usually decays by an electromagnetic γ-ray transition. The γ-ray transition probability for a transition from the final, excited state, I_f to the initial state, I_i is given by

$$\lambda(L) = \frac{1}{\tau} = \frac{8\pi(L+1)}{\hbar L[(2L+1)!!]^2} \left(\frac{E_\gamma}{\hbar c}\right)^{2L+1} B\left(\mathcal{M}L; I_i \rightarrow I_f\right) \tag{2.43}$$

with L being the multipole index, τ the lifetime of the excited state, I_f, E_γ the energy of the emitted γ-ray and $B(\mathcal{M}L; I_i \rightarrow I_f)$ the reduced transition probability which is defined as

$$B\left(\mathcal{M}L; I_i \rightarrow I_f\right) = \frac{1}{2I_i+1} \left|\langle I_f||\hat{m}L||I_i\rangle\right|^2 \tag{2.44}$$

with $\hat{m}L$ being the electromagnetic multipole operator. With the electromagnetic multipole matrix elements that characterise the excitation from the initial state, I_i to the final state I_f being the same as those that characterise the decay from the final state to the initial state the cross section for Coulomb excitation to a particular state is the same as the decay constant for a γ-ray transition from the excited state. The reduced transition probability for the downward transition can therefore be written as

$$B(\mathcal{M}L; I_f \rightarrow I_i) = \frac{2I_i + 1}{2I_f + 1} B(\mathcal{M}L; I_i \rightarrow I_f)$$

$$= \frac{1}{2I_f + 1} |\langle I_f || \hat{m}L || I_i \rangle|^2. \tag{2.45}$$

Equation 2.45 indicates that the *B(E2)* values are sensitive to the wavefunctions of the initial and final states. As the electromagnetic operators are well known direct information about the structure of the nuclear states can be obtained from measurements of the absolute transition probabilities.

In the case of an electric quadrupole transition the reduced transition probability can be related to the intrinsic quadrupole moment, Q_0 with the relation

$$B(E2; I_i \rightarrow I_f) = \frac{5}{16\pi} \cdot Q_0^2 \cdot \langle I_i K 20 | I_f K \rangle^2 \tag{2.46}$$

The deformation of a nuclear state can be directly inferred from the size and sign of the quadrupole moment. The Coulomb excitation cross section is influenced by the quadrupole moment through the *reorientation effect*. This second order process describes the effect that the size and sign of the quadrupole moment has on the magnitude of the Coulomb excitation cross section. A quadrupole moment that is positive will result in a positive diagonal matrix element and lead to constructive interference with the first-order transition. This will increase the observed Coulomb excitation cross section. Conversely a negative quadrupole moment, that results in a negative diagonal matrix element will decrease the Coulomb excitation cross section as there will be destructive interference with the first order transition. A higher Coulomb excitation yield can then be expected for a positive quadrupole moment. This effect can be observed in Figure 2.2

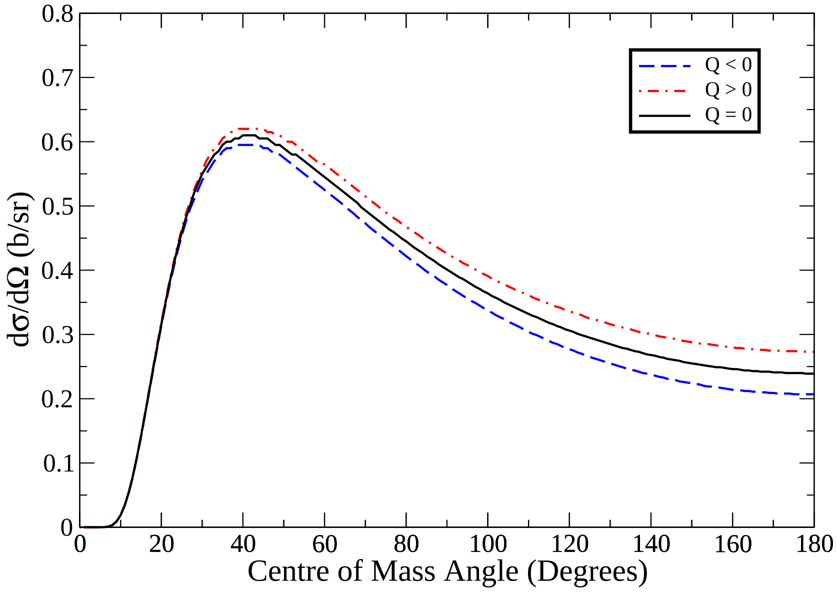

Figure 2.2: The effect of differing quadrupole moments on the differential Coulomb excitation cross section for a beam of ^{182}Hg bombarding a target of ^{112}Cd. The dashed blue line represents the differential Coulomb excitation cross section for a quadrupole moment f -1 eb; the dashed red line represents the differential Coulomb excitation cross section for a quadrupole moment f +1 eb; the solid black line represents the differential Coulomb excitation cross section for a quadrupole moment of 0 eb

which shows the differential Coulomb excitation cross section when a beam of ^{182}Hg bombards a target of ^{112}Cd and was calculated with the classical Coulomb excitation code *CLX*. A value of +1 eb was used for the positive quadrupole moment, whilst a value of -1 eb was used for the negative quadrupole moment. It is clear that as the centre of mass angle increases there is an obvious difference in cross section for differing values of quadrupole moment. It is this sensitivity that is exploited in the experiments described in Chapter 5.

The shape of an axially symmetric deformed nucleus can be described in terms of the quadrupole deformation parameter β_2, which is related to the eccentricity of an ellipse through the equation

$$\beta_2 = \frac{4}{3}\sqrt{\frac{\pi}{5}}\frac{\Delta R}{R_0}. \tag{2.47}$$

The intrinsic quadrupole moment, Q_0 can be written in terms of the β_2 parameter

[LC88] through the equation

$$Q_0 = \frac{3}{\sqrt{\pi(2\lambda+1)}} \cdot ZR_0^{\lambda}\overline{\beta_\lambda} \qquad \forall \quad \lambda \geq 2. \tag{2.48}$$

By assuming a uniform charge distribution, the quadrupole moment for an *E2* transition can be connected to the quadrupole deformation parameter β_2 through the formula

$$Q_0 = \frac{3}{\sqrt{5\pi}} ZR^2\beta_2\left(1 + 0.16\beta_2\right)e, \tag{2.49}$$

with Z the atomic number of the nucleus under consideration and $R = R_0A^{1/3}$ the nuclear radius. It can be seen from Equation 2.49 that the intrinsic quadrupole moment, Q_0 is directly proportional to the quadrupole deformation parameter β_2. A nucleus is labeled prolate in such a case where $Q_0 > 0$ or $Q_s < 0$ and oblate in the case where $Q_0 < 0$ or $Q_s > 0$. For the special case of an *E2* transition from the first excited 2^+ state to the 0^+ ground state the reduced transition probability can be related to the quadrupole deformation parameter by the equation

$$|\beta_2| = \frac{4\pi}{3} \cdot \frac{\sqrt{B(E2; 0^+_{\mathrm{gs}} \rightarrow 2^+_1)}}{R_0^2 Z} \tag{2.50}$$

meaning that the modulus of the quadrupole deformation parameter and thus the size of the deformation can be extracted solely from the reduced transition probability. It should be noted that only the *size* of the deformation can be extracted when using Equation 2.50. The *sign* of the deformation parameter cannot be extracted solely from the reduced transition probability. For this a measurement of the diagonal matrix element is required.

The reduced transition probability can also yield information on the mixing of nuclear states. If the wavefunctions are expressed in terms of a simple set of basis states that span the Hilbert space and are associated to the different intrinsic structures, it is possible to extract the mixing amplitudes from the experimental measurements of the reduced transition probability with ease. The reduced transition probability may be expressed as

$$B\left(E2; I_i \rightarrow I_f\right) = \left[\sum_{jk} \alpha_j^i \alpha_k^f \langle j|E2|k\rangle\right]^2 \tag{2.51}$$

with j,k denoting the unperturbed states and α_j^i and α_k^f the corresponding orthonormal mixing amplitudes. It should be noted that $\sum_j \alpha_j^2 = 1$. When using a simple two band mixing scheme where the initial state i is assumed to be a pure deformed state with a quadrupole moment of Q_0^i, the final state assumed to be mixed and interband transitions between unperturbed states forbidden then a relationship between the reduced transition probability, the quadrupole moment and the mixing amplitude can be obtained from Equation 2.52 and Equation 2.46

$$\sqrt{B\left(E2; I_i \rightarrow I_f\right)} = \alpha_j^f \sqrt{\frac{5}{16\pi}} \left\langle I_i K 20 | I_f 0 \right\rangle Q_0^i \tag{2.52}$$

The simplistic approach allows for the extraction of the mixing amplitudes for a given state purely from the measured electromagnetic properties. The two band mixing scheme is the most simplistic and has been applied to ^{186}Hg in [Dra94]. More complex mixing schemes have been developed to describe the observed level structures and transition probabilities of the light, even-even Hg isotopes such as those described in [WBD$^+$94] using the interacting boson model. Alpha decay hindrance factors have also been used [BBSD83] to obtain mixing factors in the light Hg region.

2.1.7 Experimental Method of Coulomb Excitation

It has been shown in the previous sections that the reduced transition probability and diagonal matrix elements that allow for the quadrupole moment, and therefore deformation, to be calculated, are related to the Coulomb excitation cross section. The calculation of the cross section (and therefore the matrix elements) in Chapter 5 relies on the excitation of both target and projectile nuclei. Matrix elements are determined by measuring the γ-ray yield of the transition $f \rightarrow i$ from the populated $|f\rangle$ state to the initial state $|i\rangle$ in coincidence with scattered projectile nuclei or recoiling target nuclei. The Coulomb excitation yields for both target and projectile are proportional to the integrated luminosity, L

$$L = N_B \left(\frac{N}{A}\right)_t, \tag{2.53}$$

where N_B is the number of incident beam particles and $(\mathrm{N/A})_t$ is the target thickness. The Coulomb excitation cross section for the projectile nucleus, which is the nucleus under investigation in the experiments described in Chapter 5, is determined by exploiting the fact that the γ-ray yield from the target transitions are proportional to the γ-ray transition yields from the projectile nucleus. This allows the unknown Coulomb excitation cross section for the projectile nucleus to be determined relative to the known Coulomb excitation cross section of the target nucleus. The γ-ray yield is defined as the number of detected γ rays in the germanium array. The following expressions define the γ-ray yield for the target and projectile respectively

$$N_\gamma^t = \epsilon_\gamma^t \cdot W_\gamma^t \cdot \sigma_{CE}^t \cdot L \cdot \epsilon_{exp}$$

$$N_\gamma^p = \epsilon_\gamma^p \cdot W_\gamma^p \cdot \sigma_{CE}^p \cdot L \cdot \epsilon_{exp} \tag{2.54}$$

with ϵ_γ the γ-ray detection efficiency and L the luminosity from Equation 2.53. Experimental uncertainties are contained within the factor ϵ_{exp}. The Coulomb excitation cross section, σ_{CE} is defined as

$$\sigma_{CE} = \int \left(\frac{d\sigma}{d\Omega}\right)_{CE} d\Omega \tag{2.55}$$

where the integral is taken over all solid angles covered by the particle detector. The term W_γ is the angular distribution correction factor. Due to the number of experimental uncertainties, an exact measure of the absolute cross sections are unfeasable. It is therefore preferable to exploit the fact that the ratio of the projectile and target Coulomb excitation cross sections is proportional to the ratio of the experimental γ-ray yields associated with the projectile and target nuclei. By taking a ratio of the expressions listed in Equations 2.54 an expression for the unknown Coulomb excitation cross section of the projectile nucleus can be obtained in terms of the known Coulomb excitation cross section of the target nucleus and the measured experimental γ-ray yields associated with the dexcitation of states with the target and projectile nuclei.

$$\sigma_{CE}^p = \frac{N_\gamma^p}{N_\gamma^t} \cdot \frac{\epsilon_\gamma^p}{\epsilon_\gamma^t} \cdot \frac{W_\gamma^p}{W_\gamma^t} \cdot \sigma_{CE}^t \tag{2.56}$$

By taking this ratio all systematic uncertainties associated with L and ϵ_{exp} have been eliminated and the unknown cross section has been made obtainable with the only required measurements being the experimental observed yields.

2.1.8 The GOSIA Analysis Code

The program capable of computing multiple Coulomb excitation yields, COULEX [AW66], used the semiclassical approximation to determine expected yields resulting from heavy-ion Coulomb excitation. The main limitation of this code is that it does not provide a method to determine matrix elements from measured experimental quantities, but rather a set of yields based on the input matrix elements. These matrix elements would be determined from a certain nuclear model, making the code effectively model dependent. The Coulomb excitation analysis code GOSIA [CCW83] provides a method of determining matrix elements directly from experimental measurements. The code is based on the semi-classical treatment of Coulomb excitation and performs a least-squared fit of matrix elements to experimental data in a model-independent manner. The measured yields of observed transitions in Coulomb excitation experiments are included in this least-squares fit, along with any other known quantities such as lifetimes, branching ratios and previously measured matrix elements. The following describes the main processes involved in determining matrix elements with GOSIA from measured experimental γ-ray yields.

Yield Determination

The first major step in the analysis of Coulomb excitation data with GOSIA is the determination of the integrated yields, representing the Coulomb excitation cross section. GOSIA first of all calculates the *point* yields, yields corresponding to a particular combination of particle scattering angle and γ-ray emission angle. Equation 2.57 is solved for every transition of interest by integrating around the possible ϕ_p particle scattering angles and summing over spherical harmonics.

$$Y_{point}(I \rightarrow I_f) = \int_{\phi_p} \frac{d^2\sigma(I \rightarrow I_f)}{d\Omega_p d\Omega_\gamma} d\phi_p \tag{2.57}$$

Calculations require initial matrix element values and angular attenuation factors, which describe the efficiency of the γ-ray detectors as a function of angle. Matrix elements are required for the dominant multipole orders of the transition of interest and for transitions linking the observed states to higher lying levels, to account for unobserved feeding to the level of interest. Diagonal matrix elements must also be defined.

Due to the γ rays emitted from excited nuclei being highly anisotropic, defining the location of the γ ray detectors is of great importance for the GOSIA χ^2 fit. Introducing angular attenuation factors, Q, to the yield integration allows for the probability of detecting a γ ray at a certain position to be determined. The attenuation factor, Q, is defined as

$$Q_k(E_\gamma) = \frac{J_k(E_\gamma)}{J_0(E_\gamma)}, \tag{2.58}$$

where

$$J_k(E_\gamma) = \int_0^{\alpha_max} P_k cos(\alpha) \left[\epsilon_{abs}(\alpha, E_\gamma)\right] sin\alpha d\alpha, \tag{2.59}$$

E$_\gamma$ the γ-ray energy, α the angle from the central axis of the HPGe detector, ϵ_{abs} the absolute γ-ray efficiency and P_k the Legendre polynomials.

GOSIA accounts for the energy loss experienced when ions travel through a thick target by means of incorporating stopping powers for the target material. Integrating over the energy and scattering angles transforms the point yields discussed earlier into yields that are comparable to the measured values. Taking the point yields defined in Equation 2.57 the fully integrated yields, $Y_{int}(I \rightarrow I_f)$ are defined as

$$Y_{int}(I \rightarrow I_f) = \int_{E_{min}}^{E_{max}} dE \frac{1}{\frac{dE}{dx}} \int_{\theta_{p_{min}}}^{\theta_{p_{max}}} Y_{point}(I \rightarrow I_f) sin(\theta_p) d\theta_p \tag{2.60}$$

with E_{min} and E_{max} being the minimum and maximum beam energies, $\theta_{p_{min}}$ and $\theta_{p_{max}}$ the minimum and maximum angles of the particle detector with respect to the beam axis. The integrated yields are expressed in units of $mb/srad.mg/cm^2$ and so are a measure of the Coulomb excitation cross section for the transition of interest.

χ^2 Minimization and Fitting of Matrix Elements

The calculated yields that incorporate the energy loss of nuclei passing through the target and the position of the HPGe detectors can be compared directly with the measured experimental yields. Matrix elements are then varied by GOSIA to find the optimum fit to the experimental data. The fitting procedure utilises a least-squares calculation to test trial solutions based on a χ^2 calculation. Optional data such as lifetimes and branching ratios can be incorporated, along with their experimentally determined error, to reduce the number of degrees of freedom. At each step in the χ^2 minimization values of these observables can be determined and compared to the measured values. If one defines data from previous experiments as $d_{exp} \pm \theta_d$ and the calculated values from the χ^2 minimization as d_{calc}, the full least-squares goodness of fit is given by

$$S = \sum_i \left(\frac{Y_i^{exp} - Y_i^{calc}}{\sigma_i^{exp}} \right)^2 + \sum_j \left(\frac{Y_j^{calc} - u}{u} \right)^2 + \sum_k \left(\frac{d_k^{exp} - d_k^{calc}}{\sigma_k^d} \right)^2 \tag{2.61}$$

Optimal values of all free matrix elements are found by minimizing the value of S. Errors on the matrix elements are found by determining the 1σ uncertainty ranges on these values. Off-diagonal, or correlated errors, can also be computed by GOSIA.

2.2 Lifetime Measurements

The lifetime of nuclear states range from 10^{15} years to below 10^{-15} seconds. It comes as no surprise that with such a large range there are a number of methods available to measure the lifetime of a nuclear state. For the experiments discussed in Chapter 4 the expected lifetime for the excited states of the nuclei are in the range of picoseconds. The appropriate method for measuring lifetimes is therefore

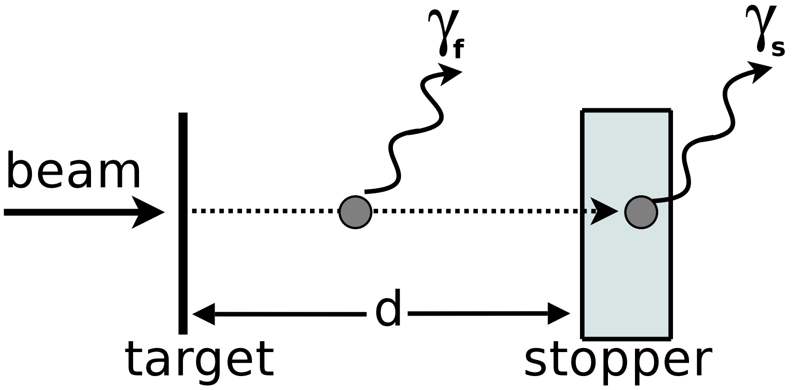

Figure 2.3: Recoiling nuclei created after an incident beam impinges upon a stationary target emit γ rays either before or after the stopper foil. The distance d impacts upon the relative intensities of the γ rays emitted before the stopper, γ_f and the γ-rays emitted when the nucleus has been fully stopped, γ_s.

the Recoil Distance Doppler Shift (RDDS) method and is discussed in detail in the following sections.

2.2.1 The Recoil Distance Doppler Shift Method

The Recoil Distance Doppler Shift (RDDS) method [SW68] is the standard method to measure lifetimes of excited nuclear states that are in the range of $\sim 10^{-12}$ - 10^{-8} s. The basic premise of this method relies on the fact that the mean lifetime, τ, of the nuclear state is related to the time required by a recoiling nucleus with a certain velocity v/c to travel a distance d. Recoiling nuclei produced when a beam impinges upon a stationary target travel a distance d before being stopped by the appropriately named stopper foil. Depending upon the lifetime of the excited state, γ rays are either emitted in flight before the nucleus reaches the stopper foil or after the nucleus has been stopped within the stopper foil. Figure 2.3 illustrates the principles explained. When γ rays are emitted before reaching the stopper foil they are subject to a Doppler shift while the energy of the γ rays emitted when the nucleus has been stopped is not. The energy of the Doppler shifted γ rays is given by the equation

$$E = E_0 \left[1 + \frac{v}{c} cos\theta \right], \tag{2.62}$$

where E_0 is the energy of the γ ray emitted at rest and θ is the angle of the emitted γ ray with respect to the direction of the velocity. It is therefore possible, when detecting γ rays at an angle θ with respect to the recoil direction to distinguish those emitted before reaching the stopper foil, γ_f, and those emitted when the nucleus has been stopped by the foil, γ_s. The intensity of a γ-ray transition is distributed between γ_f and γ_s. The intensity of the Doppler-shifted component is given by the relation

$$I_f = I_0 \left(1 - e^{-d/v\tau} \right), \tag{2.63}$$

while the intensity of the stopped component is given by

$$I_s = I_0 e^{-d/v\tau}. \tag{2.64}$$

The mean lifetime, τ, of an excited state can be found from measurements of I_f and I_s. The fraction of the γ-ray intensity in the stopped component shows an exponential dependence on the lifetime

$$\frac{I_s}{I_s + I_f} = e^{-d/v\tau}. \tag{2.65}$$

The mean lifetime can be found as a function of distance using this ratio if the recoil velocity, v is known.

Equation 2.65 assumes that the excited state of interest is populated promptly and that no side feeding occurs. To account for such feedings the Differential Decay Curve method (DDCM)[DHvB89, PHD$^+$92] is used and applied to the RDDS measurements.

2.2.2 The Differential Decay Curve Method

The Differential Decay Curve method (DDCM) uses the intensities of the flight and stopped components of the γ-ray transition to obtain the mean lifetime of the

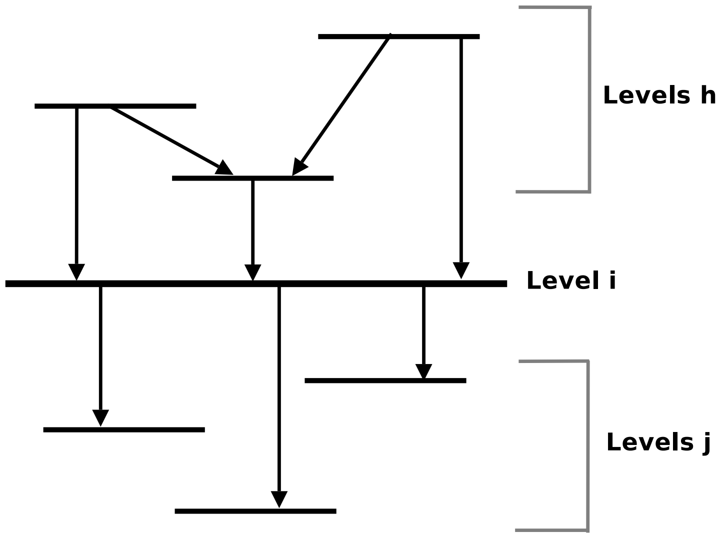

Figure 2.4: Schematic representation of feeding and depopulating transitions to a level i where the DDCM will be used to obtain the mean lifetime, τ.

state of interest. The results discussed in Chapter 4 are from an experiment where a degrader foil was used in place of the stopper foil. This allowed for the recoiling nuclei to be detected in downstream detectors. In terms of a discussion on the DDCM the stopped components in the following equations have been replaced with “degraded components”.

If all direct feeding transitions to the level of interest are known the lifetime of the excited state can be found by considering a single, first order differential equation of quantities, which are obtained in the experimental measurements. When measuring using multiple target to degrader distances, d, illustrated in Figure 2.3, the mean lifetime of the excited state, τ is found using

$$\tau_i(d) = -\frac{R_{ij}(d) - b_{ij}\sum_h R_{hi}(d)}{vdR_{ij}(d)/dt}, \tag{2.66}$$

where $R_{ij}(d)$ is the intensity of the degraded component of the transition from level i to level j, $R_{hi}(d)$ the degraded component of the transition that directly feeds i, the level of interest and b_{ij} the branching ratio of the transition from i to j. An illustrative level scheme depicting transitions that feed and depopulate the level of interest is shown in Figure 2.4. R_{ij} is related to the decay constant

λ_i through the formula

$$R_{ij}(d) = b_{ij} \int_t^{\infty} n_i(t) dt \tag{2.67}$$

with $n_i(t)$ being the number of nuclei in a given state i. The values for the derivative $\frac{dR_{ij}(d)}{dt}$ in Equation 2.66 are easily obtained from the measured decay curve when fitting a smooth polynomial through the data points. In RDDS measurements spectra are commonly obtained at multiple target-to-degrader distances, allowing for the fully Doppler shifted components $I^s_{ij}(d)$, and the degraded components $I^d_{ij}(d)$ to be obtained for the transition in various ratios. It is useful in the analysis of such data to introduce the relative quantity $Q_{ij}(d)$ which is defined as

$$Q_{ij}(d) = \frac{R_{ij}(d)}{R_{ij}(0)} = \frac{I^d_{ij}(d)}{I^d_{ij}(d) + I^s_{ij}(d)} \tag{2.68}$$

and can be obtained from measured quantities. Using $Q_{ij}(d)$ Equation 2.66 can be rewritten as

$$\tau_i(d) = -\frac{Q_{ij}(d) - b_{ij} \sum_h [J_{hi}/J_{ij}] Q_{hi}(d)}{v dQ_{ij}(d)/dt} \tag{2.69}$$

with J_{hi} is the relative intensity of the γ-ray transition from level h to level i and J_{ij} the relative intensity of the γ-ray transition from level i to level j. A full description of the method and the derivations of formula quoted here can be obtained from reference [DHvB89].

Chapter 3

Experimental Techniques and Facilities

The following chapter gives an overview of techniques common to both experiments discussed in Chapter 4 and Chapter 5 such as γ-ray spectroscopy and an overview of the experimental facilities used to obtain the data analysed in Chapter 4 and Chapter 5. The setup at the Jyväskylä accelerator laboratory will be discussed in detail along with the Köln plunger, which was the unique aspect of the experimental setup, to give context to the experiment performed to measure lifetimes of excited states in the light Hg isotopes described in Chapter 4. The REX-ISOLDE facility at CERN is described for the purposes of the Coulomb excitation measurements described in Chapter 5.

3.1 Nuclear Production

Nuclei can be produced in a number of ways. Of interest for the purposes of this thesis are two methods, which will be discussed separately. The method used to produce the Hg nuclei that were used in the Coulomb excitation experiments performed at REX-ISOLDE was the ISOL technique. The method employed to produce the Hg nuclei at the Jyväskylä accelerator laboratory for the purposes of the lifetime measurements was the fusion-evaporation technique.

3.1.1 Isotope Separation On-Line

Isotope Separation On Line (ISOL) production of radioactive beams is now employed in many leading facilities such as TRIUMF and REX-ISOLDE. Before describing the REX-ISOLDE facility in detail, it is the objective of this section to give a general overview of the ISOL technique.

The production of nuclei through the ISOL technique usually starts with the acceleration of light particles such as protons or α-particles. Such particles then impinge upon a thick primary target, which in the case of the experiment described in Chapter 5 was uranium-carbide. Upon impact a wide range of nuclei are formed through three processes: spallation, fission and fragmentation. The favoured process is largely dependent upon the energy at which the particles bombard the primary target. Spallation requires high energies to take place, typically $\geq$500 MeV. When particles of such an energy impinge upon the primary target nucleons are knocked out or 'boiled off' due to the heat of the collision. The target nuclei then produce a few large residual products and a large number of free nucleons. It is then common for an ionising source to remove electrons from the nuclei that have diffused through the primary target so as they can be easily accelerated and steered. To reduce the number of species in an ionised beam, the ions are separated by their charge-to-mass ratio. This produces, often pure, beams of isotopes consisting of a single mass, A in a singly-charged ionised state. It should be noted that though much is done to make the beam as pure as possible contaminants from mass multiples in higher charged states are possible. After producing a single-species beam, the ions are then transported to the experimental station as required, or post-accelerated.

3.1.2 Fusion Evaporation

Experiments described in Chapter 4 have employed a rather different technique than that of ISOL production to obtain the relevent nuclei for experimental study. *Fusion evaporation reactions* were employed to produced Hg nuclei in highly ex-

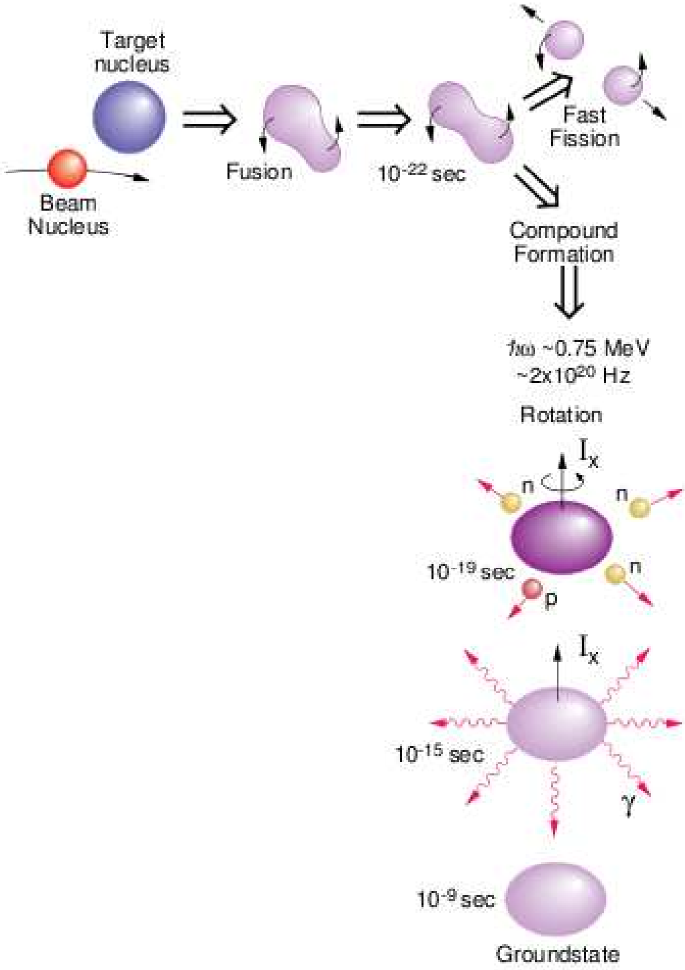

Figure 3.1: Schematic representation of the various stages in a fusion evaporation reaction along with typical time scales. [Pau]

cited states. In such reactions, target and projectile nuclei fuse to form a compound nucleus with a high angular momentum and excitation energy. There are several stages to such a reaction. These stages are highlighted in Figure 3.1. With sufficient energy to overcome the Coulomb barrier, the colliding target and projectile nuclei will fuse to form an intermediate compound nucleus. The compound nucleus is formed in a highly excited state and is often rotating, giving the compound nucleus a certain amount of angular momentum. The specific angular momentum is characterised by the impact parameter b. After the formation of the compound nucleus numerous decay channels become available so as energy and angular momentum can be minimized. The nucleus may undergo fission or multi-fragmentation. The compound nucleus may also decay through *particle evaporation*. Occurring approximately 10^{-19} seconds after the formation of the compound state, light particles such as protons, neutrons or α-particles are emitted from the system when they gain a sufficient amount of energy to overcome the Coulomb barrier. Typically these light particles take 8-10 MeV from the compound nucleus, reducing the total energy and forming new residual nuclei. This process takes little angular momentum from the system and is hindered when the total energy of the system is below the particle evaporation threshold, $\approx$8 MeV. When particle evaporation is no longer energetically favoured, the residual nuclei will decay by emitting γ rays. This process typically occurs 10^{-15} seconds after the formation of the compound state. The decay occurs at first through *statistical* or *cooling* γ rays. These are usually high-energy electric dipole γ-ray transitions that take a large portion of energy away from the system but little angular momentum. As the nucleus approaches the yrast region γ-ray emission continues through discrete low-energy transitions that carry a larger amount of angular momentum away from the system. These transitions will be within, or near to the yrast line and will continue until the nucleus reaches its ground state. It is these discrete transitions that carry information on the structure of the nucleus and are of importance to the work described in Chapter 4.

3.2 γ-Ray Spectroscopy and Related Topics

As a γ ray is uncharged it cannot be detected directly. The detection of γ rays is therefore dependent on an interaction with the detector medium that transfers all or part of the γ ray energy. The three primary interactions types of interaction, *photoelectric absorption*, *Compton scattering* and *pair production* are discussed in this section. Much has been written on these three topics and overviews can be found in such publications as [Kno00]. Therefore only the main characteristics of these three process are given. Related topics to γ-ray spectroscopy such as selection rules and internal conversion are covered along with a brief introduction to Germanium detectors and arrays. This is intended to lead the reader into the experimental setups discussed in §3.3 and §3.4.1.

3.2.1 Interaction With Matter

Photoelectric Absorption

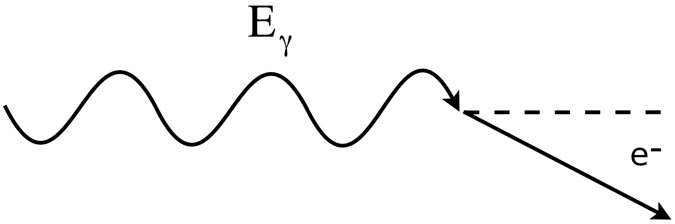

Figure 3.2: Schematic representation of photoelectric absorption.

The process of photoelectric absorption is shown in Figure 3.2. During this process an incident photon undergoes an interaction with an atom of the absorber material such that the photon energy is converted and an atomic electron is ejected by the atom. This ejected electron is known as a photoelectron and must be bound to the atom to in order to conserve energy and momentum. The energy of the photoelectron (E_{e^-}) is given by,

$$E_{e^-} = h\nu - E_{be} \tag{3.1}$$

where E_{be} is the binding energy of the photoelectron. This process creates a ionised absorber atom with a hole, which is quickly filled either through a rearrangement of the other electrons resulting in a cascade of X rays, or capture of a free electron. The probability of the photoelectric process occurring depends on both the atomic number of the absorber atom Z, and the energy of the incident photon. The absorption probability can be approximated as:

$$\tau \propto \frac{Z^n}{E_\gamma^{3.5}} \tag{3.2}$$

where n varies between 4 and 5 for a given energy region. This is derived from empirical observations [Kra88]. The strong dependence on Z is why high Z materials such as lead are used for shielding. Photoelectric absorption is the prefered mechanism of the three main interactions processes as all the energy of the incident photon is deposited in the detector. However, it is only dominant for low energy photons (<200 keV) as the probability is inversely proportional to energy.

Compton Scattering

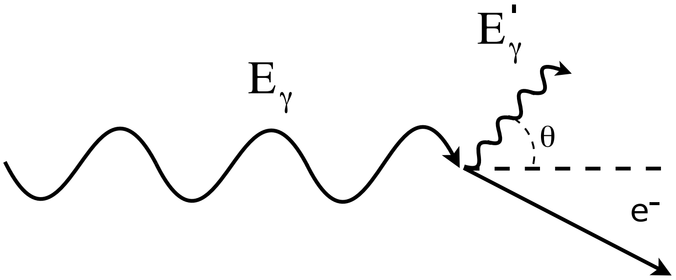

Figure 3.3: Schematic representation of Compton scattering.

The process of Compton scattering is shown in Figure 3.3. Here an incident γ ray scatters from an electron in the absorber material at an angle θ to the incident direction, and some portion of the γ-ray energy is relinquished to the electron. Applying conservation of energy and momentum, the following expression can be derived for the energy of the Compton scattered photon,

$$E_\gamma^{'} = \frac{E_\gamma}{1 + (\frac{E_\gamma}{m_0 c^2})(1 - cos\theta)}, \tag{3.3}$$

where E$_\gamma$ is the energy of the incident photon, E$_\gamma^{'}$ is the energy of the scattered photon, θ is the scattering angle and m$_0 c^2$ is the rest mass of the electron. The expression for the energy of the scattering electron is given by

$$T_e = E_\gamma - E_\gamma^{'} = \frac{E_\gamma^2 (1 - cos\theta)}{m_0^2 + E_\gamma (1 - cos\theta))}. \tag{3.4}$$

The scattered photon is left with a range of possible energies which leads to the production of a Compton continuum. If the incident γ ray deposits energy in the detector via this method and then scatters out of the detector, only the energy from the scattered electron will be detected. The continuum extends up to an energy defined by the maximum energy transfer, where there is a sharp cut off point known as the Compton edge.

Compton scattering is the most probable process for γ rays of intermediate energy (~200 keV - 5 MeV), the probability decreases rapidly for increasing energy. The probability of Compton scattering per atom of absorber material depends on the number of atoms available as scattering centres, and therefore increases linearly with Z. The probability of Compton scattering at any given angle of θ can be given by the Klein-Nishina formula [KN29] for the differential scattering cross section $\mathrm{d}\sigma/\mathrm{d}\Omega$:

$$\frac{d\sigma}{d\Omega} = Zr_0^2 \left(\frac{1}{1+\alpha(1-cos\theta)}\right)^2 \left(\frac{1+cos^2\theta}{2}\right) \left(1+\frac{\alpha^2(1-cos\theta)^2}{(1+cos^2\theta)[1+\alpha(1-cos\theta)]}\right) \tag{3.5}$$

where Z is the atomic number of the incident material, α is the photon energy in units of the electron rest-mass energy ($\alpha = \mathrm{E}_\gamma\ /\mathrm{m}_0^2$) and r_0 is the classical electron radius, $\mathrm{r}_0 = 2.818\,\mathrm{fm}$. There is a strong tendency for high energy γ rays to be forward scattered.

Pair Production

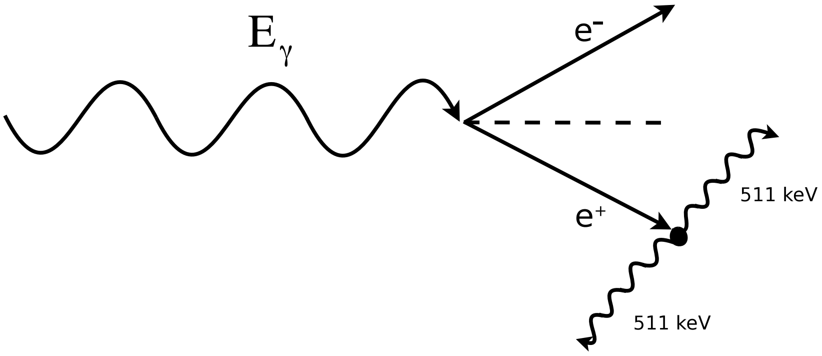

Figure 3.4: Schematic representation of pair production.

The third interaction mechanism, known as pair production is shown in Figure 3.4. If the incident γ ray has an energy greater than 1.022 MeV, twice the rest mass of the electron, in the field of the atomic nucleus an electron-positron pair can be created. Any remaining energy from the γ ray is distributed evenly between the electron-positron pair. As the positron slows to thermal energies by interaction with the absorbing material, annihilation can occur with one of the atomic electrons. This produces two 511 keV γ rays, which are either absorbed or able to escape from the detector. If one of the 511 keV γ rays escape, a single escape peak is observed at E$_\gamma$-m_0c^2 and if both escape a double escape peak at E$_\gamma$-2m_0c^2. This process only becomes significant for high energy γ rays (5-10 MeV).

3.2.2 Selection Rules and Single-Particle Estimates

To study the properties of a nucleus it is the electromagnetic force that is often used, rather than the strong nuclear interaction. The transition from a state I_i to I_f in an excited nucleus results in an electromagnetic photon being produced. This photon has an energy equal to the difference in energy between states I_i and I_f, when the small recoil energy is neglected, and has a certain parity and multipole order associated to it. Selection rules govern which transitions are allowed between certain states. The angular momentum selection rule governs the allowed multipolarity of transitions between excited states. For an initial state with spin I_i and a final state with spin I_f

$$|I_i + I_f| \geq L \geq |I_i - I_f|, \tag{3.6}$$

where L is the multipole of the transition. For a pure γ-ray transition $L \neq 0$ due to the intrinsic spin of the photon. Though a number of multipole transition are possible, often lower order multipoles are favoured. This can be seen in Table 3.1 depicting transition rates and Weisskopf estimates. A *stretched* transition occurs when a γ ray carries off the difference in angular momentum between the two states.

The parity of the photon is determined by the following selection rules

$$\begin{gathered} \pi(ML) = (-1)^{L+1}, \\ \pi(EL) = (-1)^{L}. \end{gathered} \tag{3.7}$$

It therefore follows that no change in parity occurs for an even electric or odd magnetic transition.

The interaction between the electromagnetic field and the nucleus causes a change in nuclear state. The transition rate for the emission of a photon is given by

$$T_{if}(\mathcal{M}L) = \frac{8\pi(L+1)}{\hbar L((2L+1)!!)^2} \left(\frac{E_\gamma}{\hbar c}\right)^{2L+1} B(\mathcal{M}L : I_i \rightarrow I_f) \tag{3.8}$$

where $\mathcal{M}$ represents electric or magnetic radiation, E_γ the energy of the emitted photon, L the mulitpole of the transition and $B(\mathcal{M}L : I_i \rightarrow I_f)$ the reduced transition probability. The lifetime of an excited nuclear state is strongly dependent on the multipolarity of the γ-ray transitions by which it can decay. By assuming that a single nucleon changing from one shell state to another is responsible for the observed transition an estimate can be obtained for the state's half-life. The Weisskopf estimates listed in Table 3.1 are the most common estimate used.

Weisskopf Estimates	
$\lambda(E1) = 1.0 \times 10^{14} A^{\frac{2}{3}} E^{3}$	$\lambda(M1) = 5.6 \times 10^{13} E^{3}$
$\lambda(E2) = 7.3 \times 10^{7} A^{\frac{4}{3}} E^{5}$	$\lambda(M2) = 3.5 \times 10^{13} A^{\frac{2}{3}} E^{5}$
$\lambda(E3) = 34 A^{2} E^{7}$	$\lambda(M3) = 16 A^{\frac{4}{3}} E^{7}$
$\lambda(E4) = 1.1 \times 10^{-5} A^{\frac{8}{3}} E^{9}$	$\lambda(M4) = 4.5 \times 10^{-6} A^{2} E^{9}$

Table 3.1: Weisskopf estimates for single-particle transition rates. $\lambda(\mathcal{M}L)$ are in units of s^{-1} and E in units of MeV.

These estimates are not exact calculations of the transition rates, but do serve to provide values that can be compared to experimental measurements.

The electromagnetic transitions between nuclear states may result from only one or a few particles changing their state, or form a collective motion whereby many particles within the nucleus change their state. It is from measuring transition probabilities that one can gain an insight into the magnitude of collective motion within a certain nucleus. It is the general case that a large reduced transition probability is indicative of collective motion and a small reduced transition probability is indicative of single particle behaviour. By comparing the observed electromagnetic transition rates with the Weisskopf single-particle estimates the degree of collectivity can be inferred. The collective transition rates listed in Table 3.2 are shown in terms of the reduced transition probabilities. The ratio of experimental $B(\mathcal{M}L)$ values to those predicted in Table 3.2 will allow for the reduced transition probabilities to be expressed in *Weisskopf units*. This in turn will be an approximation to the number of nucleons involved in the transition and therefore an indication of collectivity.

Collective Transition Rate Estimates	
$\lambda(E1) = 1.59 \times 10^{15} B(E1) E^3$	$\lambda(M1) = 1.76 \times 10^{13} B(M1) E^3$
$\lambda(E2) = 1.22 \times 10^{9} B(E2) E^5$	$\lambda(M2) = 1.35 \times 10^{7} B(M2) E^5$
$\lambda(E3) = 5.67 \times 10^{2} B(E3) E^7$	$\lambda(M3) = 6.28 B(M3) E^7$
$\lambda(E4) = 1.69 \times 10^{-4} B(E4) E^9$	$\lambda(M4) = 1.87 \times 10^{-6} B(M4) E^9$

Table 3.2: Collective transition rate estimates. $\lambda(\mathcal{M}L)$ are given in units of s^{-1}, B(EL) in units of e^2fm^{2L}, B(ML) in $\mu_n^2 fm^{2L+1}$ and E in MeV

3.2.3 Internal Conversion

A competing electromagnetic process to γ-ray emission is *internal conversion.* In this process the excitation energy of the nucleus is transferred to an atomic electron causing it to be emitted from the nucleus. The kinetic energy of the electron, T_e is thus given by the difference between the transition energy, $\Delta E = E_i - E_f$ and the binding energy of the electron, B_e

$$T_e = \Delta E - B_e. \tag{3.9}$$

Electrons in different atomic orbits will have different binding energies. It is therefore possible that for a given transition there are several possible electron energies. Consideration of Equation 3.9 shows that internal conversion can only occur if the excitation energy exceeds the binding energy of the electron for the particular shell it is frequenting. Conversion electrons are labelled by the shell in which the originated. The K, L and M shells, used so often in atomic physics to describe electron orbits, correspond to the principle quantum numbers *n = 1, 2, 3,*. Labelling of electrons as, for example, L_I, L_{II} and L_{III} takes into account shell substructure and corresponds to electrons originating from the $2s_{1/2}$, $2p_{1/2}$ and $2p_{3/2}$ sub shells respectively. The internal conversion process is accompanied by the emission of characteristic X-rays. The vacancy left in an atomic shell by the emission of a conversion electron is filled by an electron form a higher shell. It is the difference in energy of the two shells that correspond to the energy of the emitted X-ray. The probability of internal conversion relative to γ-ray emission is given by the *internal conversion coefficient*, α, defined as

$$\alpha = \frac{\Gamma_e}{\Gamma_\gamma}, \tag{3.10}$$

where Γ_e is the internal conversion rate and Γ_γ is the γ-ray emission rate. The total transition rate, Γ_t is therefore given by the sum of the internal conversion rate and the γ-ray emission rate

$$\Gamma_t = \Gamma_e + \Gamma_\gamma = \Gamma_\gamma(1+\alpha) \tag{3.11}$$

Internal conversion coefficients are dependent on three factors: the principle quantum number n, the atomic number Z and the transition energy. The approximate dependencies are summarised for the most relevent contributions in this work, *E2* and *M1* transitions

$$\begin{aligned} \alpha(E2) &\propto \frac{Z^3}{n^3 E_\gamma^{\frac{9}{2}}}, \\ \alpha(M1) &\propto \frac{Z^3}{n^3 E_\gamma^{\frac{3}{2}}}. \end{aligned} \tag{3.12}$$

The relations in Equation 3.12 show that internal conversion due to a magnetic transition is often much larger than for an electric transition, for a given multipole order. It can be seen that internal conversion is most important when considering low energy transitions in large-Z nuclei, with the largest contribution coming from *n=1* K shell electrons. Internal conversion has a strong dependence on multipolarity. Equation 3.12 shows that for a transition of a given energy, internal conversion due to a M1 component will be greater than that due to an E2 component by a factor of E_γ^3.

Observed γ-ray intensities must be corrected for internal conversion. Conversion coefficients have been calculated and tabulated in a variety of publications, though those of [RFAP78] have been used in this work.

3.2.4 Germanium Detectors

Energy resolution and efficiency is of great importance for γ-ray spectroscopy. The material that has been employed in the experiments described in this work

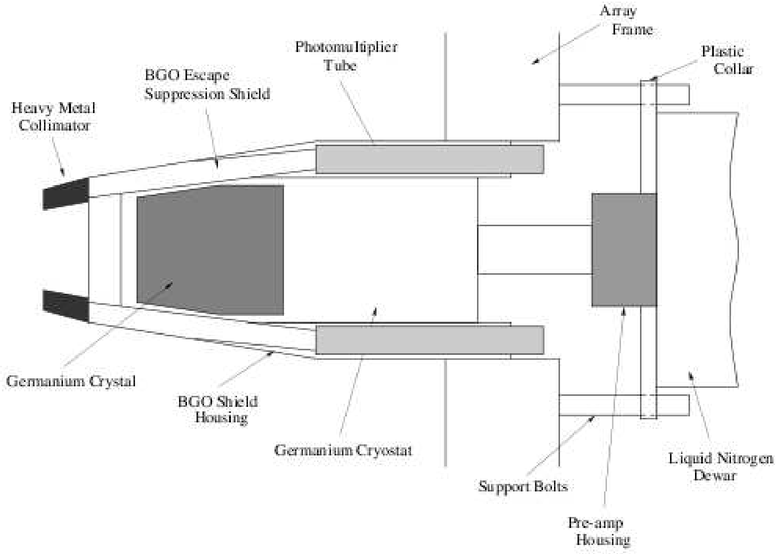

Figure 3.5: Schematic representation of a High Purity Germanium detector.

for the purposes of γ-ray detection is High Purity Germanium (HPGe). HPGe detectors are reverse biased p-n junction diodes. Any γ rays interacting with the germanium will produce electron-hole pairs in the depletion region. The electric gradient across this region causes the migration of electrons and holes and therefore produces a detectable electric current. The use of reverse bias maximises the depletion region and therefore increases the active region of the detector.

To further enhance the active volume of a HPGe crystal the shape can be modified. The most common crystal geometry is a closed-end coaxial with tapered front end corners. This minimises areas of low electric field, which can occur at sharp corners. Figure 3.5 shows a schematic representation of a typical HPGe detector with an escape suppression shield.

HPGe detectors are cooled to 77 K using a cold finger extending from a LN_2 dewar. With such a small band gap in Ge, thermal leakage current increases rapidly with temperature. It is therefore important to operate HPGe detectors at very low temperatures to reduce this effect.

A typical HPGe detector can achieve an energy resolution of $\approx 2.5 - 3.0$ keV at

1.3 MeV. As the energy required to produce an electron-hole pair in Ge is much lower than the typical energy of a γ ray it encounters a multiple of electron-hole pairs are produced for each incident γ ray, lowering statistical fluctuations and giving much higher resolution.

3.2.5 Compton Suppression

It is the feature of some, though not all, HPGe detectors to employ some form of Compton suppression shield. Due to the finite size of a HPGe detector, some γ rays may not impart all of their energy into the detector medium. γ rays may Compton scatter out of the detector or pass through completely undetected. Scattered γ rays will contribute to the total background and decrease detection efficiency. To counteract this effect, scintillators such as bismuth germanate (BGO) are used in anti-coincidence with the HPGe detectors. Though BGO has poor energy resolution it has excellent timing properties and is therefore an ideal medium for coincidence detectors. If a γ ray is detected in the HPGe crystal and in coincidence with the BGO shields then the signal will be rejected. This does not effect photopeak efficiency significantly and reduces the Compton continuum. This has the advantage of increasing the peak-to-total ratio. The increase can be as much as ≈20% -50% in singles spectra [BFF+92]. One other advantage of BGO as a suppression shield is its high density. A relatively small amount of the material is required to fully stop a scattered γ ray. This becomes important if one wishes to pack several detectors together closely to form an array.

3.2.6 Detector Arrays

To increase detection efficiency HPGe detectors are often mounted in arrays. These arrays are designed to cover as much of the 4π solid angle as possible. A measure of the quality of spectra obtainable with an array is given by the *resolving power* R, which is defined as

$$R = \left(\frac{SE_\gamma}{\Delta E_\gamma}\right) PT, \tag{3.13}$$

where SE_γ is the average energy separation between γ rays in a cascade, ΔE_γ is the full width at half-maximum (FWHM) of the measured γ rays and PT is the peak-to-total ratio. It is clear that the peak-to-total ratio plays a significant part in the resolving power of an array, though in practice it is difficult to increase. A more controlable factor in the resolving power of an array is ΔE_γ, which has four major contributing factors

- The intrinsic resolution of the detector system, ΔE_I, which takes into account the individual properties of the detector.
- Doppler broadening due to the opening angle of the detectors, ΔE_D. Segmentation of detectors can improve this quantity, as can clustering of detectors.
- Doppler broadening due to the angular spread of recoils, ΔE_R. Improvements can be made with kinematic corrections.
- Doppler broadening due to the velocity distribution of recoils, ΔE_V.

The final energy resolution of the detector array is found from summation of these four factors in quadrature

$$\Delta E_\gamma = \sqrt{\Delta E_I^2 + \Delta E_D^2 + \Delta E_R^2 + \Delta E_V^2} \tag{3.14}$$

In order to resolve a peak in a given spectrum it must stand above the background and be statistically significant. One way to help improve this is to be further selective of the γ rays one lets into the spectrum. The use of ancillary devices such as recoil separators can help reduce background further.

3.2.7 Recoil Separators

Recoil separators are designed to separate the nuclei of interest inflight from the primary beam particles and other fusion-evaporation products. Magnetic and electric fields separate the different products by their mass-to-charge ratio. In a magnetic field the track of a charged particle is defined by the Lorentz force. If a particle with electric charge q and mass m moves through a homogeneous

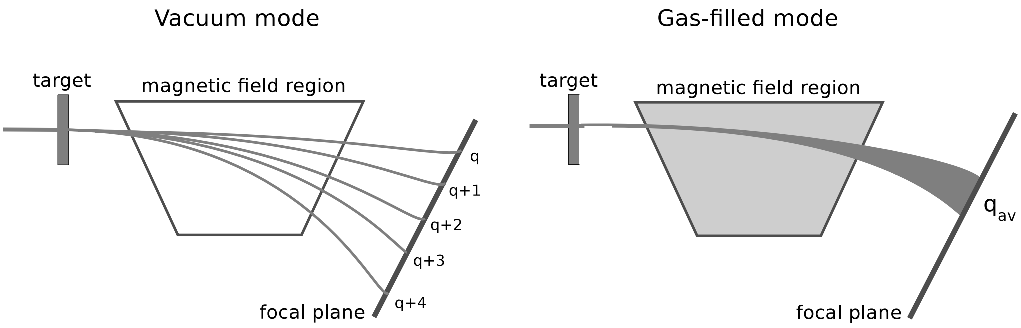

Figure 3.6: The main differences between vacuum and gas-filled recoil separators. It can be seen that vacuum separators have a higher resolution power, though are not as efficient at transmitting ions to the focal plane.

magnetic field B with a velocity v then the particle track radius is defined as

$$\rho = \frac{mv}{qB}. \tag{3.15}$$

Recoil separators can be run in vacuum mode or gas-filled mode (see Figure 3.6). In vacuum mode recoil separators, the spatial distribution of the recoils is wide. It is therefore not possible to focus the recoils of interest through the separator without significant losses. Though only a few charge states can be guided to the focal plane, an advantage of the vacuum mode is the high resolving power obtainable. This can be advantages for many experiments.

To avoid the effect of broad charge state distribution, a recoil separator can be filled with gas. In a gas-filled separator heavy ions undergo collisions that change the initial charge state of the ion. The charge state of the ions tends towards a mean value, q_{av}. The ions then proceed along the same trajectory determined by the average charge state. Defining the average charge to be

$$q_{av} = \frac{v}{v_0} Z^{\frac{1}{3}} \tag{3.16}$$

if v is in the range

$$1 < \frac{v}{v_0} < Z^{\frac{2}{3}} \tag{3.17}$$

and substituting into Equation 3.15, an expression for the magnetic rigidity of the separator can be obtained

$$B\rho = \frac{mv}{q_{av}} \approx 0.0227\frac{A}{Z^{\frac{1}{3}}}, \tag{3.18}$$

where v_0 is the Bohr velocity, $2.19{\times}10^6\,\mathrm{ms}^{-1}$. The nuclei studied in Chapter 4 were Z=80 Hg nuclei and had an approximate velocity of 0.04c, hence the approximation is valid [GYL$^+$88].

Equation 3.18 illustrates two important properties of gas-filled separators: the magnetic rigidity is independent of velocity and of the initial charge distribution of the particles. Due to this the spatial distribution of recoils after separation is narrower and so the recoil collection efficiency is higher than in vacuum mode. A disadvantage of gas-filled separators is the lack of mass resolving power. Typical mass resolution for gas-filled separators is ≈10%, which is only enough to separate the recoiling nuclei from the primary beam. Fortunately for the experiments described in Chapter 4 this was all the resolving power required.

3.3 Jyväskylä Setup

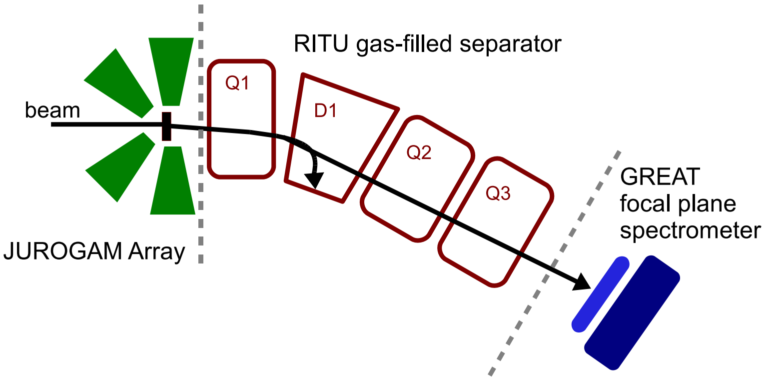

Figure 3.7: Schematic representation of the experimental setup for lifetime measurements performed at the University of Jyväskylä. The Köln plunger is located at the target position of the JUROGAM array.

Lifetime measurements of excited states in ^{182}Hg were performed at the University of Jyväskylä accelerator laboratory. The inhouse setup of the JUROGAM HPGe array, the RITU gas-filled separator and the GREAT focal plane detector were used in conjunction with the Köln plunger device. Figure 3.7 shows a schematic representation of the experimental setup and how the pieces of equipment couple together. In this section a description of each piece of equipment will be given along with technical details.

3.3.1 JUROGAM HPGe Detector Array

Figure 3.8: The JUROGAM detector array at the University of Jyväskylä

In order to detect prompt γ rays from excited nuclear states JUROGAM HPGe detectors are placed in a spherical array around the target position. This array is located at the entrance to RITU, the gas-filled separator. JUROGAM consists of 43 HPGe detectors, each with BGO Compton suppression shielding. A combination of EUROGAM Phase I [BFF$^+$92] and GASP type [Alv93] detectors have been used to build the array. EUROGAM Phase I detectors have a typical diameter of 69 - 75 mm and a length $\geq$70 mm. GASP type detectors are of a similar size, though slightly larger due to a thicker BGO shielding component. The efficiency of JUROGAM detectors varies from 65% - 85% relative to a 3 x 3 inch NaI detector measuring 1332 keV γ rays at a distance of 25 cm. The energy

JUROGAM Detector Positions		
Position	**Number of Detectors**	**Angle w.r.t. Beam Line**
Ring 1	5	157.6°
Ring 2	10	133.6°
Ring 3	10	107.9°
Ring 4	5	94.2°
Ring 5	5	85.8°
Ring 6	8	78.1°

Table 3.3: The position and angles of the 43 HPGe detectors in the JUROGAM array.

resolution as FWHM is between 2.5 keV and 3.0 keV at 1332 keV. The standard target chamber was replaced by the Köln plunger device, which is discussed in § 3.3.5.

The detector frame is based on an array of regular pentagons with the HPGe detectors placed at differing angular positions with respect to the beamline. The number of detectors at each position is summarised in Table 3.3. For the work described in Chapter 4 detectors at angles close to 90° were unable to provide a sufficiently large Doppler shift to perform lifetime measurements using the RDDS method. Therefore only detectors in Ring 1 and Ring 2 were used in the analysis of the data.

3.3.2 The RITU Gas-Filled Separator

Figure 3.9: The Recoil Ion Transport Unit RITU in position at the University of Jyväskylä.

The gas filled recoil separator RITU (Recoil Ion Transport Unit) [LÄE^{+}95, Lei97] provides the required separation of primary beam from the recoiling nuclei. The separator consists of three quadrupole magnets (Q) and one dipole magnet (D) arranged in a QDQQ configuration with a total length of 4.8 m. The first quadrupole magnet is used to focus the recoil cone vertically, as the acceptance angle to the dipole magnet is relatively small at 10 msr. The dipole magnet then separates the beam particles from the recoiling nuclei as described in § 3.2.7. The remaining quadrupole magnets focus the recoiling nuclei to the focal plane detectors. RITU is filled with He gas with an approximate pressure of 1 mbar. The high vacuum beam line is separated from gas volume using either a differential pumping system or a carbon foil. In the present work a carbon foil was used.

In the A$\sim$180 mass region RITU provides a short separation time, which can be of the order 0.5 μs. and a transmission efficiency in the region of 10 - 30%.

3.3.3 The GREAT Focal Plane Spectrometer

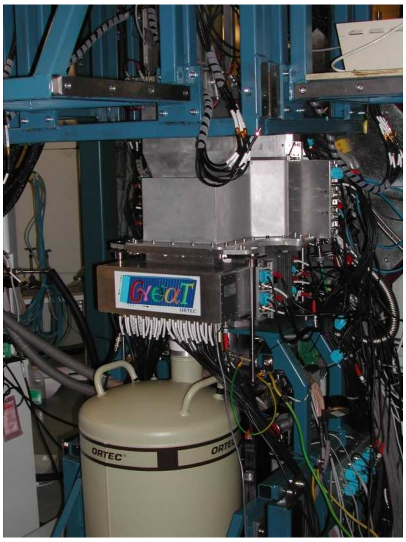

Figure 3.10: The GREAT focal plane spectrometer at the University of Jyväskylä.

The Gamma Recoil Electron Alpha Tagging (GREAT) spectrometer [PAA$^+$03] is a focal plane detector array designed primarily for tagging experiments. The spectrometer has the ability to detect the implanted recoils and perform spatial and temporal correlations of subsequent radioactive and electromagnetic decays involving the emission of α particles, β particles, protons, γ rays, X-rays and conversion electrons. The GREAT spectrometer, shown in Figure 3.10, consists of a multiwire proportional counter (MWPC), two double-sided silicon strip detectors (DSSDs), 28 PIN diodes, a planar Ge detector and a clover Ge detector positioned behind the planar detector.

The MWPC located at the entrance of GREAT has two mylar windows measuring 131 mm x 50 mm acting as entrance and exit windows and is filled with isobutane gas. Energy loss, timing and position signals are generated when recoils pass through the MWPC. Upon exiting the MPWC recoils are implanted into two DSSDs, each with an active area of 60 mm x 40 mm and a thickness of 300 μm. 60 vertical and 40 horizontal strips of 1 mm width provide 4800 detector pixels. This high granularity provides an estimated recoil efficiency of $\approx$80%. The DSSDs provide a measurement of the energy of the implanted recoil as well as measurements of subsequent α, β or proton decays. Coupling the DSSD information with the MWPC information allows for the clean separation of recoiling fusion products from scattered beam particles. This allows for a much cleaner spectrum through the employment of the recoil tagging technique. GREAT also has the ability to detect conversion electrons and escaping α particles though the use of an array of 28 silicon PIN diodes which are mounted in a box arrangement around the DSSDs. With an active area of 120 mm x 60 mm x 15 mm, a planar Ge detector is mounted at the back of the DSSDs in order to detect x rays and low-energy γ rays. High-energy γ rays can be detected at the focal plane by the clover Ge detector mounted above the vacuum chamber housing the DSSDs and PIN diodes.

3.3.4 Data Acquisition

To avoid the dead time associated with conventional data acquisition systems, the triggerless Total Data Readout (TDR) system [LAB$^+$01] has been employed. Data from all detectors is read simultaneously and stamped with a global 100 MHz clock with a 10 ns accuracy. The front-end electronics of the TDR system are commercial NIM/CAMAC units. Data is fed to the analogue-to-digital converter (ADC) cards via shaping amplifiers and constant fraction discriminators (CFDs). The ADC cards timestamp the data to within a 10 ns precision. A metronome unit ensures all ADCs are synchronised. Events are then time ordered and sent to the event builder, which uses the spatial and temporal information to reconstruct events. The data is then formatted by the event builder for use in the online sorting device GRAIN [Rah07].

3.3.5 Köln Plunger Device

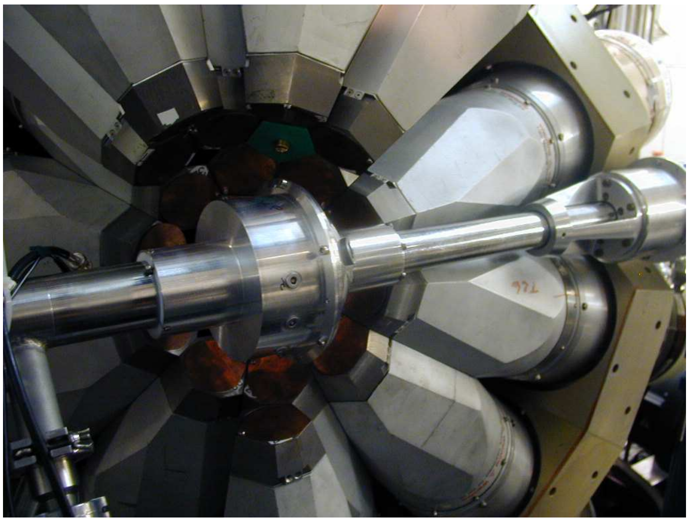

Figure 3.11: The Köln plunger device installed at the target position of JUROGAM.

The Köln plunger is a device used to perform RDDS lifetime measurements. In the experiment discussed in Chapter 4 the plunger device was located at the target position of JUROGAM. The position of the plunger can be seen in Figure 3.11. At the heart of the plunger device is a chamber housing the target and degrader foils (see Figure 3.12). Target and degrader foils are stretched and mounted on conical support rings. These in turn are mounted to frames that are attached to movable rods. The distance between target and degrader foil can be be set by changing the position of the target foil. While the degrader foil position is fixed, the position of the target foil can be changed using a commercial piezoelectric device (Inchworm). Distances less than 200 μm are measured by a magnetic transducer. Distances greater than 200 μm are measured using an optical system attached to the Inchworm. A separate control system records the distance for each experimental run. For short distances an automatic regulation system is used based on the capacitance between target and degrader foils.

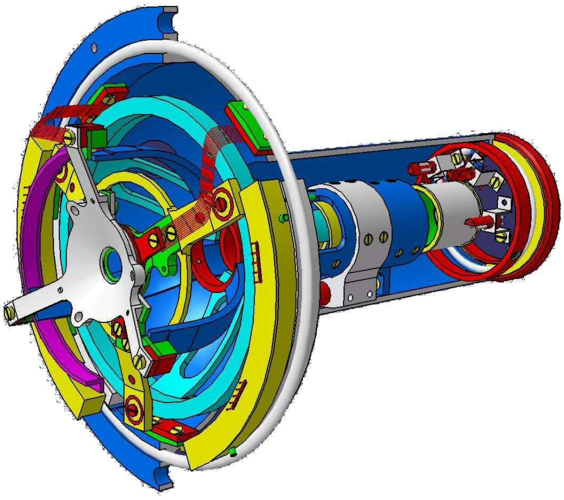

Figure 3.12: Technical representation of the Köln plunger device focusing on the target and degrader set up.

3.4 CERN ISOLDE Facility

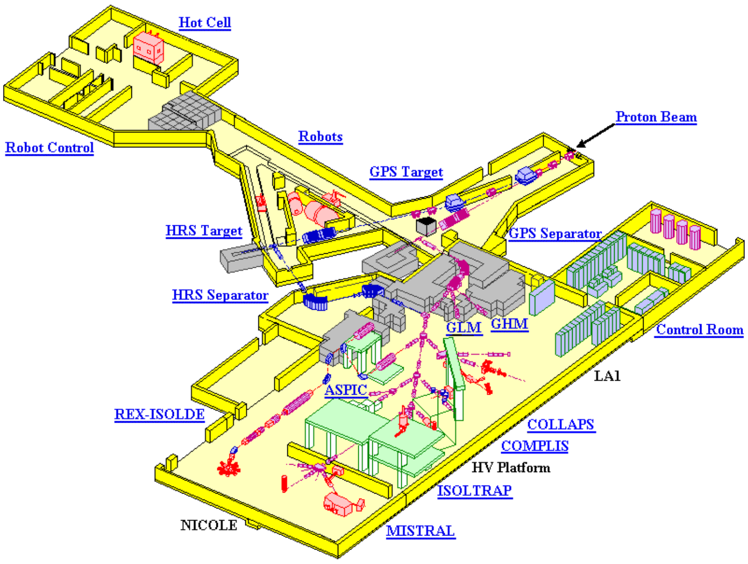

Figure 3.13: Schematic layout of the ISOLDE hall at CERN. The REX linac and MINIBALL spectrometer are located in the south-west corner of the diagram.

The experiments described in Chapter 5 were performed at the ISOLDE facility, CERN. A schematic representation of the ISOLDE hall is given in Figure 3.13. Radioactive isotopes are produced at ISOLDE through spallation, fragmentation or fission reactions. Protons with energies of 1.0 - 1.4 GeV bombard the primary target to produce numerous radioactive isotopes. The protons are provided by the CERN PS Booster (PSB), which consists of four synchrotrons that can provide a maximum proton beam intensity of $3.2\text{x}10^{13}$ p/pulse. Singly charged ions are then extracted from the target-ion source and then accelerated to 60 keV and guided to either of ISOLDE's two isotope separators: the General Purpose Separator (GPS) and the High Resolution Separator (HRS). The GPS has a mass resolving power of $\frac{m}{\Delta m} \approx 2400$ whilst the HRS has a mass resolving power of $\frac{m}{\Delta m} \approx 5000$.

3.4.1 REX-ISOLDE Post Accelerator

The **R**adioactive beam **EX**periment (REX) [HKS+98, KSE+03, CAB+04] at ISOLDE is used for the post acceleration of radioactive isotopes. Beams of singly-charged atoms are delivered to the Penning trap, REX-TRAP where they are cooled and bunched. The bunches are then sent to REX-EBIS, an electron beam ion source, where they are converted to highly charged ions. The highly charged ions that satisfy the specified mass-to-charge ratio, A/q, are extracted as ion bunches, mass separated and injected into the linear accelerator REX-LINAC where they accelerated to an energy around 3.0 MeV/u.

Charge Breeding

Figure 3.14: REX-TRAP (left) and REX-EBIS (right) in the ISOLDE hall CERN.

The charge breeding system at REX-ISOLDE comprises of REX-TRAP [SAB$^+$02], REX-EBIS [Wen02, WCF$^+$03] and an achromatic A/q separator [RKS$^+$99], which guides the mass-separated beam towards the REX-LINAC. 60 keV 1^+ ions delivered by ISOLDE enter the gas filled REX-TRAP and are retarded due to collisions with the dipole-polarised buffer gas. This allows for the continuous injection of ions in the trap. The cylindrical structure of REX-TRAP is located on a 60 keV high voltage platform with a magnetic field of 3 Tesla provided by a superconducting solenoid bore. Such a strong magnetic field provides radial confinement of ions within REX-TRAP, whilst a quadrupole electric potential provides longitudinal confinement of the ions. Further selectivity of the species of interest is provided through sideband cooling [ABD$^+$05], which couples the magnetron and reduced cyclotron motions of the ions. After a typical accumulation and cooling time of 20 ms the ions are extracted from the trap in short bunches and re-accelerated to 60 keV and injected into REX-EBIS for charge breeding. Transmission through REX-TRAP is dependent upon the number of ions accumulated. For an intensity of less than 10^5 ions per bunch an efficiency of up to 45% can be reached. Efficiency decreases with increasing number of ions and can be as low as 10% for intensities of 10^7 ions per bunch.

REX-EBIS produces highly charged ions by bombarding ions sent from REX-TRAP with mono-energetic 5 keV electrons. Current densities of around 150 A/cm are obtained by compressing a 0.2 A electron beam using a 2 T magnetic field created by a superconducting solenoid. For a certain operational frequency, the breeding time can be varied. Varying the breeding time changes the charge state distribution of the produced ions, allowing for certain A/q values to be optimised. It is therefore possible to tune REX-EBIS to the optimal charge state of the ions required for post-acceleration by the REX-LINAC. The beam extracted from REX-EBIS has a typical bunch width of $\sim$100 μs. As only one charge state from the total charge state distribution is chosen by the A/q selector, the maximum breeding efficiency of REX-EBIS is about 30%. As the number of positively charged ions that can be stored in REX-EBIS is around 2x10^{10} per breeding cycle, REX-EBIS does not limit the intensity of the post-accelerator. The number of desired nuclei produced is often several orders of magnitude smaller that the residual stable gas ions bred in REX-EBIS. Mass separation of the beam extracted from REX-EBIS is performed by a S-shaped separator with a mass resolution of $\frac{A/q}{\Delta A/q} \approx 100$ -150. The separator has a transmission efficiency of about 75-90%. The chosen, highly charged radioactive ions are then sent to the REX-LINAC for post-acceleration.

REX Linac

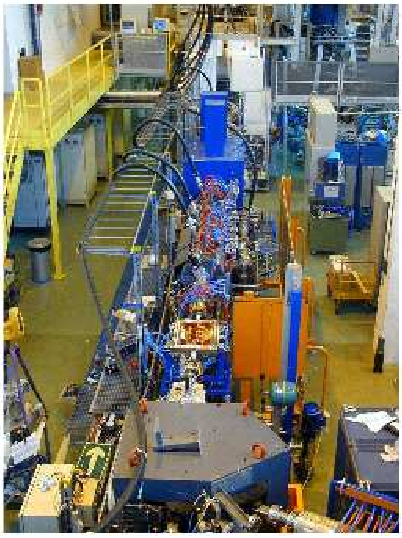

Figure 3.15: REX-LINAC in situe at the ISOLDE hall CERN.

The REX-LINAC, shown in situ in Figure 3.15 and schematically in Figure 3.16, consists of four resonant structures, each adjustable of a certain energy range. The first stage of acceleration occurs when 5 keV ions from REX-EBIS are accelerated to an intermediate energy of 300 keV/u by the RFQ structure. The IH structure then further accelerates the ions to an adjustable energy of 1.1 - 1.2 MeV/u. The final acceleration stages consist of three 7-gap resonators delivering energies in the range of 0.8 - 2.25 MeV/u, and a 9-gap resonator delivering the final, maximum energy of 3.0 MeV/u. The resonance frequency of the 7-gap resonators is 101.28 MHz, whist the 9-gap resonator has a frequency of 202.56 MHz. The ratio of the time over which the LINAC is on over the total time between EBIS pulses is known as the *duty cycle* and is 10%.

The total transmission through REX-LINAC is in the order of 80%. When considering the efficiencies of REX-TRAP, REX-EBIS and the A/q separator, the overall efficiency of REX-ISOLDE is $\approx$5%. The overall efficiency is defined as the ratio of the number of ions reaching the target to the number of ions delivered by ISOLDE to the front of REX-TRAP.

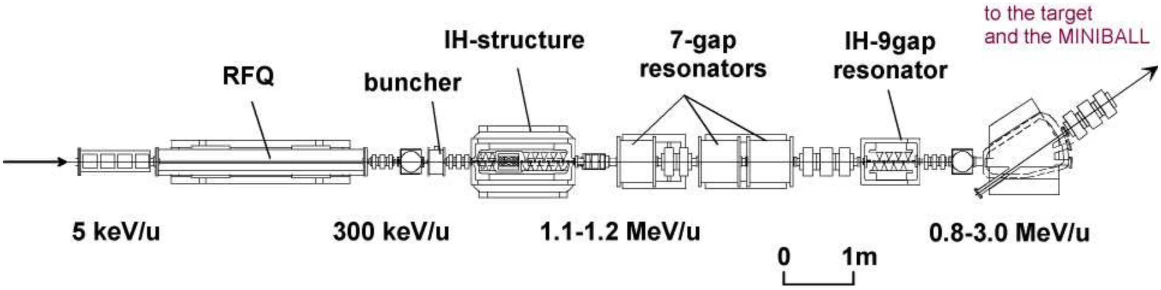

Figure 3.16: Schematic layout of the REX-LINAC [Rex]. The figure shows the accelerating units of REX-LINAC, a bending magnet which guides the ions to one of the two beam lines and the 65° beam line leading to the target position of MINIBALL.

3.4.2 MINIBALL HPGe Array

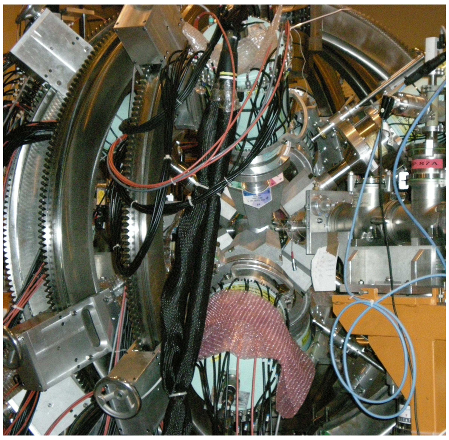

Figure 3.17: The MINIBALL array in situe at REX-ISOLDE.

The MINIBALL detector array consists of 24 individually encapsulated HPGe detectors, each with 6-fold electronic segmentation. The detectors are encapsulated with a 0.7 mm aluminium casing and are arranged into 8 triple-cluster units. The arrangement of the detectors in triple clusters allows for the implementation of an addback procedure, where the individual energies in the three detectors can be summed in the event of a γ ray depositing its energy in neighbouring crystals. The individual cores provide a granularity of 24, whilst the electronic segmentation brings the granularity to 144. Typical depletion voltages for MINIBALL HPGe crystals are 2.5-4.5 kV. Each triple-cluster is kept at LN_2 temperature through the use of a cold finger and an attached dewer containing LN_2. The 8 triple cluster units are mounted to the supporting structure which consists of 6 semi-circular arms, each with three adjustable mounting points as shown in Figure 3.17. The movable supporting arms provide the ability to position the triple cluster units in numerous ways and to obtain the optimum configuration for maximum solid angle coverage. The clusters can also rotate on their own axis and the target-to-detector distance can be modified, for further configuration options. Due to the MINIBALL target chamber having a radius of 8.5 cm, the minimum target-to-detector distance is approximately 9 cm. At such a distance the maximum solid angle coverage is approximately 60% of 4π. The average γ-ray resolution of the MINIBALL detector cores is 2.3 keV at 1.3 MeV. For the MINIBALL segments the resolution decreases slightly to 2.8 keV at 1.3 MeV.

3.4.3 CD Detector

Figure 3.18: The CD particle detector inside the MINIBALL target chamber.

In Coulomb excitation experiments particle detection techniques must be employed in order to identify target and projectile kinematics branches. Located inside the MINIBALL target chamber and mounted 30.5 mm behind the movable target wheel, a double-sided silicon strip detector is located. The segmented Si detector [OCD$^+$02] consists of 4 independent and identical quadrants and is known as the CD detector. Each quadrant has 16 annular strips on the front side. Each strip is 1.9 mm wide with a pitch of 2.0 mm. The back side of the detector has 24 sector strips with a 3.4° pitch resulting in a total of 160 discrete detector elements. The polar and azimuthal coordinates of impinging beam and target nuclei can therefore be easily identified. With a target to detector distance of 30.5 mm the resulting polar angle coverage of the CD detector in the laboratory frame is 16.2° to 53.3°. The polar and azimuthal resolution is approximately 2°. The CD detector has an outer radius of 42.5 mm and an inner radius of 7.5 mm. An azimuthal range of 82° is covered by each quadrant resulting in a total active area of 91%.

3.4.4 Data Acquisition

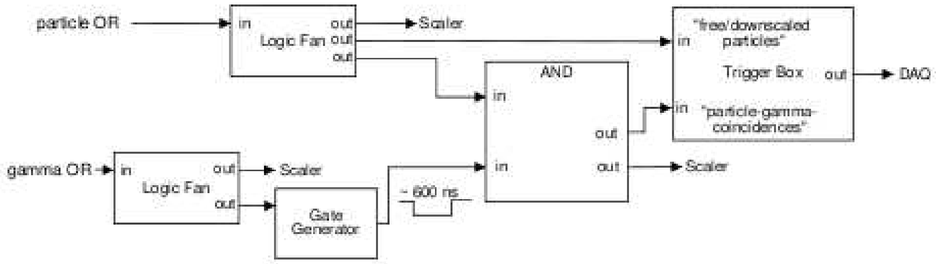

Figure 3.19: Electronics layout of the DAQ trigger generation.

The electronics setup and data acquisition system of MINIBALL is optimised to record information necessary to perform γ-particle coincidences. Detectors in the MINIBALL array are read out using digital XIA DGF4-C modules. The CD detector is read out using CAEN V785 modules. A readout of all channels in one quadrant is fed into a DGF running on the same 40 MHz clock as that of the MINIBALL DGFs. With each individual quadrant treated this way, the CD detector can be regarded as four independent particle detectors. This allows accurate γ-particle-particle coincidences to be determined in the event building process, where a γ ray is required in coincidence with two particles - in opposing CD quadrants. Readout of MINIBALL electronics is aligned to the pulse signal of REX-EBIS. At the start of an EBIS pulse the ‘on beam’ window is opened. The size of the window is typically 800 μs. After this time window closes a readout occurs. The ‘off beam’ window is opened for 8 ms after the start of the EBIS pulse. An event in this window will force a second readout. Triggers arriving within 10 ms of the next EBIS pulse are rejected to ensure a clean ‘on beam’ window. If a readout is initiated the data stored onboard the buffers of the XIA and CAEN modules are read out. For the CAEN V785 modules, the maximum number of events that can be stored in the buffer is limited by hardware to 32. The maximum number of events for the XIA DGF4-C modules can be set by software. The basic layout of DAQ triggers is shown in Figure 3.19. A logical OR of all channels of the MINIBALL array that detect a γ-ray event. This signal is used to create a hardware coincidence window. If a particle OR arrives within this time window a particle-γ coincidence event will be written, generating the particle-γ coincidence trigger. If a particle OR arrives outside of this window but within the 4μs event-building time window, then these free particles are downscaled. The particle setup of Figure 3.19 exists for all four quadrants of the CD with the same common γ gate resulting in a total of 8 DAQ triggers.

Chapter 4

Lifetime Measurements of ^{182}Hg - Analysis and Results

4.1 Experimental Details

Lifetime measurements of excited states in ^{182}Hg were performed at the University of Jyväskylä accelerator laboratory in September 2006 using the Recoil Distance Doppler Shift (RDDS) method. Excited states of ^{182}Hg were populated in the fusion-evaporation reaction ^{96}Mo(^{88}Sr,2n)^{182}Hg at an energy of 310 MeV with target thickness of 0.8 mgcm^{-2}. The reaction at this energy provided an initial recoil velocity of $v/c = 4.4\%$. Typical beam currents were in the region of 2 pnA, limited by the heating of the stretched target and the counting rate of the JUROGAM array. The standard target chamber of JUROGAM was replaced by the Köln plunger device in order to perform RDDS lifetime measurements. The low production cross section of ^{182}Hg required that the selectivity of prompt γ rays was high. The standard stopper foil was therefore replaced by a 1 mgcm^{-2} Mg degrader foil. The fusion-evaporation residuals could therefore enter RITU and be separated from the scattered beam according to their magnetic rigidity. At the focal plane of RITU recoils were implanted into the GREAT spectrometer. MWPCs were used to record energy loss and timing signals and two DSSD detectors recorded the arrival time of the recoil and its subsequent decays.

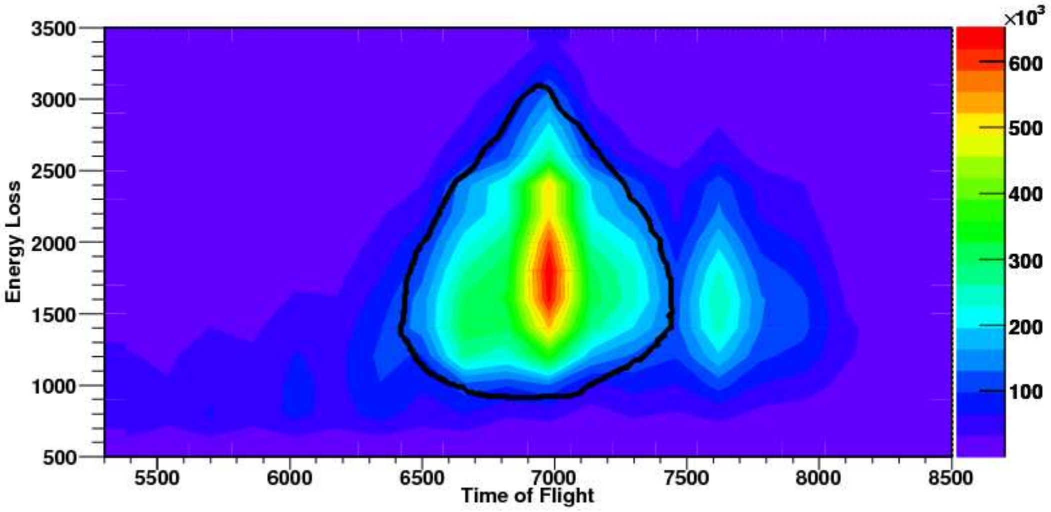

Figure 4.1: Time of flight vs energy loss in the MWPC. Residual fusion evaporation products are on the left and circled with the gate used in the sort code. Scattered beam particles are to the right of the residual fusion evaporation products.

4.2 Recoil Distance Doppler Shift Measurements of ^{182}Hg

The timing and energy loss signals of the MWPC were combined with the timing information of the DSSDs in order to perform recoil gating. Thus prompt γ rays recorded at the target position of the JUROGAM array were associated with the recoils detected at the GREAT focal plane detector. All spectra produced in this chapter used a recoil gate condition. The DSSDs have been used in conjunction with the MWPC to produce a two-dimensional histogram of the time of flight of recoils versus the energy loss recorded in the MWPC. For ^{182}Hg this is shown in Figure 4.1. Coincident recoil-gated γ rays recorded with JUROGAM detectors in Ring 1 and Ring 2 (see Table 3.3) and the whole JUROGAM array were sorted into two separate matrices for each target-to-degrader distance used. Fifteen Target-to-degrader distances ranging from $15\,\mu$m to $3000\,\mu$m were used for the purpose of creating spectra showing the evolution from shifted to degraded for each yrast transition. To illustrate the quality of spectra obtained, Figure 4.2 shows the total projected recoil-gated spectrum obtained from a $\gamma\gamma$-coincidence

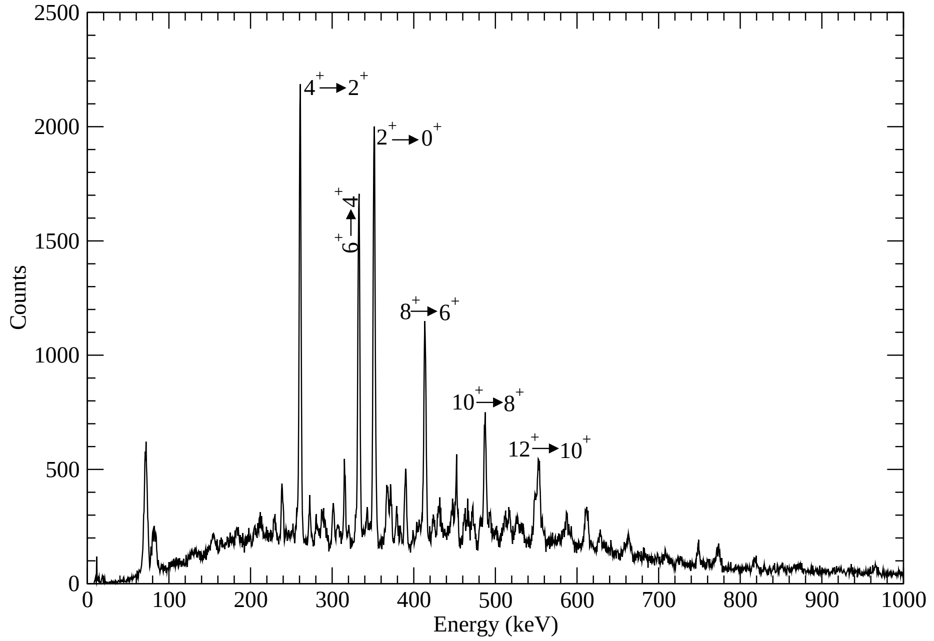

Figure 4.2: The total projection from a recoil gated $\gamma\gamma$ coincidence matrix for the target-to-degrader distance 3000 μm. Yrast transitions in ^{182}Hg used in the DDCM analysis are labeled.

matrix using Ring 1 of JUROGAM and the whole JUROGAM array.

Spectra were produced for lifetime analysis from the $\gamma\gamma$-coincidence matrices by gating on the transition directly feeding the level of interest for each target-to-degrader distance and projecting onto the axis of the Ring 1 or Ring 2 JUROGAM detectors. An example of a gated spectrum obtained from a recoil gated $\gamma\gamma$ coincidence matrix is given in Figure 4.3. When gating directly above the level of interest, uncertainties originating from the time behaviour of unobserved side feeding are eliminated. It is usual in DDCM analysis to only gate on the fully Doppler shifted component of the feeding transition. Due the shifted and degraded components being close in energy, it was necessary in this case to gate on the entire feeding transition. This method has been shown to be consistent with the standard method [DPS$^+$03].

It can be seen in Figure 4.2 and Figure 4.3 that the lifetimes of excited yrast states in ^{182}Hg that are obtainable from this data set are for the 2^+,4^+,6^+,8^+ and

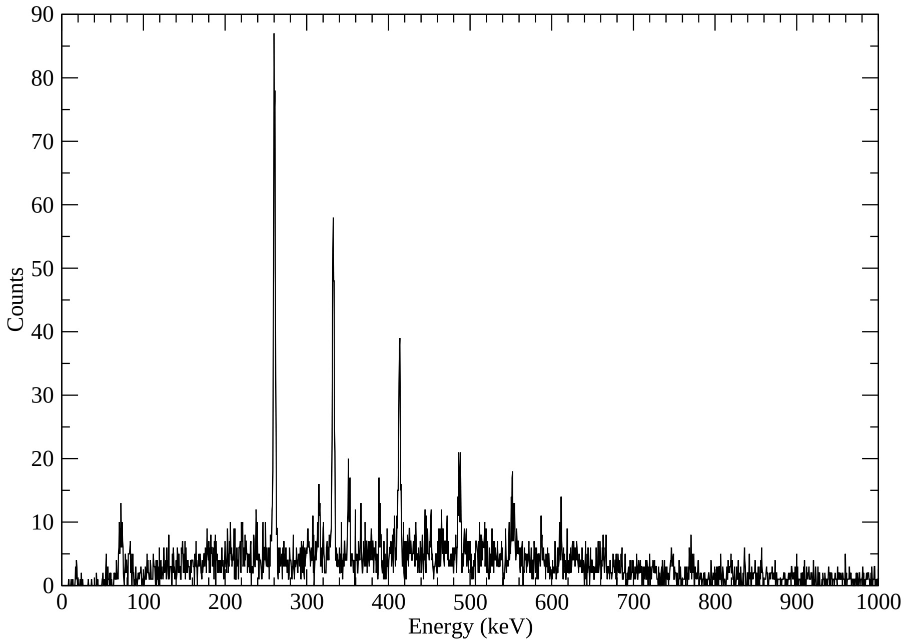

Figure 4.3: Projection of prompt γ rays in coincidence with the 351 keV $2^+ \rightarrow 0^+$ transition. The projection is obtained from a matrix of Ring 1 of JUROGAM and the whole of JUROGAM at a target to degrader distance of 3000 μm.

10^+ states. Yrast transitions higher than the $12^+ \rightarrow 10^+$ were weakly populated and lacked sufficient statistics for lifetime analysis. Lifetimes of states higher in the yrast band than 10^+ were unobtainable, as there was found to be no degraded component to the transition even at the shortest target-to-degrader distance. This suggests that the lifetimes of these high spin states are below the sensitivity of RDDS measurements and are sub-picosecond. When gating on the populating transition to the level of interest for each of the 15 target-to-degrader distances, the evolution of the depopulating transition from fully Doppler shifted to degraded can be observed and the intensities of the shifted I_s and degraded I_d components obtained. For the depopulating transition of the 2^+ yrast state the evolution of the shifted and degraded components can be seen in Figure 4.4 and Figure 4.5. These Figures show the deconvoluted spectra for all 15 target-to-degrader distances, for each individual gate, for both Ring 1 and Ring 2 of JUROGAM. Table 4.1 and Table 4.2 list the shifted and degraded counts, I_s

and I_d for the $2^+ \rightarrow 0^+$ transition at each target-to-degrader distance separately for each JUROGAM ring used. Counts were obtained by fitting the shifted and degraded components of the transition of interest using the IKP Köln package TV. Energies of fitted peaks were normalised to the fully shifted $2^+ \rightarrow 0^+$ transition. Appendix A Contains similar figures and tables corresponding to the deopulating transitions of the 4^+, 6^+, 8^+ and 10^+ yrast states.

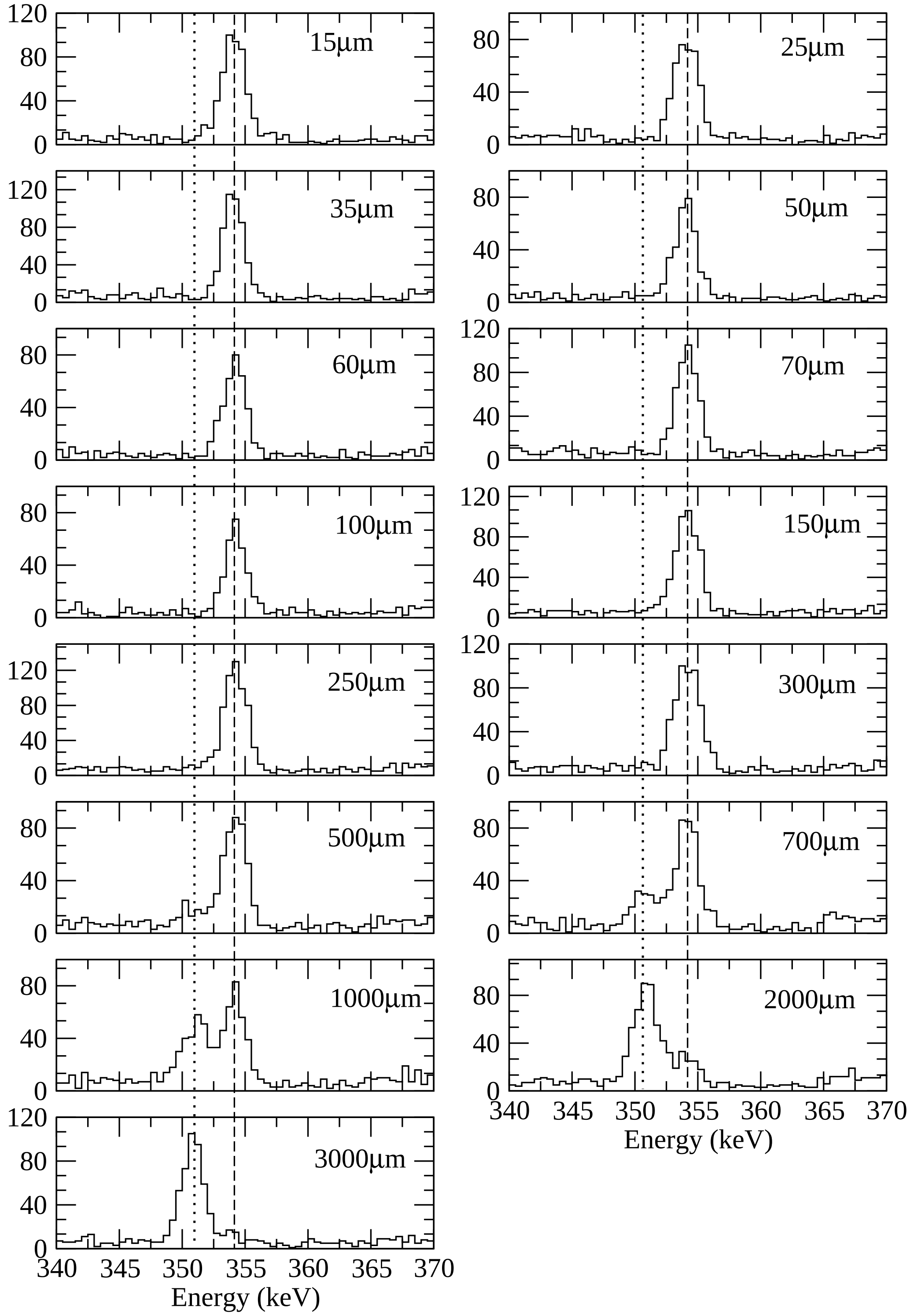

Figure 4.4: Spectra showing the deconvolution of the fully Doppler shifted and degraded components of the 351 keV $2^+ \rightarrow 0^+$ transition, gated on the populating 261 keV $4^+ \rightarrow 2^+$ transition when using Ring 1 of JUROGAM. Target-to-degrader distances are listed in each panel, dashed lines indicate the degraded component whilst dotted lines indicate the fully Doppler shifted component of the transition.

351 keV $2^+ \rightarrow 0^+$ Transition JUROGAM Ring 1		
Distance d (μm)	Counts I_s	Counts I_d
15	1±5	453±22
25	1±5	368±20
35	1±5	462±23
50	2±4	308±18
60	1±4	319±19
70	2±6	430±22
100	1±4	275±18
150	13±7	472±23
250	13±8	536±25
300	13±7	488±23
500	56±10	388±21
700	129±13	373±21
1000	215±16	309±19
2000	389±21	99±13
3000	420±22	24±8

Table 4.1: Summary of measurements of different target-to-degrader distances for the 351 keV $2^+ \rightarrow 0^+$ transition for RDDS measurements of ^{182}Hg. The fully Doppler shifted components, I_s and degraded components, I_d are measured with 5 JUROGAM detectors at 157.6°.

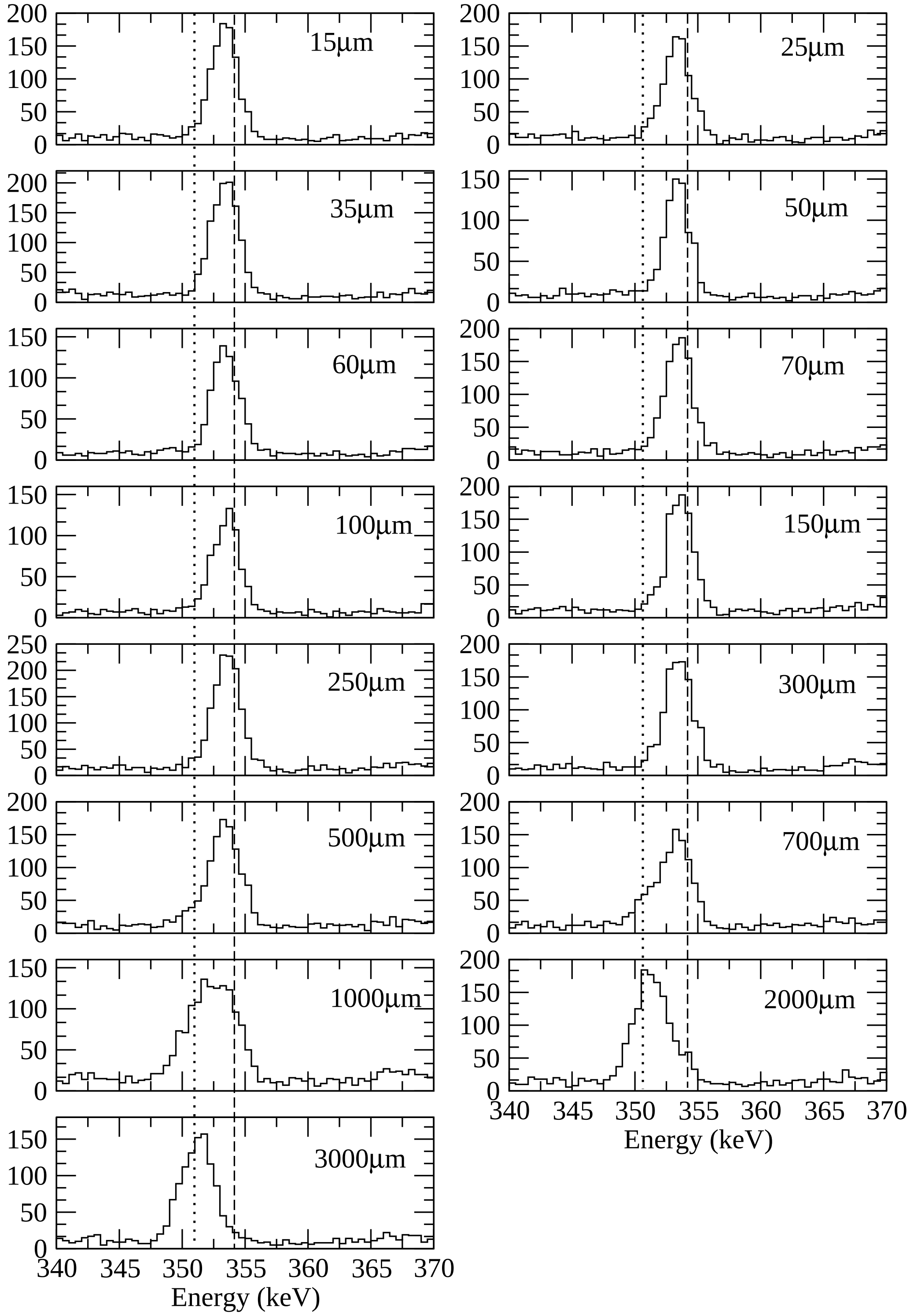

Figure 4.5: Spectra showing the deconvolution of the fully Doppler shifted and degraded components of the 351 keV $2^+ \rightarrow 0^+$ transition, gated on the populating 261 keV $4^+ \rightarrow 2^+$ transition when using Ring 2 of JUROGAM. Target-to-degrader distances are listed in each panel, dashed lines indicate the degraded component whilst dotted lines indicate the fully Doppler shifted component of the transition.

351 keV $2^+ \rightarrow 0^+$ Transition JUROGAM Ring 2		
Distance d (μm)	Counts I_s	Counts I_d
15	36±17	897±33
25	22±16	786±31
35	21±15	1064±36
50	31±14	681±29
60	19±13	692±29
70	19±14	908±34
100	25±14	618±28
150	15±12	862±33
250 12±9	1160±38	
300 14±9	894±33	
500 129±22	841±34	
700 243±25	678±32	
1000	547±32	546±31
2000	1029±39	150±24
3000	906±35	17±10

Table 4.2: Summary of measurements of different target-to-degrader distances for the 351 keV $2^+ \rightarrow 0^+$ transition for RDDS measurements of ^{182}Hg. The fully Doppler shifted components, I_s and degraded components, I_d are measured with 10 JUROGAM detectors at 134.8°.

4.3 Lifetime Analysis Using the Differential Decay Curve Method

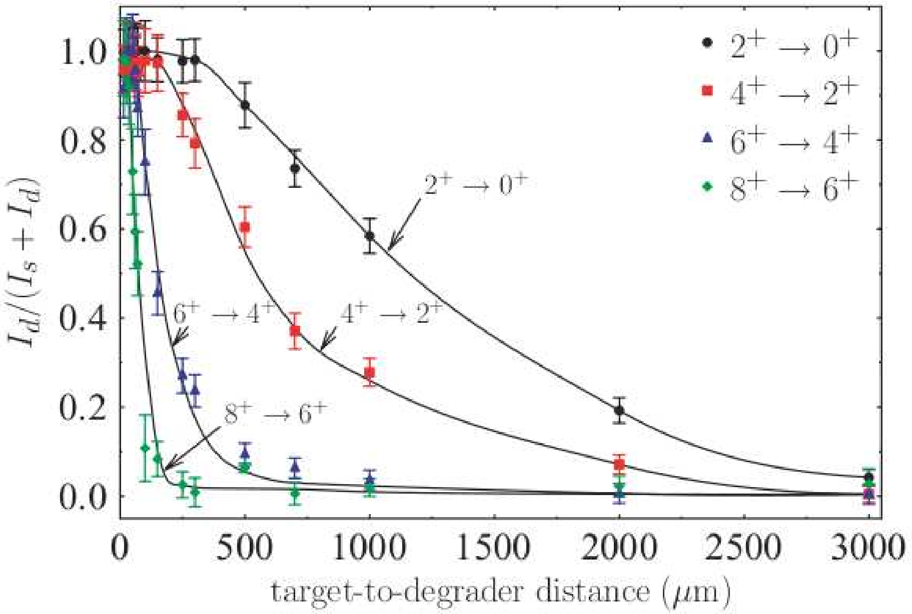

Figure 4.6: Decay curves of the lowest four yrast states in ^{182}Hg extracted from data recorded with Ring 1 of JUROGAM. Smooth lines are for the purpose of guiding the eye only.

Decay curves measured with JUROGAM detectors at 158° and 134° were analysed separately by means of the Differential Decay Curve Method (DDCM), details of which are given in § 2.2.2. Distance normalisation was performed by normalising the area of the degraded component (or fully Doppler-shifted component) of the transition of interest to the sum of the areas of the fully Doppler shifted and degraded components, as described in Equation 2.68. Sample decay curves, constructed from data using the 158° JUROGAM detectors, are given in Figure 4.6. Decay curves for both degraded and fully Doppler-shifted components were analysed separately, resulting in multiple lifetimes for each level investigated. The quoted lifetime is therefore an average of these values. An appropriate fit of the normalised degraded and fully Doppler-shifted components in NAPATAU yielded lifetimes for each investigated state. Figure 4.7 to Figure 4.11 show the fits and resulting lifetime values obtained from the measured decay curves using NAPATAU. It is important to note that only the region of sensitivity, as defined in § 2.2.2, needs be to fitted to obtain values for the lifetimes of the excited states. Values outside of this region have not necessarily been used in the fit, as can be seen in these figures.

Lifetimes for excited states are obtained from Figure 4.7 to Figure 4.11 using the DDCM. Shown in the middle panel of each figure is the decay curve associated to the depopulating transition from the level of interest. The red data points in the bottom panel represent the difference in intensity between the populating and depopulating transitions to the level of interest. This relates directly to the numerator on the right hand side of Equation 2.66. The solid blue line in the bottom panel is the differntial of the decay curve of the populating transition. This is of course relates directly to the denominator of Equation 2.66 and is found by fitting smoothly connected polynomials to the derivative of the decay curve. The lifetime at each point in the region of sensitivity is found by taking the ratio of the derivative of the decay curve to the difference in intensities of the feeding and depopulating transitions. This ratio is a direct measure of the lifetime at each point. The weighted averages of each ratio obtained at points in the region of sensitivity then result in the quoted value of τ.

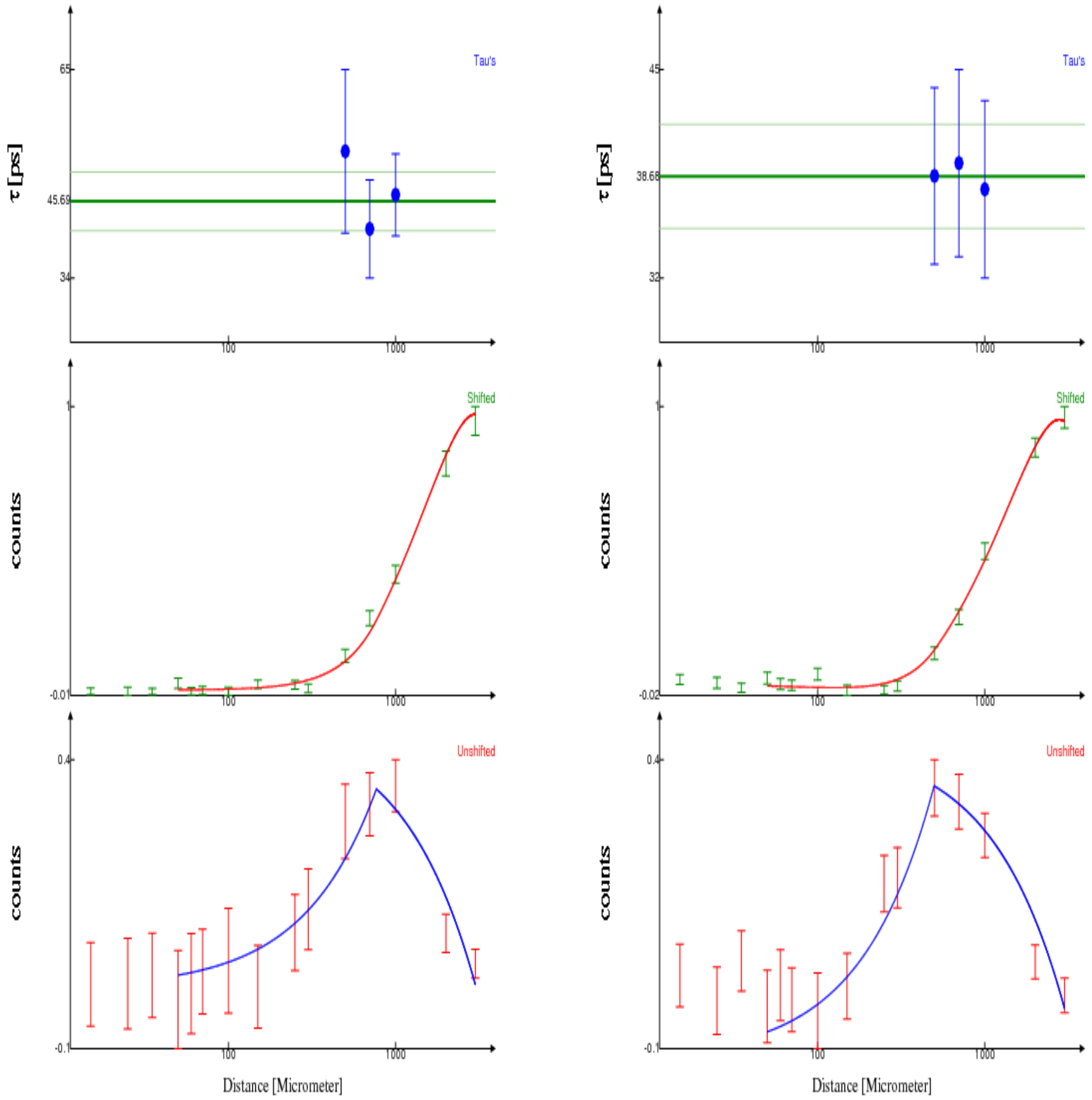

Figure 4.7: Lifetime plots generated from NAPATAU for data obtained with Ring 1 (left) and Ring 2 (right) of JUROGAM. The top panel shows the values of τ obtained for three distances within the region of sensitivity. The mean value of τ is represented a bold green line, whilst the upper and lower values are shown on the diagram as a feint green line. The middle panel shows the normalised fully Doppler-shifted component of the depopulating $2^+ \rightarrow 0^+$ transition, with the decay curve drawn in red. The bottom panel represents the difference between the degraded components of the feeding $4^+ \rightarrow 2^+$ transition and the depopulating $2^+ \rightarrow 0^+$ transition. The solid blue line is the derivative of the decay curve depicted in the middle panel, multiplied by τ.

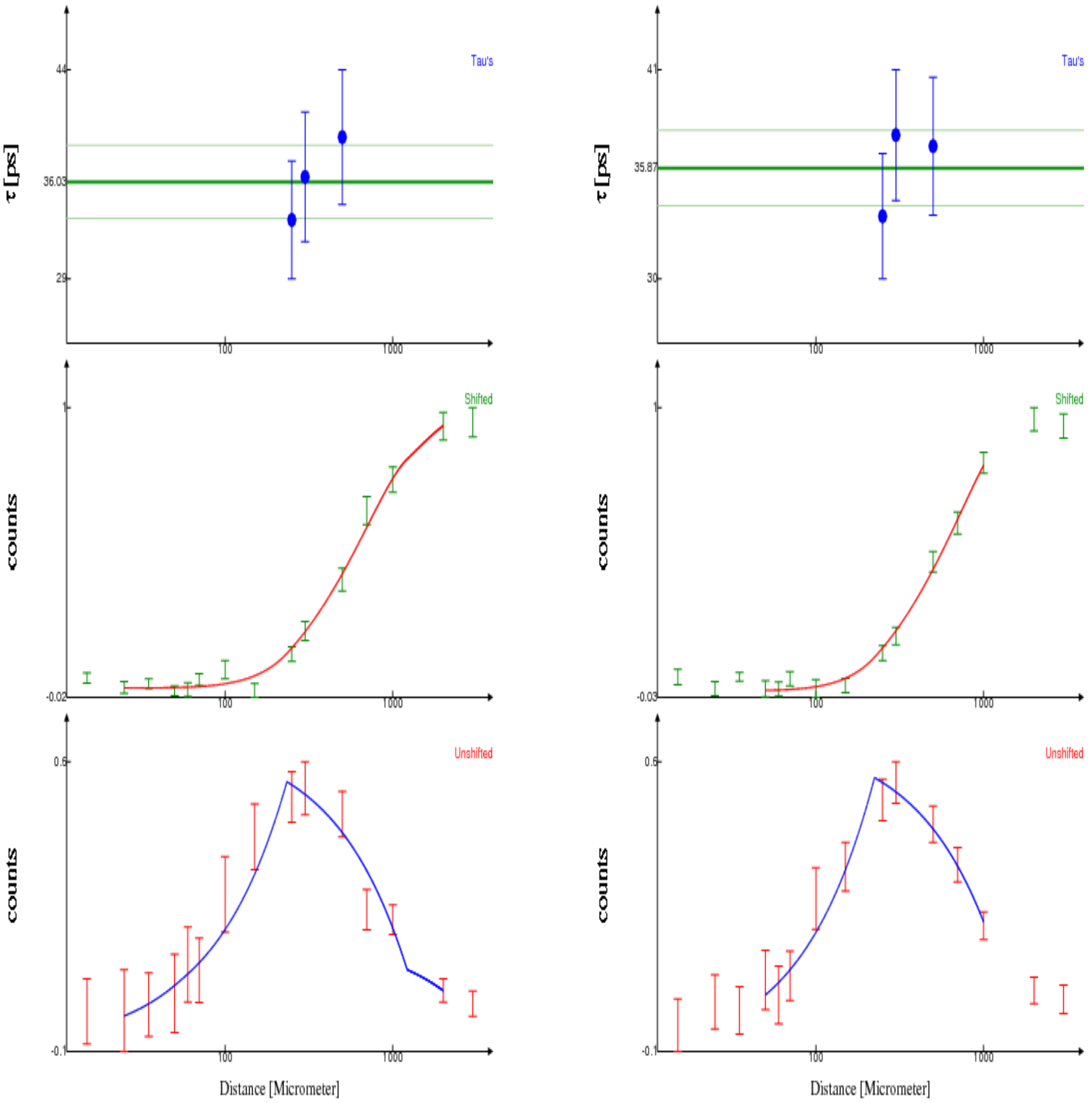

Figure 4.8: Lifetime plots generated from NAPATAU for data obtained with Ring 1 (left) and Ring 2 (right) of JUROGAM. The top panel shows the values of τ obtained for three distances within the region of sensitivity. The mean value of τ is represented a bold green line, whilst the upper and lower values are shown on the diagram as a feint green line. The middle panel shows the normalised fully Doppler-shifted component of the depopulating $4^+ \rightarrow 2^+$ transition, with the decay curve drawn in red. The bottom panel represents the difference between the degraded components of the feeding $6^+ \rightarrow 4^+$ transition and the depopulating $4^+ \rightarrow 2^+$ transition. The solid blue line is the derivative of the decay curve depicted in the middle panel, multiplied by τ.

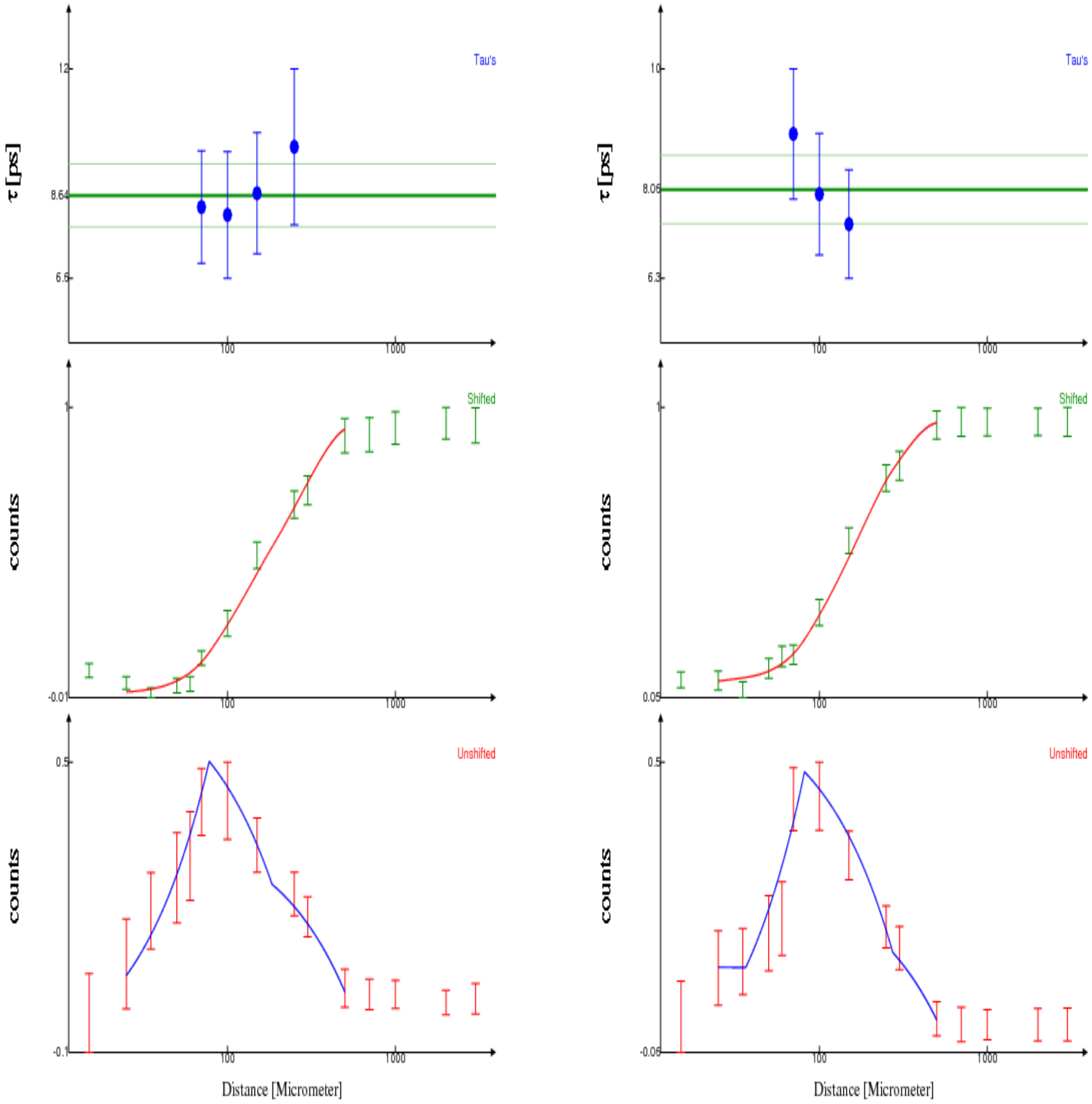

Figure 4.9: Lifetime plots generated from NAPATAU for data obtained with Ring 1 (left) and Ring 2 (right) of JUROGAM. The top panel shows the values of τ obtained for three distances within the region of sensitivity. The mean value of τ is represented a bold green line, whilst the upper and lower values are shown on the diagram as a feint green line. The middle panel shows the normalised fully Doppler-shifted component of the depopulating $6^+ \rightarrow 4^+$ transition, with the decay curve drawn in red. The bottom panel represents the difference between the degraded components of the feeding $8^+ \rightarrow 6^+$ transition and the depopulating $6^+ \rightarrow 4^+$ transition. The solid blue line is the derivative of the decay curve depicted in the middle panel, multiplied by τ.

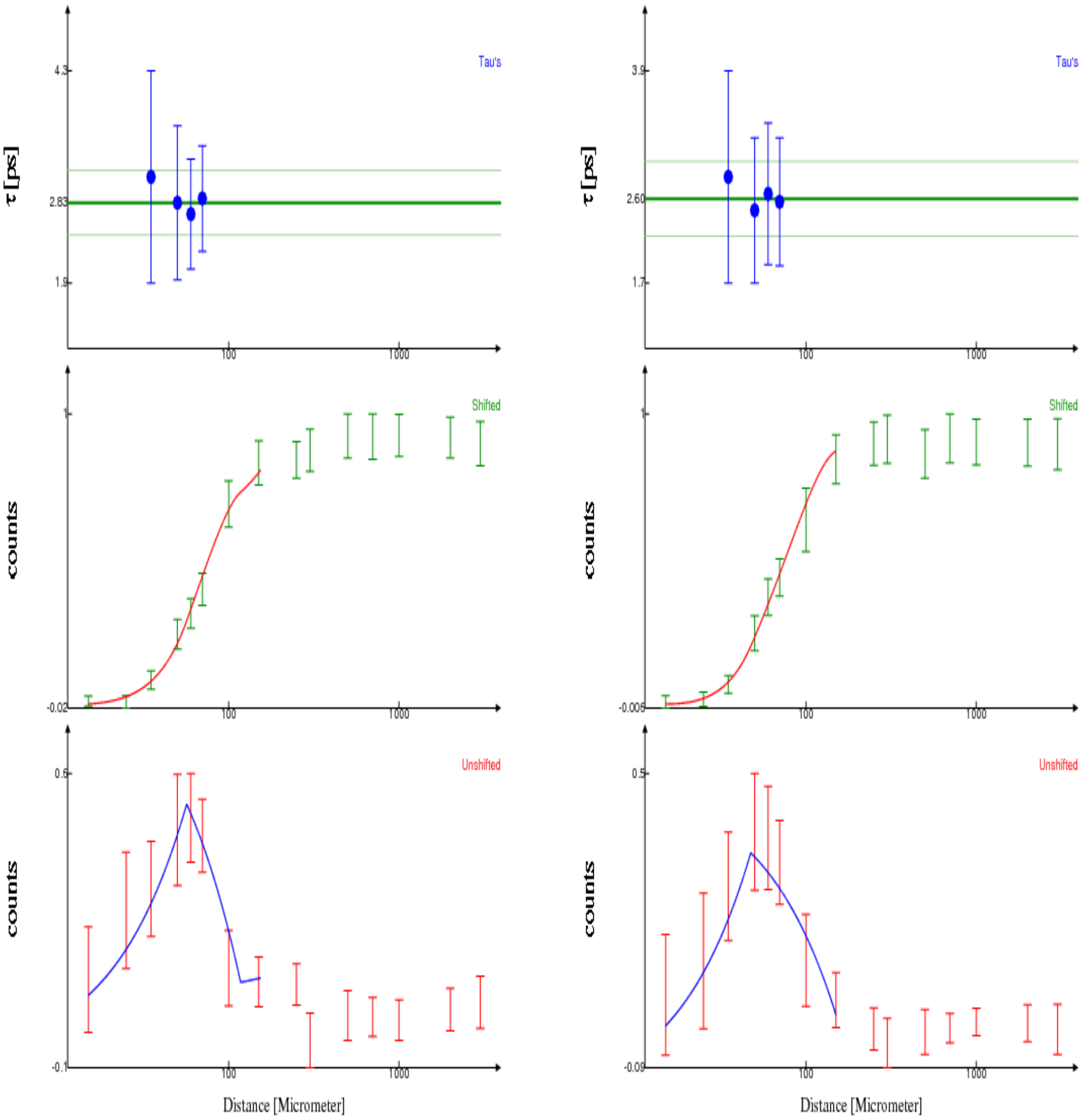

Figure 4.10: Lifetime plots generated from NAPATAU for data obtained with Ring 1 (left) and Ring 2 (right) of JUROGAM. The top panel shows the values of τ obtained for three distances within the region of sensitivity. The mean value of τ is represented a bold green line, whilst the upper and lower values are shown on the diagram as a feint green line. The middle panel shows the normalised fully Doppler-shifted component of the depopulating $8^+ \rightarrow 6^+$ transition, with the decay curve drawn in red. The bottom panel represents the difference between the degraded components of the feeding $10^+ \rightarrow 8^+$ transition and the depopulating $8^+ \rightarrow 6^+$ transition. The solid blue line is the derivative of the decay curve depicted in the middle panel, multiplied by τ.

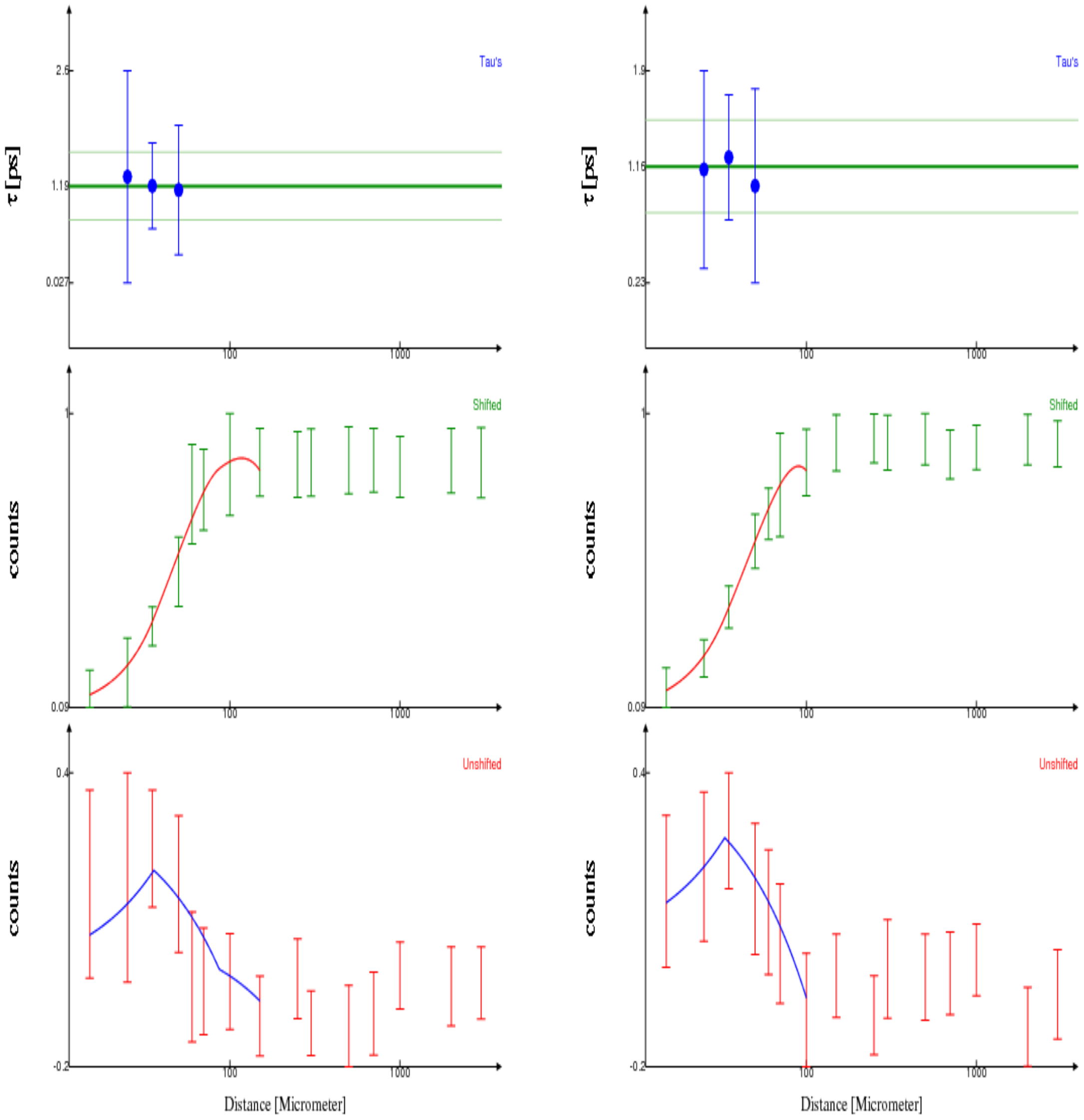

Figure 4.11: Lifetime plots generated from NAPATAU for data obtained with Ring 1 (left) and Ring 2 (right) of JUROGAM. The top panel shows the values of τ obtained for three distances within the region of sensitivity. The mean value of τ is represented a bold green line, whilst the upper and lower values are shown on the diagram as a feint green line. The middle panel shows the normalised fully Doppler-shifted component of the depopulating $10^+ \rightarrow 8^+$ transition, with the decay curve drawn in red. The bottom panel represents the difference between the degraded components of the feeding $12^+ \rightarrow 10^+$ transition and the depopulating $10^+ \rightarrow 8^+$ transition. The solid blue line is the derivative of the decay curve depicted in the middle panel, multiplied by τ.

The final mean lifetime for each measured excited yrast state in ^{182}Hg is listed in Table 4.3. The final values for each excited state are averages of the values obtained from the separate analysis of data obtained with detectors in Ring 1 of JUROGAM and Ring 2 of JUROGAM. By using the rotational model and assuming a rotating quadrupole deformation, the absolute values of the transitional quadrupole moments, Q_t and the deformation parameters $|\beta_2|$ have been extracted from the experimental *B(E2)*↓ values. Along with the mean lifetime for each measured excited state, Table 4.3 lists *B(E2)*↓, Q_t and $|\beta_2|$ values for each measured yrast state in ^{182}Hg.

Average Lifetime Values and Associated Parameters for ^{182}Hg					
E_γ (keV)	I^π	τ (ps)	*B(E2)*↓ (W.u)	$\lvert Q_t \rvert$ (e.b)	$\lvert\beta_2\rvert$
351.8	2^+	41(3)	57(4)	4.17(14)	0.135(5)
261.4	4^+	35.7(15)	264(11)	7.53(16)	0.244(6)
333.1	6^+	8.2(5)	370(30)	8.5(3)	0.274(9)
414.0	8^+	2.9(3)	380(40)	8.4(5)	0.271(13)
487.4	10^+	1.2(3)	400(100)	9(1)	0.28(4)

Table 4.3: Average lifetime values and electromagnetic properties for measured yrast states in ^{182}Hg. γ-ray energies and values of I^π are taken from [BHB$^+$95]. A value of *k=0* is assumed.

Chapter 5

Coulomb Excitation of ^{182,186}Hg - Analysis and Results

5.1 Experimental Details

In the Autumn of 2008 beams of ^{182,184,186,188}Hg were provided by REX-ISOLDE for Coulomb excitation measurements. A 1.4 GeV proton beam was taken by ISOLDE at a repetition rate of 1.2 s cycling with each of the 7/12 pulses of the PSB supercycle, containing, on average, between $1.5\,\mathrm{x}\,10^{13}$ and $2\,\mathrm{x}\,10^{13}$ protons, with a beam current of approximately 1.7 μA. Protons were delivered to the primary UC_2 target producing the above mentioned Hg isotopes. Singly-charged Hg isotopes were then charge bred by REX-EBIS to a charge state of $q = +43$ before being post accelerated by REX-LINAC to energies of 2.85 MeV/u. Table 5.1 lists the isotope intensities measured at the target position of MINIBALL for each Hg isotope accelerated. Inside the MINIBALL target holder was housed 2 mgcm^{-2} cadmium targets. For the Coulomb excitation of ^{182}Hg, a ^{112}Cd target was employed, whereas for the Coulomb excitation of ^{186}Hg a ^{114}Cd target was used. For all cases, Coulomb excitation of the Hg isotopes was performed in inverse kinematics.

Isotope Intensities	
Isotope	Intensity (pps)
^{182}Hg	4.9 x 10^3
^{184}Hg	1.0 x 10^5
^{186}Hg	2.5 x 10^5
^{188}Hg	3.1 x 10^5

Table 5.1: Measured intensity at the target position of MINIBALL of the accelerated Hg isotopes.

5.2 Efficiency Calibration

The Coulomb excitation cross section of the Hg isotopes is measured relative to the Coulomb excitation cross section of the particular Cd target employed. It is therefore imperative that an accurate efficiency calibration be performed for the MINIBALL HPGe detectors. At the start of the experimental run, a combined ^{152}Eu and ^{133}Ba source was placed at the target position of MINIBALL. Such a combination allows for a wide range of energies to be considered, ranging from 80.9 keV - 1408 keV. The relative efficiency curve shown in Figure 5.1 was produced by normalising the ^{133}Ba data to the ^{152}Eu data.

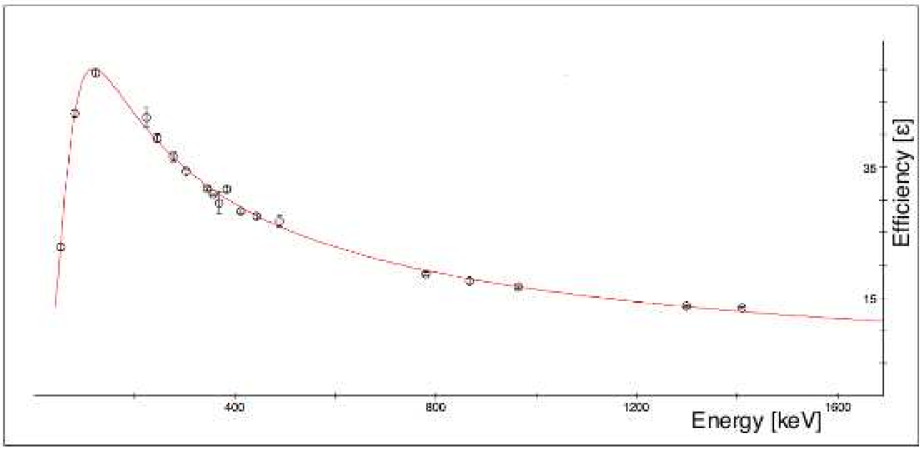

Figure 5.1: Relative efficiency curve for the MINIBALL HPGe array. Data points are obtained from ^{152}Eu and ^{133}Ba sources. The solid red line is a fitted function obtained using RADWARE.

Relative Efficiency Parameters						
A	B	C	D	E	F	G
6.8	5.0	0	4.818	-0.496	-0.081	14.8

Table 5.2: Tabulated relative efficiency parameters obtained using RADWARE. Parameters describe the relative efficiency curve in Figure 5.1 and have been used in GOSIA input file to correct raw yields.

After 100 iterations the fit converged with a χ^2/d.o.f = 2.61. The evaluated parameters of the relative efficiency curve were determined using EFFIT, a RADWARE [Rad95] package. Listed in Table 5.2 are the parameters A - G. A,B and C describe the efficiency curve at low energies such that

$$log(\epsilon_\gamma) = A + B \cdot log\left(\frac{E_\gamma}{100\,keV}\right) + C \cdot log\left(\frac{E_\gamma}{100\,keV}\right)^2 . \tag{5.1}$$

D,E and F describe the efficiency at high energies such that

$$log(\epsilon_\gamma) = D + E \cdot log\left(\frac{E_\gamma}{1\,MeV}\right) + F \cdot log\left(\frac{E_\gamma}{1\,MeV}\right)^2 . \tag{5.2}$$

The parameter G is an interaction parameter between the two regions, and describes specifically the turnover point.

5.3 Event Selection

^{182}Hg Coincidence Window

True γ-particle-particle events were selected by means of inspecting the timing spectra shown in Figure 5.2, observed following the radioactive beam reaction ^{112}Cd(^{182}Hg,^{182}Hg*) at 2.85 MeV/u. It can be seen in Figure 5.2 that true coincidence events lie within a time window of ≈300 ns, ranging from -900 $\leq t \leq$ -600. A time cut corresponding to events within this window was therefore implemented in the sort code. Random coincidences were subtracted from the prompt spectrum by defining a random time cut within the sort code. Figure 5.2 was again used for the definition of this time window. A window of equal size to that

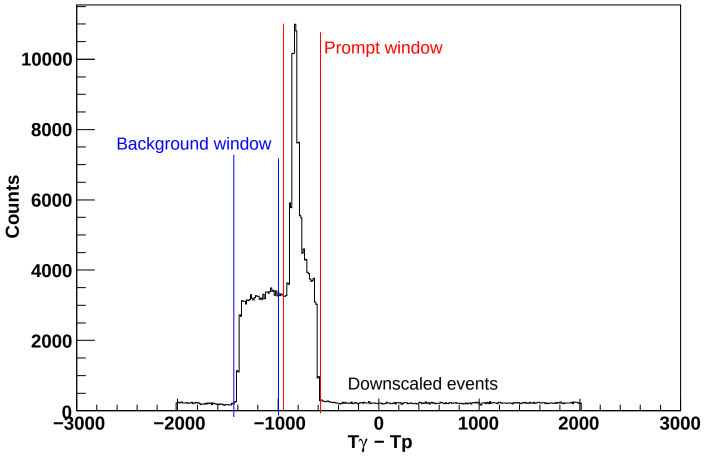

Figure 5.2: Time difference between prompt γ rays and scattered particles in the reaction ^{112}Cd(^{182}Hg,^{182}Hg*). The prompt(random) time window is depicted in red(blue). Events lying outside these windows are labelled as downscaled events.

of the prompt window was created, ranging from $-1200 \leq t \leq -900$. Events within the background window have their origin from γ rays being detected in random coincidence with scattered particles observed in the CD detector, and therefore are not associated with a true Coulomb excitation event. Coincidences occurring outside of the defined background window are defined as *downscaled events*. These originate from γ rays being detected in coincidence with elastic scattered particles in the CD detector that have not undergone Coulomb excitation.

^{182}Hg Particle Identification

As the reaction ^{112}Cd(^{182}Hg,^{182}Hg*) took place under inverse kinematics, the scattered Hg particles are confined to somewhat of a boomerang shape, defined by a maximum scattering angle of approximately 40° in the laboratory frame. To be sure that prompt γ rays are assigned to the correct kinematics branch, a condition was placed in the sort code requiring the detection of the corresponding scattered ^{112}Cd particle to the scattered ^{182}Hg particle in the CD detector. Figure 5.3 shows the theoretical kinematics for this reaction and depicts the angular region that the CD detector covers. It can be seen that when a target and projectile are required in the same event, the angular range that one is sensitive to for the ^{182}Hg

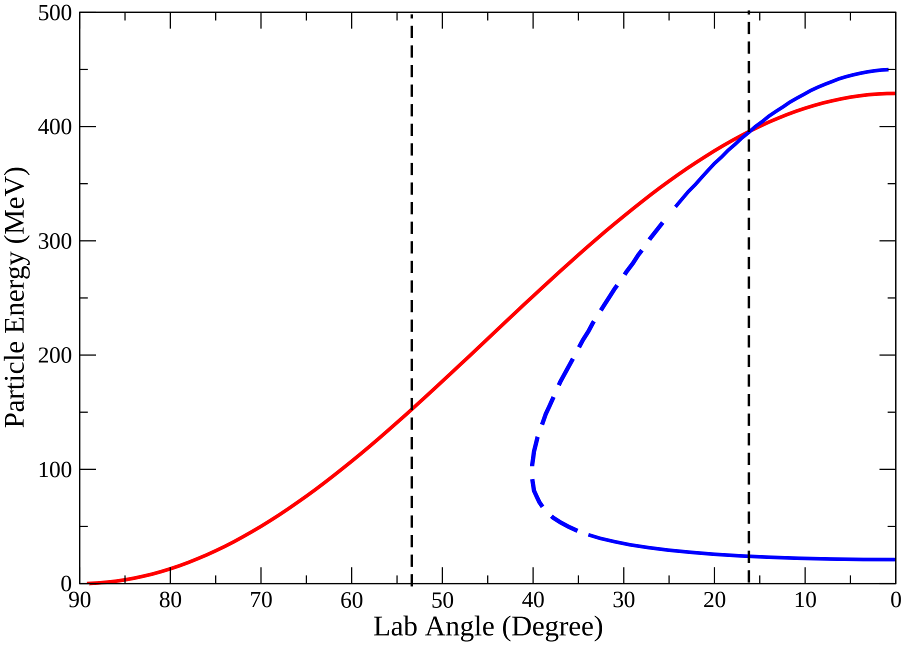

Figure 5.3: ^{112}Cd(^{182}Hg,^{182}Hg*) particle kinematics at an energy of 2.85 MeV/u. ^{112}Cd is represented by the red kinematics branch. ^{182}Hg kinematics branch is in blue. The dashed section of the ^{182}Hg branch represents the region that is observable when a ^{112}Cd particle is required within the same event. Dashed black lines represent the CD particle detector angular limits.

particles decreases. Though this limits the total centre-of-mass angular range that the experiment is sensitive to, the increased accuracy in separating the kinematics branches more than compensates. Figure 5.4 details the observed kinematics for the reaction ^{112}Cd(^{182}Hg,^{182}Hg*) at 2.85 MeV/u when the condition that both target and projectile particles are detected within the same event is implemented.

A projection of each individual CD detector strip allowed particle energy gates for each kinematic branch to be determined. If the kinematics branches could not be separated then the strip was discarded and the data omitted, ensuring that γ rays were cleanly assigned. Three distinct angular cuts were then defined using neighbouring ^{112}Cd particle energy gates. Table 5.3 defines the three angular cuts in terms of centre-of-mass scattering angle, CD detector strip numbers and laboratory angles covered.

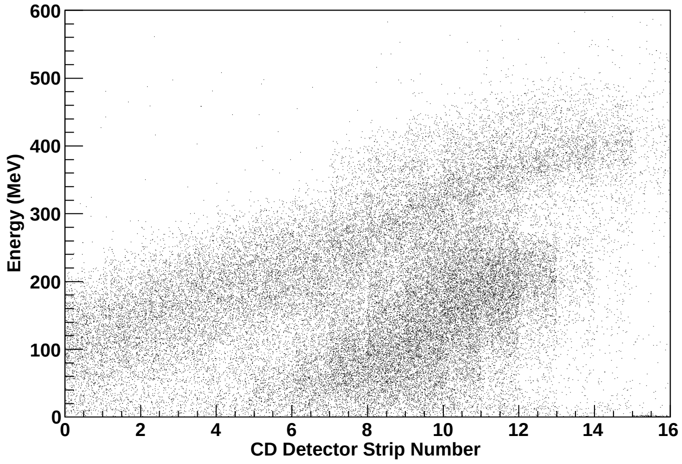

Figure 5.4: ^{112}Cd(^{182}Hg,^{182}Hg*) particle kinematics at an energy of 2.85 MeV/u. The condition that both target and projectile nuclei are detected within the same event is implemented.

Angular Cuts For ^{182}Hg			
	^{112}Cd Strip Range	^{112}Cd Lab Angle	COM Angle
Low COM	1 - 4	45.4° - 53°	74° - 90°
Med COM	5 - 9	32.73° - 42.868°	92.5° - 115°
High COM	12 - 14	20.06° - 25.13°	130° - 140°

Table 5.3: Angular cuts defined in terms of centre-of-mass scattering angle, ^{112}Cd laboratory angle and CD detector strip number. Note that the whole of the angular coverage available from the CD detector could not be used due to kinematics branches being inseparable in some CD detector strips. Cuts are named in terms of the COM angular range they cover eg Low COM angular range, Medium COM angular range and High COM angular range.

^{186}Hg Coincidence Window

True γ-particle-particle events were selected by means of inspecting the timing spectra shown in Figure 5.5, observed following the radioactive beam reaction ^{114}Cd(^{186}Hg,^{186}Hg*) at 2.85 MeV/u. It can be seen in Figure 5.5 that true coincidence events lie within a time window of ≈300 ns, ranging from $-900 \leq t \leq -600$. A time cut corresponding to events within this window was therefore implemented in the sort code. Random coincidences were subtracted from the prompt spectrum by defining a random time cut within the sort code. Figure 5.5 was again used for the definition of this time window. A window of equal size to that of the prompt window was created, ranging from $-1200 \leq t \leq -900$. Events within the background window have their origin from γ rays being detected in random coincidence with scattered particles observed in the CD detector, and therefore are not associated with a true Coulomb excitation event. Coincidences occurring outside of the defined background window are defined as *downscaled events*. These originate from γ rays being detected in coincidence with elastic scattered particles in the CD detector that have not undergone Coulomb excitation.

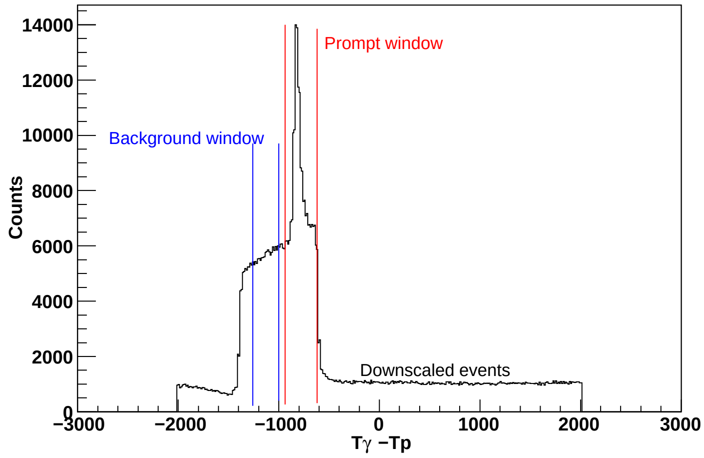

Figure 5.5: Time difference between prompt γ rays and scattered particles in the reaction ^{114}Cd(^{186}Hg,^{186}Hg*). The prompt(random) time window is depicted in red(blue). Events lying outside these windows are labelled as downscaled events.

^{186}Hg Particle Identification

As the reaction ^{114}Cd(^{186}Hg,^{186}Hg*) took place under inverse kinematics, the scattered Hg particles are confined to somewhat of a boomerang shape, defined by a maximum scattering angle of approximately 39.0° in the laboratory frame. To be sure that prompt γ rays are assigned to the correct kinematics branch, a condition was placed in the sort code requiring the detection of the corresponding scattered ^{114}Cd particle to the scattered ^{186}Hg particle in the CD detector. As was the case described in § 5.3, the angular range that one is sensitive to for the ^{186}Hg particles decreases but the ability to separate the kinematics branches increases. Figure 5.6 details the observed kinematics for the reaction ^{114}Cd(^{186}Hg,^{186}Hg*) at 2.85 MeV/u when the condition that both target and projectile particles are detected within the same event is implemented.

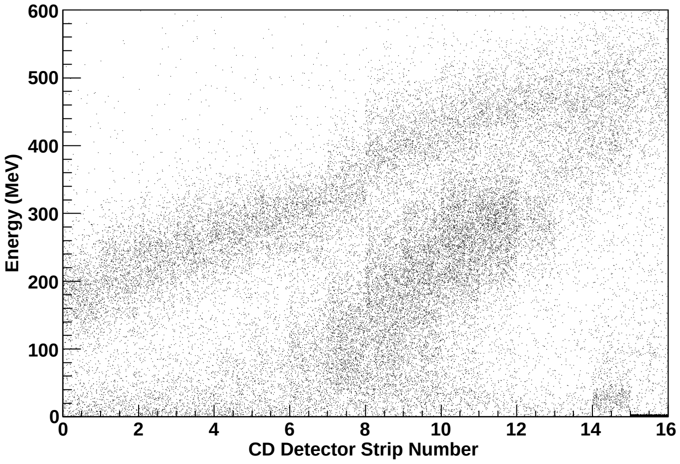

Figure 5.6: ^{114}Cd(^{186}Hg,^{186}Hg*) particle kinematics at an energy of 2.85 MeV/u. The condition that both target and projectile nuclei are detected within the same event is implemented.

Angular Cuts For ^{186}Hg

	^{114}Cd Strip Range	^{112}Cd Lab Angle	COM Angle
Low COM	1 - 4	45.4° - 53.3°	74° - 90°
Med COM	5 - 8	35.26° - 42.86°	96° - 110°
High COM	10 - 13	22.59° - 30.19°	120° - 135°

Table 5.4: Angular cuts defined in terms of centre-of-mass scattering angle, ^{114}Cd laboratory angle and CD detector strip number. Note that the whole of the angular coverage available from the CD detector could not be used due to kinematics branches being inseparable in some CD detector strips. Cuts are named in terms of the COM angular range they cover e.g. Low COM angular range, Medium COM angular range and High COM angular range.

A projection of each individual CD detector strip allowed particle energy gates for each kinematic branch to be determined. If the kinematics branches could not be separated then the strip was discarded and the data omitted, ensuring that γ rays were cleanly assigned. Three distinct angular cuts were then defined using neighbouring ^{114}Cd particle energy gates. Table 5.4 defines the three angular cuts in terms of centre-of-mass scattering angle, CD detector strip numbers and laboratory angles covered.

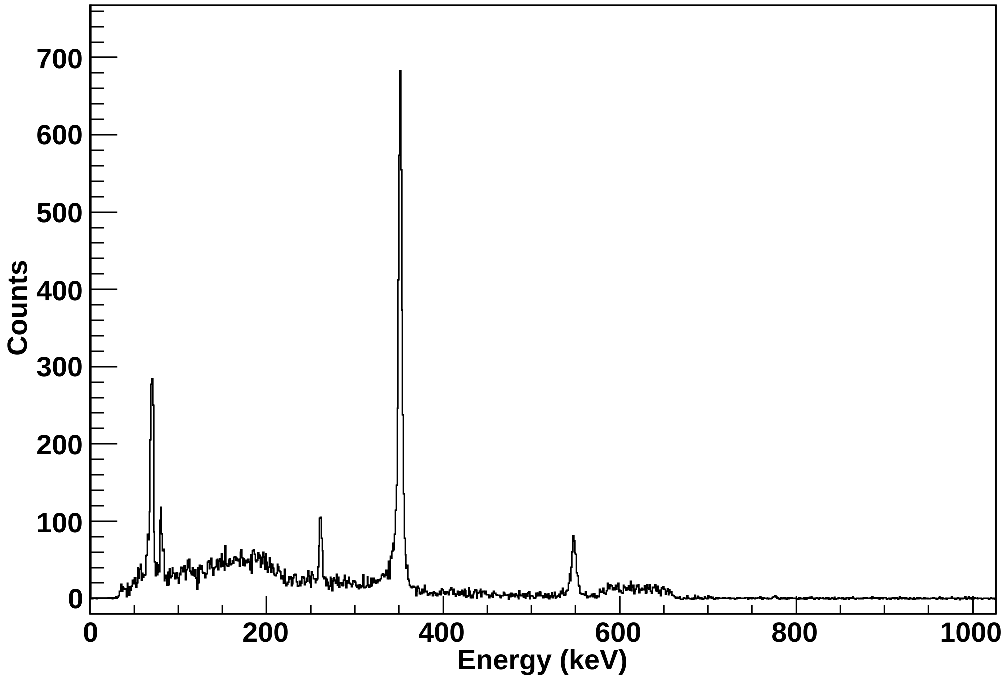

Figure 5.7: ^{182}Hg γ-ray energy spectrum when considering the whole range of the CD detector. The spectrum is the difference between prompt and random γ-particle-particle coincidences as defined in § 5.3 and is Doppler corrected for ^{182}Hg particles.

5.4 Spectroscopy of ^{182,186}Hg and ^{112,114}Cd Via Coulomb Excitation

5.4.1 ^{112}Cd(^{182}Hg,^{182}Hg*) Experimental Yields

The random-background subtracted, Doppler-corrected γ-ray energy spectrum obtained when considering all the angular range of the CD detector is shown in Figure 5.7. Only γ rays in coincidence with both a target and projectile nucleus have been recorded within this spectrum. The $2_1^+ \rightarrow 0_1^+$ transition in ^{112}Cd can be observed at approximately 617.5 keV. The large FWHM is due to the spectrum being Doppler corrected for ^{182}Hg and not ^{112}Cd. The yield for this transition is taken from an identical spectrum that has been Doppler corrected for ^{112}Cd instead of ^{182}Hg. This gives a much sharper lineshape for the ^{112}Cd transition, and therefore a more accurate measurement of the yield. Transitions

^{112}Cd(^{182}Hg,^{182}Hg*) Experimental Yields - All CD Detector			
Nucleus	E_γ (keV)	$I_i^\pi \rightarrow I_f^\pi$	N_γ
^{112}Cd	617.52	$2_1^+ \rightarrow 0_1^+$	768 ± 40
^{182}Hg	351.8	$2_1^+ \rightarrow 0_1^+$	3591 ± 81
^{182}Hg	548.6	$2_2^+ \rightarrow 0_1^+$	510 ± 39
^{182}Hg	261.4	$4_1^+ \rightarrow 2_1^+$	321 ± 33
^{182}Hg	196.8	$2_2^+ \rightarrow 2_1^+$	101 ± 29
^{182}Hg	68	k_α x-ray	1260 ± 53

Table 5.5: Experimental yields for the reaction ^{112}Cd(^{182}Hg,^{182}Hg*). All yields are obtained from the spectrum in Figure 5.7 except the ^{112}Cd $2_1^+ \rightarrow 0_1^+$ yield which was obtained from an identical spectrum that was Doppler corrected for ^{112}Cd.

observed belonging to ^{182}Hg include the $2_1^+ \rightarrow 0_1^+$ transition at 351 keV, the $2_2^+ \rightarrow 0_1^+$ transition at 549 keV, the $4_1^+ \rightarrow 2_1^+$ transition at 262 keV and the $2_2^+ \rightarrow 2_1^+$ transition at 196 keV. This final transition is somewhat unfortunately situated on the Compton continuum edge. Prominent X-ray peaks associated to ^{182}Hg are also observed at energies of 68 kev and 80 keV. The enhanced nature of these peaks suggest a strong E0 component to the $2_2^+ \rightarrow 2_1^+$ transition and a contribution to the total X-ray yield from an unobserved $0_2^+ \rightarrow 0_1^+$ transition. The fitted intensities of the observed transitions are listed in Table 5.5. When applying the angular cuts, discussed in § 5.3, the data is split into three distinct experiments corresponding to the angular ranges defined by the cuts. Figure 5.8 to Figure 5.10 depict the spectra obtained for each of these angular ranges when a γ ray is recorded in coincidence with both a target and projectile nucleus detected in the CD particle detector. The spectra again have the random background coincidences subtracted and are Doppler corrected for ^{182}Hg. All transitions observed in Figure 5.7 are again observed, though obviously with less counts. Table 5.6 to Table 5.8 list the fitted intensities for each observed transition in each defined angular range.

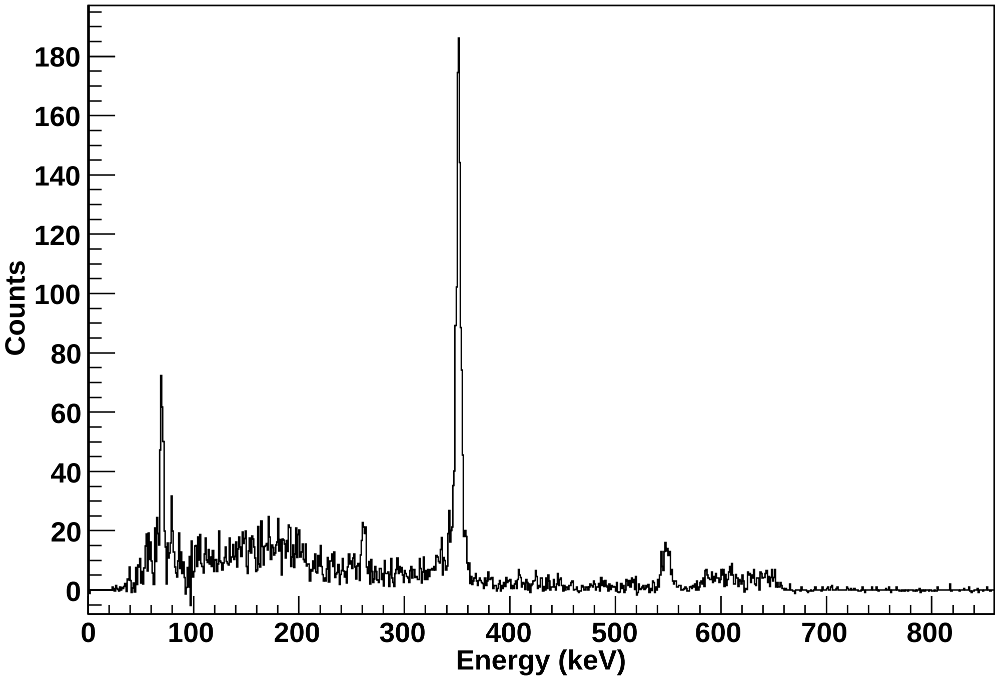

Figure 5.8: ^{182}Hg γ-ray energy spectrum when considering the Low COM angular range. The spectrum is the difference between prompt and random γ-particle-particle coincidences as defined in § 5.3 and is Doppler corrected for ^{182}Hg particles.

^{112}Cd(^{182}Hg,^{182}Hg*) Experimental Yields - Low COM			
Nucleus	E_γ (keV)	$I_i^\pi \rightarrow I_f^\pi$	N_γ
^{112}Cd	617.52	$2_1^+ \rightarrow 0_1^+$	186 ± 21
^{182}Hg	351.8	$2_1^+ \rightarrow 0_1^+$	936 ± 42
^{182}Hg	548.6	$2_2^+ \rightarrow 0_1^+$	89 ± 15
^{182}Hg	261.4	$4_1^+ \rightarrow 2_1^+$	80 ± 16
^{182}Hg	196.8	$2_2^+ \rightarrow 2_1^+$	26 ± 9
^{182}Hg	68	k_α x-ray	256 ± 17

Table 5.6: Experimental yields for the reaction ^{112}Cd(^{182}Hg,^{182}Hg*) when using the Low COM angular range, as defined in Table 5.3. All yields are obtained from the spectrum in Figure 5.8 except the ^{112}Cd $2_1^+ \rightarrow 0_1^+$ yield which was obtained from an identical spectrum that was Doppler corrected for ^{112}Cd.

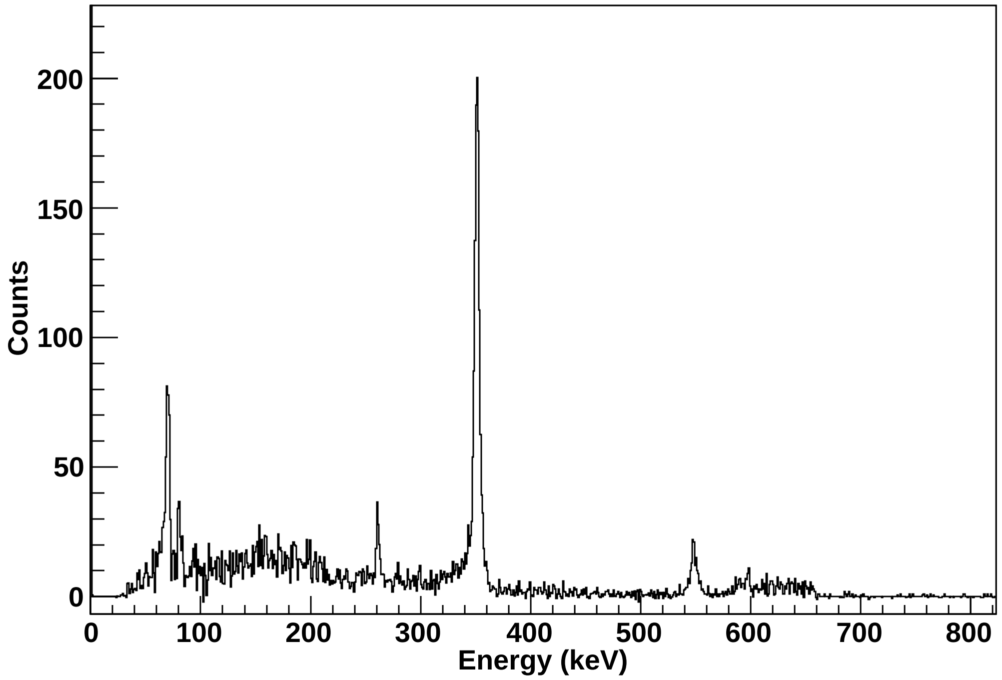

Figure 5.9: ^{182}Hg γ-ray energy spectrum when considering the Med COM angular range. The spectrum is the difference between prompt and random γ-particle-particle coincidences as defined in § 5.3 and is Doppler corrected for ^{182}Hg particles.

^{112}Cd(^{182}Hg,^{182}Hg*) Experimental Yields - Med COM			
Nucleus	E_γ (keV)	$I^\pi_i \rightarrow I^\pi_f$	N_γ
^{112}Cd	617.52	$2^+_1 \rightarrow 0^+_1$	219 ± 22
^{182}Hg	351.8	$2^+_1 \rightarrow 0^+_1$	1210 ± 51
^{182}Hg	548.6	$2^+_2 \rightarrow 0^+_1$	149 ± 18
^{182}Hg	261.4	$4^+_1 \rightarrow 2^+_1$	105 ± 18
^{182}Hg	196.8	$2^+_2 \rightarrow 2^+_1$	31 ± 9
^{182}Hg	68	k_α x-ray	330 ± 20

Table 5.7: Experimental yields for the reaction ^{112}Cd(^{182}Hg,^{182}Hg*) when using the Med COM angular range, as defined in Table 5.3. All yields are obtained from the spectrum in Figure 5.9 except the ^{112}Cd $2^+_1 \rightarrow 0^+_1$ yield which was obtained from an identical spectrum that was Doppler corrected for ^{112}Cd.

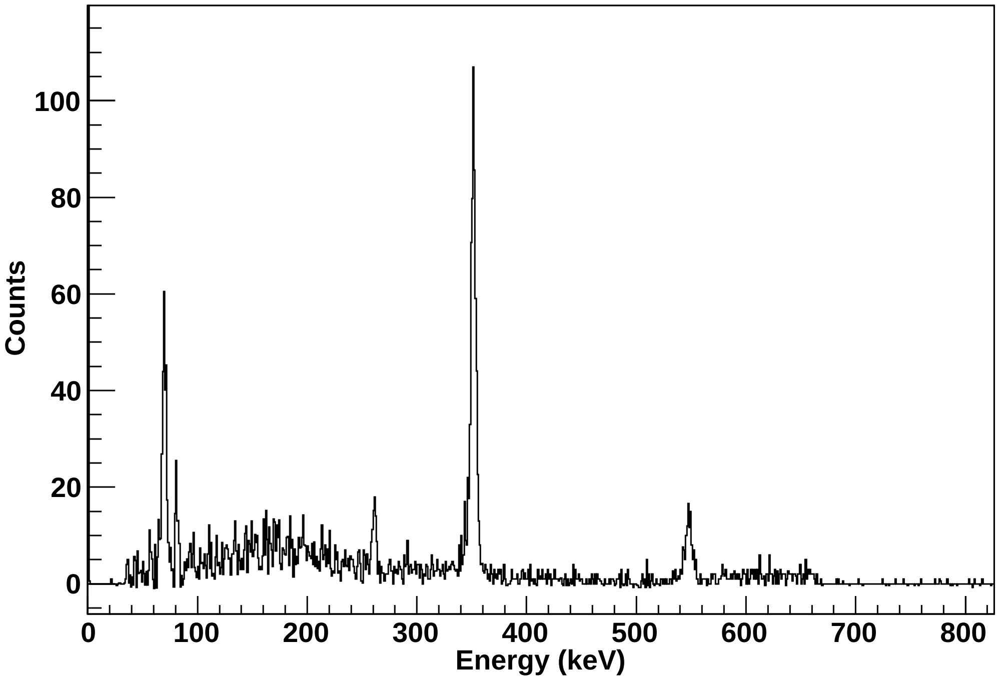

Figure 5.10: ^{182}Hg γ-ray energy spectrum when considering the High COM angular range. The spectrum is the difference between prompt and random γ-particle-particle coincidences as defined in § 5.3 and is Doppler corrected for ^{182}Hg particles.

^{112}Cd(^{182}Hg,^{182}Hg*) Experimental Yields - High COM

Nucleus	E_γ (keV)	$I_i^\pi \rightarrow I_f^\pi$	N_γ
^{112}Cd	617.52	$2_1^+ \rightarrow 0_1^+$	82 ± 10
^{182}Hg	351.8	$2_1^+ \rightarrow 0_1^+$	510 ± 33
^{182}Hg	548.6	$2_2^+ \rightarrow 0_1^+$	103 ± 15
^{182}Hg	261.4	$4_1^+ \rightarrow 2_1^+$	74 ± 13
^{182}Hg	196.8	$2_2^+ \rightarrow 2_1^+$	12 ± 8
^{182}Hg	68	k_α x-ray	244 ± 16

Table 5.8: Experimental yields for the reaction ^{112}Cd(^{182}Hg,^{182}Hg*) when using the High COM angular range, as defined in Table 5.3. All yields are obtained from the spectrum in Figure 5.10 except the ^{112}Cd $2_1^+ \rightarrow 0_1^+$ yield which was obtained from an identical spectrum that was Doppler corrected for ^{112}Cd.

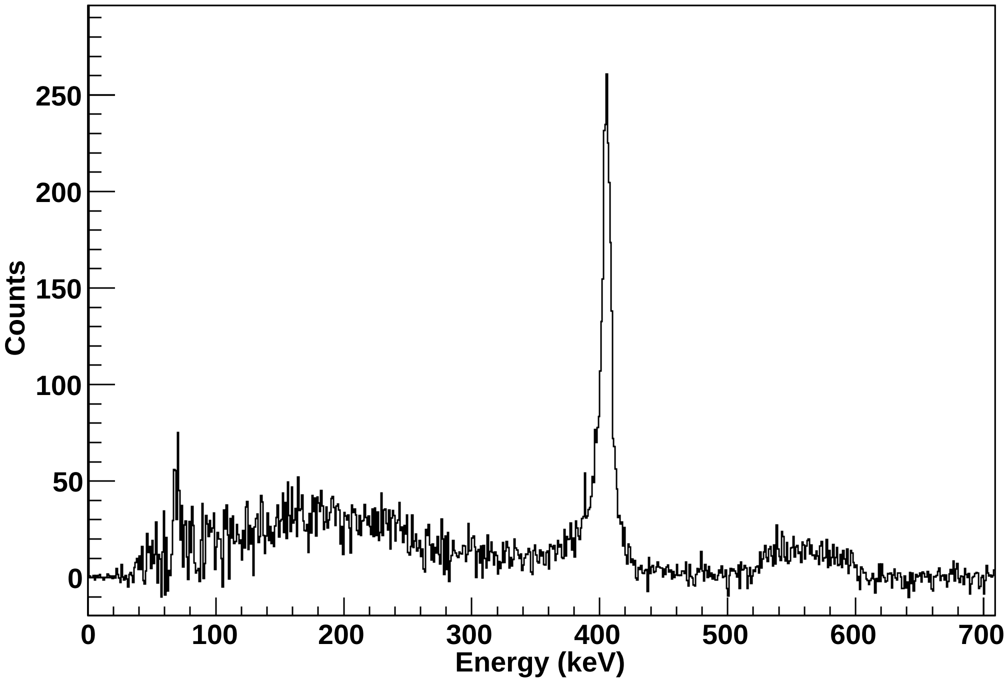

Figure 5.11: ^{186}Hg γ-ray energy spectrum when considering the whole range of the CD detector. The spectrum is the difference between prompt and random γ-particle-particle coincidences as defined in § 5.3 and is Doppler corrected for ^{186}Hg particles.

5.4.2 ^{114}Cd(^{186}Hg,^{186}Hg*) Experimental Yields

The random background subtracted, Doppler corrected γ-ray energy spectrum obtained when considering the whole angular range of the CD detector is shown in Figure 5.11. Only γ rays in coincidence with both a target and projectile nucleus have been recorded within this spectrum. The $2^+_1 \rightarrow 0^+_1$ transition in ^{114}Cd can be observed at approximately 558.4 keV. Again a large FWHM is observed for the cadmium transition due to the spectrum being Doppler corrected for ^{186}Hg and not ^{114}Cd. The yield for this transition is taken from an identical spectrum that has been Doppler corrected for ^{114}Cd instead of ^{186}Hg. Transitions observed belonging to ^{186}Hg include the $2^+_1 \rightarrow 0^+_1$ transition at 405.33 keV and X-ray peaks associated to ^{186}Hg at energies of approximately 68 kev and 80 keV. The $4^+_1 \rightarrow 2^+_1$ transition at 402.66 keV lies in the tail of the $2^+_1 \rightarrow 0^+_1$ transition and is unobserved. Due to the weak population of the 4^+_1 state, little yield from this transition is expected. The fitted intensities of the observed transitions are listed in Table 5.5.

^{114}Cd(^{186}Hg,^{186}Hg*) Experimental Yields - All CD Detector			
Nucleus	E_γ (keV)	$I_i^\pi \to I_f^\pi$	N_γ
^{114}Cd	558.4	$2_1^+ \to 0_1^+$	583 ± 22
^{186}Hg	405.3	$2_1^+ \to 0_1^+$	1815 ± 41
^{186}Hg	68	k_α x-ray	68 ± 28

Table 5.9: Experimental yields for the reaction ^{114}Cd(^{186}Hg,^{186}Hg*). All yields are obtained from the spectrum in Figure 5.11 except the ^{114}Cd $2_1^+ \to 0_1^+$ yield which was obtained from an identical spectrum that was Doppler corrected for ^{114}Cd.

When applying the angular cuts, discussed in § 5.3, the data is split into three distinct experiments corresponding to the angular ranges defined by the cuts. Figure 5.12 to Figure 5.14 depict the spectra obtained for each of these angular ranges when a γ ray is recorded in coincidence with both a target and projectile nucleus in the CD particle detector. The spectra again have the random-background coincidences subtracted and are Doppler corrected for ^{186}Hg. All transitions in Figure 5.11 are again observed, though obviously with less counts. Table 5.10 - Table 5.12 list the fitted intensities for each observed transition in each defined angular range.

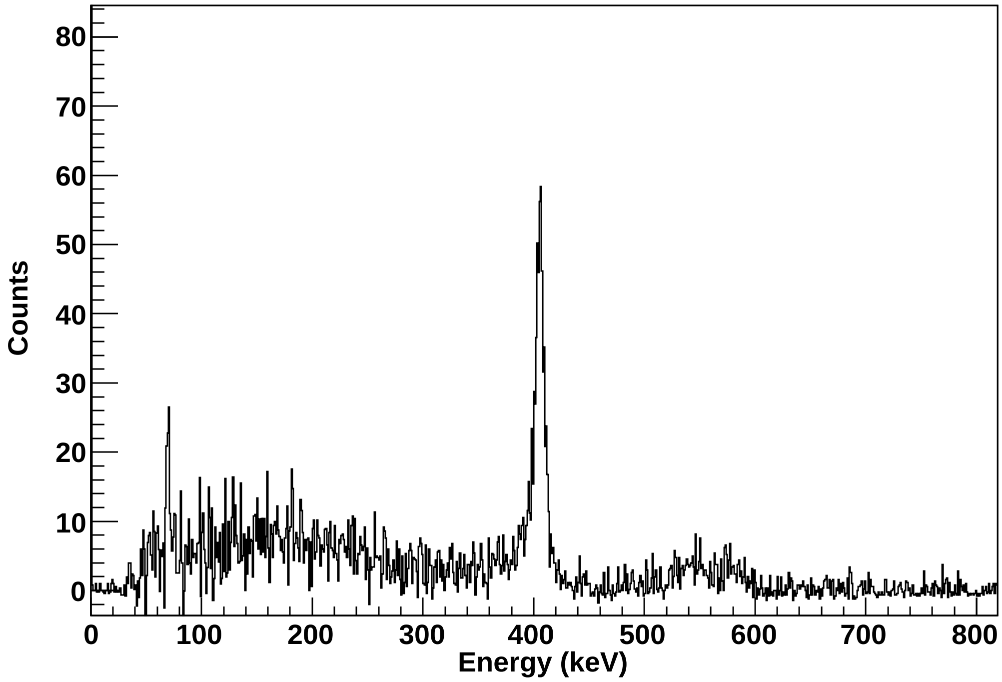

Figure 5.12: ^{186}Hg γ-ray energy spectrum when considering the Low COM angular range. The spectrum is the difference between prompt and random γ-particle-particle coincidences as defined in § 5.3 and is Doppler corrected for ^{186}Hg particles.

^{114}Cd(^{186}Hg,^{186}Hg*) Experimental Yields - Low COM

Nucleus	E_γ (keV)	$I^\pi_i \rightarrow I^\pi_f$	N_γ
^{114}Cd	558.4	$2^+_1 \rightarrow 0^+_1$	253 ± 15
^{186}Hg	405.3	$2^+_1 \rightarrow 0^+_1$	778 ± 27
^{186}Hg	68	k_α x-ray	31 ± 21

Table 5.10: Experimental yields for the reaction ^{114}Cd(^{186}Hg,^{186}Hg*) when using the Low COM angular range, as defined in Table 5.4. All yields are obtained from the spectrum in Figure 5.12 except the ^{114}Cd $2^+_1 \rightarrow 0^+_1$ yield which was obtained from an identical spectrum that was Doppler corrected for ^{114}Cd.

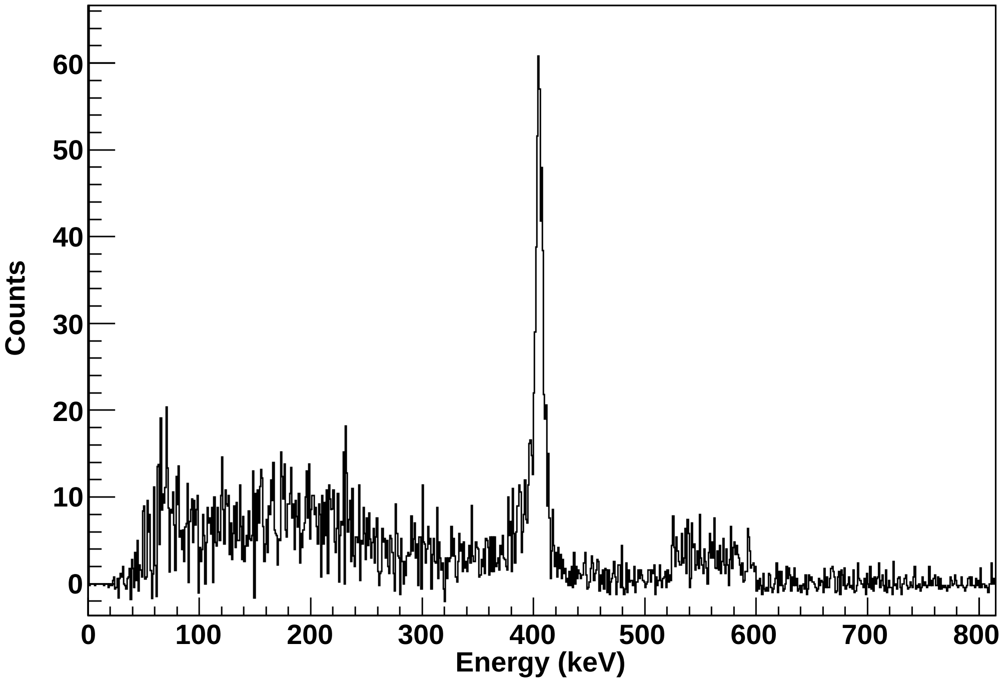

Figure 5.13: ^{186}Hg γ-ray energy spectrum when considering the Med COM angular range. The spectrum is the difference between prompt and random γ-particle-particle coincidences as defined in § 5.3 and is Doppler corrected for ^{186}Hg particles.

^{114}Cd(^{186}Hg,^{186}Hg*) Experimental Yields - Med COM			
Nucleus	E$_\gamma$ (keV)	$I^\pi_i \rightarrow I^\pi_f$	N$_\gamma$
^{114}Cd	558.4	$2^+_1 \rightarrow 0^+_1$	219 ± 16
^{186}Hg	405.3	$2^+_1 \rightarrow 0^+_1$	696 ± 36
^{186}Hg	68	k$_\alpha$ x-ray	28 ± 17

Table 5.11: Experimental yields for the reaction ^{114}Cd(^{186}Hg,^{186}Hg*) when using the Med COM angular range, as defined in Table 5.4. All yields are obtained from the spectrum in Figure 5.13 except the ^{114}Cd $2^+_1 \rightarrow 0^+_1$ yield which was obtained from an identical spectrum that was Doppler corrected for ^{114}Cd.

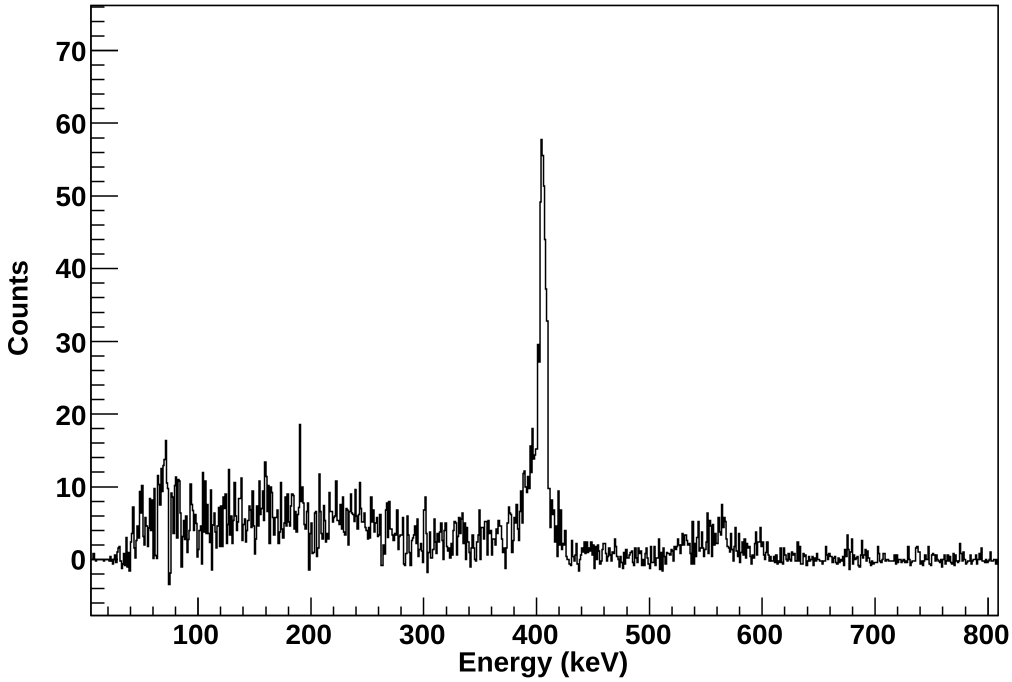

Figure 5.14: ^{186}Hg γ-ray energy spectrum when considering the High COM angular range. The spectrum is the difference between prompt and random γ-particle-particle coincidences as defined in § 5.3 and is Doppler corrected for ^{186}Hg particles.

^{114}Cd(^{186}Hg,^{186}Hg*) Experimental Yields - High COM

Nucleus	E_γ (keV)	$I_i^\pi \rightarrow I_f^\pi$	N_γ
^{114}Cd	558.4	$2_1^+ \rightarrow 0_1^+$	151 ± 13
^{186}Hg	405.3	$2_1^+ \rightarrow 0_1^+$	485 ± 22
^{186}Hg	68	k_α x-ray	15 ± 11

Table 5.12: Experimental yields for the reaction ^{114}Cd(^{186}Hg,^{186}Hg*) when using the High COM angular range, as defined in Table 5.4. All yields are obtained from the spectrum in Figure 5.14 except the ^{114}Cd $2_1^+ \rightarrow 0_1^+$ yield which was obtained from an identical spectrum that was Doppler corrected for ^{114}Cd.

5.5 ^{112}Cd(^{182}Hg,^{182}Hg*) GOSIA Analysis

5.5.1 Coulomb Excitation Yields

The electromagnetic properties of the low-lying states in the target nucleus ^{112}Cd are well known. This allows for the Coulomb-excitation yield of the $0^+_1 \rightarrow 2^+_1$ transition, which is proportional to the average integrated Coulomb-excitation cross section, to be calculated with the analysis code GOSIA. A relative calculation of the Coulomb-excitation yields for the projectile nucleus, ^{182}Hg, can then be made which neglects experimental uncertainties such as absolute beam current and data acquisition dead time.

^{112}Cd Coulomb Excitation Yields

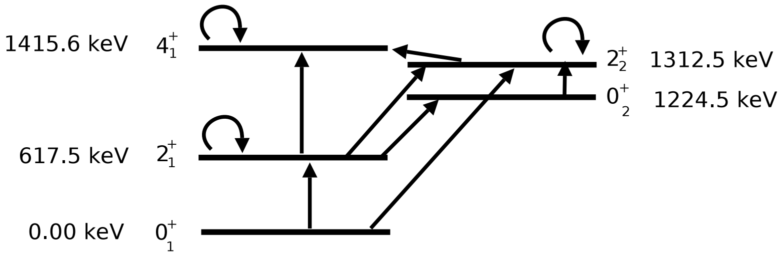

Figure 5.15: Low-lying levels in ^{112}Cd considered in the analysis. Straight arrows represent transitional couplings between states. Curly arrows represent diagonal self-couplings due to the reorientation of the magnetic substates.

The Coulomb excitation yield for the $2^+ \rightarrow 0^+$ transition in ^{112}Cd has been calculated using GOSIA for the three angular ranges defined in Table 5.3. All significant couplings, detailed in Figure 5.15, to the low-lying levels have been included in the calculation.

The reduced matrix elements used in the analysis, and used for GOSIA input, are listed in Table 5.13. The $\langle 2^+_1||E2||0^+_1\rangle$ has been taken from the weighted average of results obtained in [EKSB76, STSH85]. $\langle 2^+_1||E2||2^+_1\rangle$ is the weighted average of results published in [EKSB76, MPC$^+$77]. $\langle 4^+_1||E2||2^+_1\rangle$ has been obtained from a weighted average of results obtained in [MRSF65, JKB78]. $\langle 2^+_2||E2||0^+_1\rangle$ has been taken from [MMS$^+$69].$\langle 2^+_1||E2||0^+_2\rangle$ has been obtained from [LBC69]

^{112}Cd Matrix Elements	
$\langle 2_1^+ \vert\vert E2 \vert\vert 0_1^+ \rangle$	-0.696(3)
$\langle 2_1^+ \vert\vert E2 \vert\vert 2_1^+ \rangle$	-0.62(6)
$\langle 2_1^+ \vert\vert E2 \vert\vert 0_2^+ \rangle$	+0.38(6)
$\vert\langle 2_2^+ \vert\vert E2 \vert\vert 0_1^+ \rangle\vert$	0.102(7)
$\langle 2_2^+ \vert\vert E2 \vert\vert 0_2^+ \rangle$	0.0
$\langle 2_2^+ \vert\vert E2 \vert\vert 2_1^+ \rangle$	-0.59(3)
$\langle 2_2^+ \vert\vert E2 \vert\vert 2_2^+ \rangle$	0.0
$\langle 4_1^+ \vert\vert E2 \vert\vert 2_1^+ \rangle$	+1.31(9)
$\langle 4_1^+ \vert\vert E2 \vert\vert 2_2^+ \rangle$	0.0
$\langle 4_1^+ \vert\vert E2 \vert\vert 4_1^+ \rangle$	0.0

Table 5.13: Reduced transitional and diagonal matrix elements for ^{112}Cd for all significant couplings.

and $\langle 2_2^+||E2||2_1^+\rangle$ from [HAMD71]. As there are currently no published values for $\langle 2_2^+||E2||2_2^+\rangle$, $\langle 4_1^+||E2||4_1^+\rangle$, $\langle 2_2^+||E2||0_2^+\rangle$ and $\langle 4_1^+||E2||2_2^+\rangle$ arbitary values were used as input for GOSIA. It was found that these matrix elements had no significant effect on the calculated yield for the $2_1^+ \rightarrow 0_1^+$ transition. The Coulomb excitation yield has been calculated for each centre-of-mass range using the matrix elements listed in Table 5.13 by integrating over the full target thickness. Uncertainty on the calculated yields arise from the uncertainties on the experimental values of the transitional and diagonal matrix elements. The upper limit on the integrated yield is calculated using the most positive, and therefore least destructive, value of the diagonal matrix element and the upper limit of the transitional matrix element. Similarly, the lower limit on the integrated yield is obtained by using the lower limit of the transitional matrix element and the most negative, and therefore least constructive value of the diagonal matrix element.

Due to the sign ambiguity in the triple product of E2 couplings between the 0_1^+, 2_1^+ and 2_2^+ states the values quoted in Table 5.14 are an average of two results. One result is obtained when the sign of this triple product is positive, and the

^{112}Cd Integrated Coulomb Excitation Cross Sections

$I_i^\pi \rightarrow I_f^\pi$	$\sigma_{CE}(^{112}Cd)$ Low	$\sigma_{CE}(^{112}Cd)$ Med	$\sigma_{CE}(^{112}Cd)$ High
$2_1^+ \rightarrow 0_1^+$	6.4 ± 0.2	6.7 ± 0.2	1.9 ± 0.1
$4_1^+ \rightarrow 2_1^+$	0.06 ± 0.01	0.09 ± 0.02	0.022 ± 0.003
$2_2^+ \rightarrow 2_1^+$	0.0029 ± 0.0001	0.0041 ± 0.0003	0.0014 ± 0.0002

Table 5.14: Integrated Coulomb excitation cross sections for transitions in ^{112}Cd for each COM range investigated (denoted by Low, Med, High referring to the ranges defined in Table 5.3). Quoted values are averages of values obtained for both positive and negative values of the triple product of matrix elements coupling the 0_1^+, 2_1^+ and 2_2^+ states and are given in units of mb/srad·mg/cm^2.

interference is constructive. The other result used to obtain the average is found when the sign of the triple product is negative, and the interference is destructive. In reality it was found that there was little difference between the results obtained for each sign of the triple product.

It is quite apparent from the calculated yields in Table 5.14 that very little excitation to states other than the 2_1^+ state will occur. The influence of higher lying states on the yield of the $2_1^+ \rightarrow 0_1^+$ will therefore be negligible.

^{182}Hg Coulomb Excitation Yields

By comparing the measured γ-ray intensities, Coulomb excitation yields to the 2_1^+, 2_2^+ and 4_1^+ states have been calculated relative to the $2_1^+ \rightarrow 0_1^+$ transition in ^{112}Cd for the three defined centre-of-mass ranges using the method described in § 2.1.7 and a modified version of Equation 2.56 that incorporates the particular γ-ray yield for the transition in ^{182}Hg that is being investigated. γ-ray yields listed in Table 5.6 to Table 5.8 along with the corresponding Coulomb excitation yield to the 2_1^+ state in ^{112}Cd, listed in Table 5.14, have been used to calculate the Coulomb excitation yields for ^{182}Hg listed in Table 5.15. Efficiency correction factors and angular correction factors have been incorporated into the results. Values listed in Table 5.15 are average values, taking into account the constructive and destructive interference of the triple product of E2 couplings between the 0_1^+,

^{182}**Hg Integrated Coulomb Excitation Cross Sections**			
$I_i^{\pi} \rightarrow I_f^{\pi}$	$\sigma_{CE}(^{182}Hg)$ Low	$\sigma_{CE}(^{182}Hg)$ Med	$\sigma_{CE}(^{182}Hg)$ High
$2_1^+ \rightarrow 0_1^+$	23 ± 3	23 ± 3	6.6 ± 1.2
$2_2^+ \rightarrow 0_1^+$	6.9 ± 1.2	6.6 ± 1.2	1.6 ± 0.3
$4_1^+ \rightarrow 2_1^+$	3.1 ± 0.6	4.0 ± 0.8	1.2 ± 0.3

Table 5.15: Integrated Coulomb excitation cross sections for transitions in ^{182}Hg for each COM range investigated (denoted by Low, Med, High referring to the ranges defined in Table 5.3). Quoted values are averages of values obtained for both positive and negative values of the triple product of matrix elements coupling the 0_1^+, 2_1^+ and 2_2^+ states and are given in units of mb/srad·mg/cm^2.

2_1^+ and 2_2^+ states. Due to the Coulomb excitation yield being determined from a relative measurement, the uncertainty on the extracted yields are found from three contributing factors; the error on the ratio of γ-ray energy efficiencies, the statistical error on the ratio of measured γ-ray intensities and the uncertainties arising from the errors on the ^{112}Cd matrix elements.

5.5.2 Electromagnetic Matrix Elements of ^{182}Hg

Utilising the measured yields listed in Table 5.15 a χ^2 minimization was performed using GOSIA. Resulting matrix elements and the corresponding *B(E2)* and quadrupole moments are listed in Table 5.16 for transitions with observed experimental yields. The listed matrix elements were treated as free variables and allowed to vary in order to find the lowest value of χ^2 for a set of matrix elements that could reproduce the measured yield to within 1σ error bars. All significant couplings between states up to the 6_1^+ state in the ground state band and the 4_2^+ state in the intruder band have been included in the GOSIA fit to account for feeding due to virtual excitation to higher lying states.

Lifetimes of the 2_1^+, 4_1^+ and 6_1^+ states [GPS$^+$09], listed in Table 4.3, were included as separate data points. *B(E2)* values for the $2_1^+ \rightarrow 0_1^+$, $4_1^+ \rightarrow 2_1^+$ and $6_1^+ \rightarrow 4_1^+$ transitions were obtained from these measurements and included as

^{182}Hg Matrix Elements and Associated Parameters		
$\langle$I$\|\|$E2$\|\|$F$\rangle$	Value (eb)	$B(E2)$ or Q_s (eb)
$\langle 2_1^+ \|\| E2 \|\| 0_1^+ \rangle$	-1.34 ± 0.07	+0.36 ± 0.04
$\langle 2_1^+ \|\| E2 \|\| 2_1^+ \rangle$	-0.6 ± 0.5	-0.5 ± 0.4
$\langle 2_2^+ \|\| E2 \|\| 0_1^+ \rangle$	-1.06 ± 0.06	+0.23 ± 0.03
$\langle 2_2^+ \|\| E2 \|\| 2_2^+ \rangle$	+1.2 ± 0.9	+0.9 ± 0.8
$\langle 4_1^+ \|\| E2 \|\| 2_1^+ \rangle$	+3.7 ± 0.2	+1.5 ± 0.1
$\langle 4_1^+ \|\| E2 \|\| 4_1^+ \rangle$	-3 ± 2	-2.4 ± 1.7

Table 5.16: Reduced transitional and diagonal matrix elements for ^{182}Hg at the χ^2 minimum and the corresponding *B(E2)* and Q_s values.

starting points for the χ^2 minimization. All other unknown matrix elements were assigned random values by GOSIA each time a minimization was performed to ensure no bias. χ^2 minimizations were then performed until known lifetimes were reproduced and the minimum value of χ^2 found.

B(E2) values listed in Table 5.16 for the $2_1^+ \rightarrow 0_1^+$ and $4_1^+ \rightarrow 2_1^+$ transitions are in agreement with those obtained from lifetime measurements listed in Table 4.3. A value of $Q_{2_1^+}$ = -0.46 ± 0.4 eb implies the 2_1^+ state is most probably *prolate*, a conclusion in agreement with [GPS$^+$09]. With a value of $Q_{2_2^+}$ = +0.9 ± 0.8 eb, the 2_2^+ state can be described as most probably *oblate*. The small magnitude of these values suggest that these states are in fact strongly mixed. The 4_1^+ state, with a value of $Q_{4_1^+}$ = -2.4 ± 1.7 eb is again most probably *prolate* and belongs to the same band and the 2_1^+ state. The deformation of the 2_1^+, 2_2^+ and 4_1^+ states can be inferred from the transitional matrix elements and the quadrupole moments. Table 5.17 lists the β_2 values for these states. The values of β_2 for the 2_1^+ and 4_1^+ states listed in Table 5.17 are in agreement with those values listed in Table 4.3 obtained from lifetime measurements. A sign to the β_2 value has been inferred from the sign of the corresponding quadrupole moment.

^{182}Hg Deformation Parameters	
$\beta_2^{2_1^+}$	+0.139 ± 0.008
$\beta_2^{2_2^+}$	-0.11 ± 0.01
$\beta_2^{4_1^+}$	+0.25 ± 0.01

Table 5.17: β_2 values for the 2_1^+, 2_2^+ and 4_1^+ states in ^{182}Hg.

5.5.3 Shape Analysis of Low-Lying States in ^{182}Hg

2_1^+ state in ^{182}Hg

The cross section of the $2_1^+ \rightarrow 0_1^+$ transition in ^{182}Hg has been derived for the three angular ranges defined in Table 5.3 relative to the $2_1^+ \rightarrow 0_1^+$ transition in ^{112}Cd. Table 5.15 lists the mean value of the Coulomb-excitation cross section in the three defined angular ranges along with the extreme $\pm\sigma$ values. Varying the $\langle 2_1^+||\mathrm{E2}||0_1^+\rangle$ and $\langle 2_1^+||\mathrm{E2}||2_1^+\rangle$ manually allows for a loci of points that can reproduce the extremes of the Coulomb-excitation cross section to be plotted. This was done for each defined angular range, producing three independent loci of points that reproduced the $\pm\sigma$ values of the Coulomb-excitation cross section. Each angular range has a different sensitivity to the quadrupole moment, as can be seen from Figure 2.2. The overlapping region of these bands therefore defines the range of values for $\langle 2_1^+||\mathrm{E2}||0_1^+\rangle$ and $\langle 2_1^+||\mathrm{E2}||2_1^+\rangle$ that can reproduce the measured Coulomb excitation cross section. This method provides a graphical check to the GOSIA χ^2 minimization that was discussed in § 5.5.2 Other significant couplings in the GOSIA calculation were set to the values obtained in the minimization discussed in § 5.5.2. Lifetime data points were not included in the calculation so as the matrix elements would be completely uninfluenced.

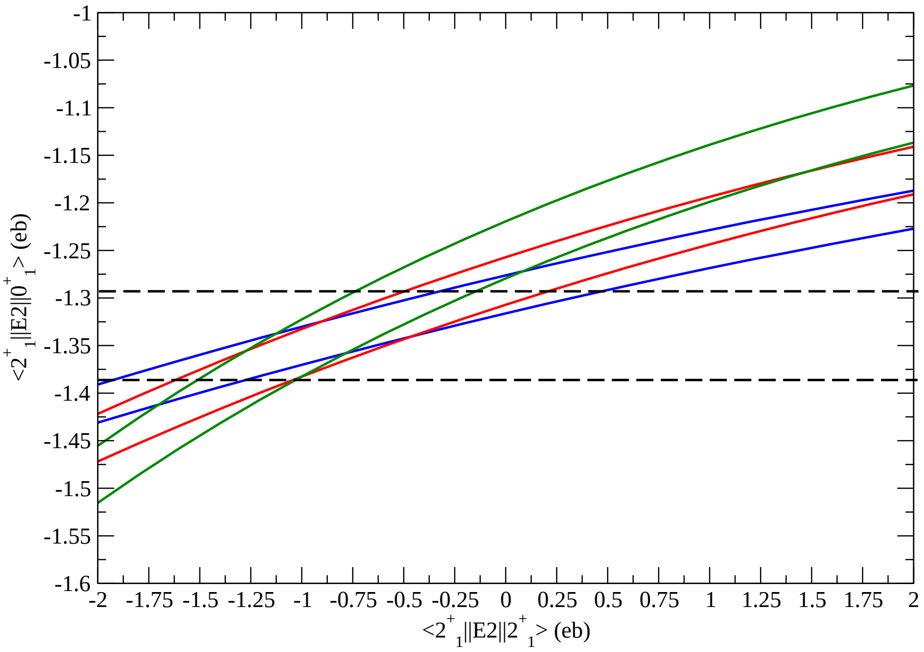

Figure 5.16: Variation of the $\langle 2_1^+||\mathrm{E2}||0_1^+\rangle$ as a function of $\langle 2_1^+||\mathrm{E2}||2_1^+\rangle$ in ^{182}Hg for the three angular ranges defined in Table 5.3. The solid blue(red,green) lines represent the extreme values of the matrix elements that reproduce the Coulomb excitation cross section in the Low COM (Med COM, High COM) angular range. The horizontal dashed black lines represent the experimental error values of $\langle 2_1^+||\mathrm{E2}||0_1^+\rangle$ as derived from lifetime measurements [GPS$^+$09].

Figure 5.16 shows the resulting loci of points that reproduce the Coulomb-excitation cross section for each defined angular range. It can be seen that the overlapping region defines a range for $\langle 2_1^+||\mathrm{E2}||0_1^+\rangle$ of ≈ -1.29 - -1.39 eb, in agreement with the value obtained from the GOSIA χ^2 minimization and the results from lifetime measurements. The error bar being larger due to the lifetime data points not being included. The range of $\langle 2_1^+||\mathrm{E2}||2_1^+\rangle$ is ≈ -0.1 - 1.1 eb, again in agreement with the GOSIA χ^2 minimization. Figure 5.16 goes some way to explaining the large error bar on $\langle 2_1^+||\mathrm{E2}||2_1^+\rangle$. This can be attributed to the sensitivity to the quadrupole moment in each of the defined angular ranges of the differential Coulomb excitation cross-section being very similar.

2_2^+ state in ^{182}Hg

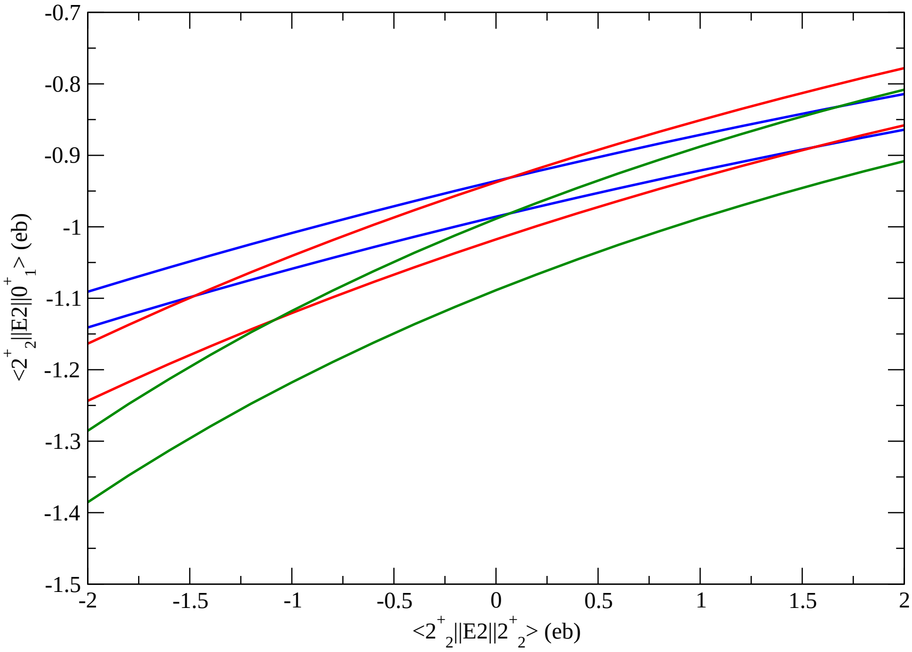

Figure 5.17: Variation of the $\langle 2_2^+||\mathrm{E2}||0_1^+\rangle$ as a function of $\langle 2_2^+||\mathrm{E2}||2_2^+\rangle$ in ^{182}Hg for the three angular ranges defined in Table 5.3. The solid blue(red,green) lines represent the extreme values of the matrix elements that reproduce the Coulomb-excitation cross section in the Low COM (Med COM, High COM) angular range.

As for the $2_1^+ \rightarrow 0_1^+$ transition in ^{182}Hg, the Coulomb-excitation cross section in the three defined angular ranges has been calculated relative to the $2_1^+ \rightarrow 0_1^+$ transition in ^{112}Cd for the $2_2^+ \rightarrow 0_1^+$. The $\pm\sigma$ values are again listed in Table 5.15. By varying the $\langle 2_2^+||\mathrm{E2}||0_1^+\rangle$ and $\langle 2_2^+||\mathrm{E2}||2_2^+\rangle$ manually, the loci of points that reproduce the $\pm\sigma$ values for the Coulomb excitation cross section have been obtained for each defined angular range.

Figure 5.17 shows the resulting loci of points that reproduce the Coulomb-excitation cross section for each defined angular range. The overlapping region defines a range for $\langle 2_2^+||\mathrm{E2}||0_1^+\rangle$ of $\approx$ -1.05 - -0.9 eb. This value agrees with the result from the GOSIA χ^2 minimization and has a larger error due to the lifetime data not being included. The range of values for $\langle 2_2^+||\mathrm{E2}||2_2^+\rangle$ obtained from the overlapping region is $\approx$ +0.1 - +2.1. Agreement with the GOSIA χ^2

minimization is also achieved. The sensitivity to the quadrupole moment of the Coulomb-excitation cross section for the 2_2^+ state is again small. This can be seen by the large overlapping region and the subsequently large error bars on the diagonal matrix element.

5.6 ^{114}Cd(^{186}Hg,^{186}Hg*) GOSIA Analysis

5.6.1 Coulomb Excitation Yields

The electromagnetic properties of the low-lying states in the target nucleus ^{114}Cd are well known. This allows for the Coulomb excitation yield of the $0_1^+ \rightarrow 2_1^+$ transition, which is proportional to the average integrated Coulomb excitation cross section, to be calculated with the analysis code GOSIA. A relative calculation of the Coulomb-excitation yields for the projectile nucleus, ^{186}Hg, can then be made which neglects experimental uncertainties such as absolute beam current and data acquisition dead time.

^{114}Cd Coulomb Excitation Yields

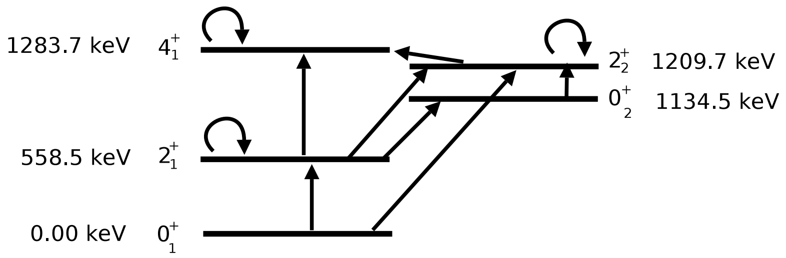

Figure 5.18: Low-lying levels in ^{114}Cd considered in the analysis. Straight arrows represent transitional couplings between states. Curly arrows represent diagonal self-couplings due to the reorientation of the magnetic substates.

The Coulomb-excitation yield for the $2^+ \rightarrow 0^+$ transition in ^{114}Cd has been calculated using GOSIA for the three angular ranges defined in Table 5.4. All significant couplings, detailed in Figure 5.18, to the low-lying levels have been included in the calculation. The reduced matrix elements used in the analysis,

^{114}**Cd Matrix Elements**	
$\langle 2_1^+\|\|\mathrm{E2}\|\|0_1^+\rangle$	+0.714(21)
$\langle 2_1^+\|\|\mathrm{E2}\|\|2_1^+\rangle$	-0.36(3)
$\langle 2_1^+\|\|\mathrm{E2}\|\|0_2^+\rangle$	+0.3000(9)
$\langle 2_2^+\|\|\mathrm{E2}\|\|0_1^+\rangle$	+0.091(3)
$\langle 2_2^+\|\|\mathrm{E2}\|\|0_2^+\rangle$	-0.17(4)
$\langle 2_2^+\|\|\mathrm{E2}\|\|2_1^+\rangle$	+0.684(20)
$\langle 2_2^+\|\|\mathrm{E2}\|\|2_2^+\rangle$	+0.92(5)
$\langle 4_1^+\|\|\mathrm{E2}\|\|2_1^+\rangle$	+1.35(4)
$\langle 4_1^+\|\|\mathrm{E2}\|\|2_2^+\rangle$	-0.35(7)
$\langle 4_1^+\|\|\mathrm{E2}\|\|4_1^+\rangle$	-0.95(11)

Table 5.18: Reduced transitional and diagonal matrix elements for ^{114}Cd for all significant couplings.

and used for GOSIA input, are listed in Table 5.18. All matrix elements listed are taken from [FBH$^+$88]. The Coulomb excitation yield has been calculated for each centre-of-mass range using the matrix elements listed in Table 5.18 by integrating over the full target thickness. Uncertainty on the calculated yields arise from the uncertainties on the experimental values of the transitional and diagonal matrix elements. The upper limit on the integrated yield is calculated using the most positive, and therefore least destructive, value of the diagonal matrix element and the upper limit of the transitional matrix element. Similarly, the lower limit on the integrated yield is obtained by using the lower limit of the transitional matrix element and the most negative, and therefore least constructive value of the diagonal matrix element.

Due to the sign ambiguity in the triple product of E2 couplings between the 0_1^+, 2_1^+ and 2_2^+ states the values quoted in Table 5.19 are an average of two results. One result is obtained when the sign of this triple product is positive, and the interference is constructive. The other result used to obtain the average is found when the sign of the triple product is negative, and the interference is destructive.

^{114}Cd Integrated Coulomb Excitation Cross Sections

$I_i^\pi \rightarrow I_f^\pi$	$\sigma_{CE}(^{114}Cd)$ Low	$\sigma_{CE}(^{114}Cd)$ Med	$\sigma_{CE}(^{114}Cd)$ High
$2_1^+ \rightarrow 0_1^+$	7.0 ± 0.4	5.3 ± 0.3	2.9 ± 0.2
$4_1^+ \rightarrow 2_1^+$	0.09 ± 0.01	0.07 ± 0.01	0.061 ± 0.003
$2_2^+ \rightarrow 2_1^+$	0.017 ± 0.003	0.014 ± 0.002	0.012 ± 0.002

Table 5.19: Integrated Coulomb ecitation cross sections for transitions in ^{114}Cd for each COM range investigated (denoted by Low, Med, High referring to the ranges defined in Table 5.4). Quoted values are averages of values obtained for both positive and negative values of the triple product of matrix elements coupling the 0_1^+, 2_1^+ and 2_2^+ states and are given in units of mb/srad·mg/cm^2.

In reality it was found that there was little difference between the results obtained for each sign of the triple product.

It is quite apparent from the calculated yields in Table 5.19 that very little excitation to states other than the 2_1^+ state will occur. The influence of higher lying states on the yield of the $2_1^+ \rightarrow 0_1^+$ will therefore be negligible.

^{186}Hg Coulomb Excitation Yields

By comparing the measured γ-ray intensities, Coulomb excitation yields to the 2_1^+ state have been calculated relative to the $2_1^+ \rightarrow 0_1^+$ transition in ^{114}Cd for the three defined centre-of-mass ranges using the method described in § 2.1.7. γ-ray yields listed in Table 5.10 - Table 5.12 along with the corresponding Coulomb excitation yield to the 2_1^+ state in ^{114}Cd, listed in Table 5.19, have been used to calculate the Coulomb excitation yields for ^{186}Hg listed in Table 5.20. Efficiency correction factors and angular correction factors have been incorporated into the results. Values listed in Table 5.20 are average values, taking into account the constructive and destructive interference of the triple product of E2 couplings between the 0_1^+, 2_1^+ and 2_2^+ states. Due to the Coulomb excitation yield being determined from a relative measurement, the uncertainty on the extracted yields are found from three contributing factors; the error on the ratio of γ-ray energy efficiencies, the statistical error on the ratio of measured γ-ray intensities and the

^{186}Hg Integrated Coulomb Excitation Cross Sections			
$I_i^\pi \rightarrow I_f^\pi$	$\sigma_{CE}(^{186}Hg)$ Low	$\sigma_{CE}(^{186}Hg)$ Med	$\sigma_{CE}(^{186}Hg)$ High
$2_1^+ \rightarrow 0_1^+$	16 ± 2	15 ± 2	5.6 ± 0.8

Table 5.20: Integrated Coulomb excitation cross sections for the $2_1^+ \rightarrow 0_1^+$ transition in ^{186}Hg for each COM range investigated (denoted by Low, Med, High referring to the ranges defined in Table 5.4). Quoted values are averages of values obtained for both positive and negative values of the triple product of matrix elements coupling the 0_1^+, 2_1^+ and 2_2^+ states and are given in units of mb/srad·mg/cm^2.

uncertainties arising from the errors on the ^{114}Cd matrix elements.

5.6.2 Electromagnetic Matrix Elements of ^{186}Hg

Utilising the measured yields listed in Table 5.20 a χ^2 minimization was performed using GOSIA. The resulting matrix elements and the corresponding *B(E2)* and quadrupole moments are listed in Table 5.21 for the $2_1^+ \rightarrow 0_1^+$ transition. Matrix elements were treated as free variables and allowed to vary in order to find the lowest value of χ^2 for a set of matrix elements that could reproduce the measured yield to within 1σ error bars. All significant couplings between states up to the 6_1^+ state in the ground state band and the 4_2^+ state in the γ band have been included in the GOSIA fit to account for feeding due to virtual excitation to higher-lying states.

Lifetimes of the 2_1^+, 4_1^+ [PDS73] and 2_2^+ [JZR$^+$94] states were included as separate data points. *B(E2)* values for the $2_1^+ \rightarrow 0_1^+$, $4_1^+ \rightarrow 2_1^+$ and $2_2^+ \rightarrow 0_1^+$ transitions were obtained from these measurements and included as starting points for the χ^2 minimization. All other unknown matrix elements were assigned random values by GOSIA each time a minimization was performed to ensure no bias. χ^2 minimizations were then performed until known lifetimes were reproduced and the minimum value of χ^2 found. The *B(E2)* value for the $2_1^+ \rightarrow 0_1^+$ transitions is in agreement with that of [PDS73]. A value of $Q_{2_1^+} = +1.7 \pm 0.5\,$eb implies the 2_1^+ state is *oblate*, in contrast to the 2_1^+ state in ^{182}Hg which was found to

^{186}Hg Matrix Elements and Associated Parameters		
$\langle$I||E2||F$\rangle$	Value (eb)	$B(E2)$ or Q_s (eb)
$\langle 2_1^+ \|\| \text{E2} \|\| 0_1^+ \rangle$	+1.2 ± 0.1	+0.3 ± 0.1
$\langle 2_1^+ \|\| \text{E2} \|\| 2_1^+ \rangle$	+2.1 ± 0.8	+1.7 ± 0.5

Table 5.21: Reduced transitional and diagonal matrix elements for ^{186}Hg at the χ^2 minimum and the corresponding *B(E2)* and Q_s values.

^{186}Hg Deformation Parameters	
$\beta_2^{2_1^+}$	-0.13 ± 0.02

Table 5.22: β_2 value for the 2_1^+ state in ^{186}Hg.

be *prolate*. The deformation of the 2_1^+ state can be inferred from the transitional matrix element and the quadrupole moment. Table 5.22 lists the β_2 value for the 2_1^+ state.

The magnitude of β_2 listed in Table 5.22 is of the same magnitude as that of the 2_1^+ state in ^{182}Hg. The sign of the β_2 value has been inferred from the sign of the corresponding quadrupole moment.

5.6.3 Shape Analysis of Low-Lying States in ^{186}Hg

2_1^+ state in ^{186}Hg

The cross section of the $2_1^+ \rightarrow 0_1^+$ transition in ^{186}Hg has been derived for the three angular ranges defined in Table 5.4 relative to the $2_1^+ \rightarrow 0_1^+$ transition in ^{114}Cd. Table 5.20 lists the mean value of the Coulomb excitation cross section in the three defined angular ranges along with the extreme $\pm\sigma$ values. Using the same method described in § 5.5.3, a graphical check to the GOSIA χ^2 minimization that was discussed in § 5.6.2 has been produced.

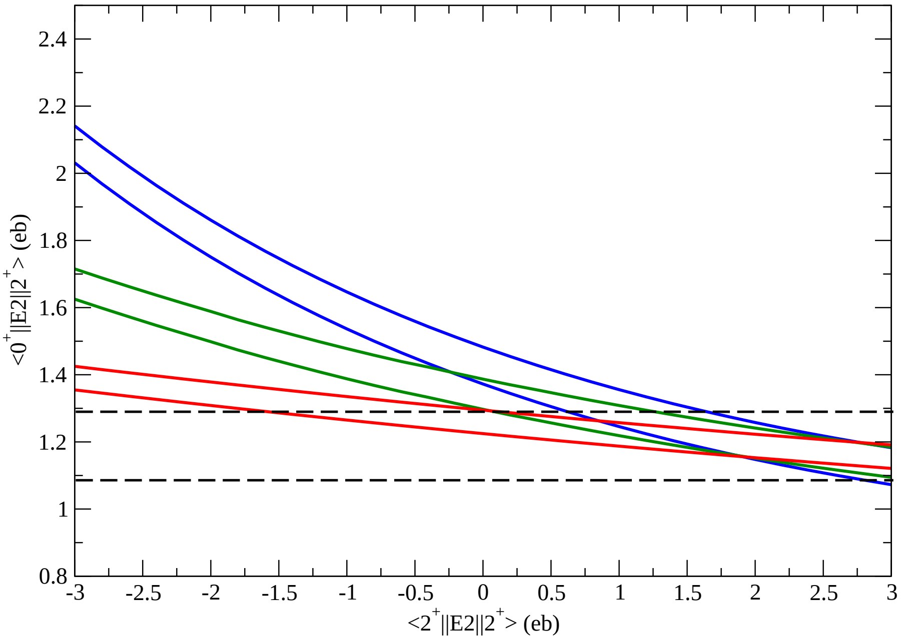

Figure 5.19: Variation of the $\langle 2_1^+||\mathrm{E2}||0_1^+\rangle$ as a function of $\langle 2_1^+||\mathrm{E2}||2_1^+\rangle$ in ^{186}Hg for the three angular ranges defined in Table 5.4. The solid red(green,blue) lines represent the extreme values of the matrix elements that reproduce the Coulomb excitation cross section in the Low COM (Med COM, High COM) angular range. The horizontal dashed black lines represent the 1σ values for $\langle 2_1^+||\mathrm{E2}||0_1^+\rangle$ as derived from previous lifetime measurements [PDS73].

Figure 5.19 shows the resulting loci of points that reproduce the Coulomb excitation cross section for each defined angular range. It can be seen that the overlapping region defines a range for $\langle 2_1^+||\mathrm{E2}||0_1^+\rangle$ of $\approx$ 1.05 - 1.22 eb, in agreement with the value obtained from the GOSIA χ^2 minimization and the results from lifetime measurements. The range of $\langle 2_1^+||\mathrm{E2}||2_1^+\rangle$ is $\approx$ 1.1 - 3.2 eb, again in agreement with the GOSIA χ^2 minimization. Figure 5.19 goes some way to explaining the large error bar on $\langle 2_1^+||\mathrm{E2}||2_1^+\rangle$. This can be attributed to the sensitivity to the quadrupole moment in each of the defined angular ranges of the differential Coulomb excitation cross section being very similar.

Chapter 6

Discussion

6.1 Collectivity in Neutron-Deficient Hg Isotopes

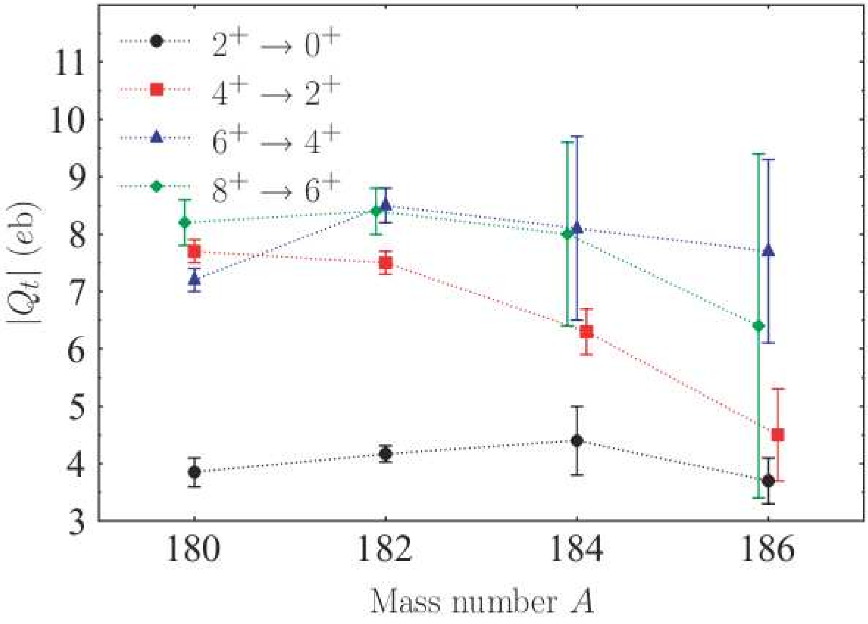

Figure 6.1: Experimental $|Q_t|$ values for yrast states up to $I^\pi = 8^+$ in ^{180,182,184,186,}Hg. Points have been slightly offset from the true value of A for clarity.

A transition from one nuclear shape to another can be inferred from $|Q_t|$ values. Figure 6.1 depicts experimental $|Q_t|$ values for ^{180,182,184,186,}Hg. $|Q_t|$ values for ^{180,182}Hg have been taken from [GPS$^+$09], $|Q_t|$ values for ^{184,186}Hg have been taken

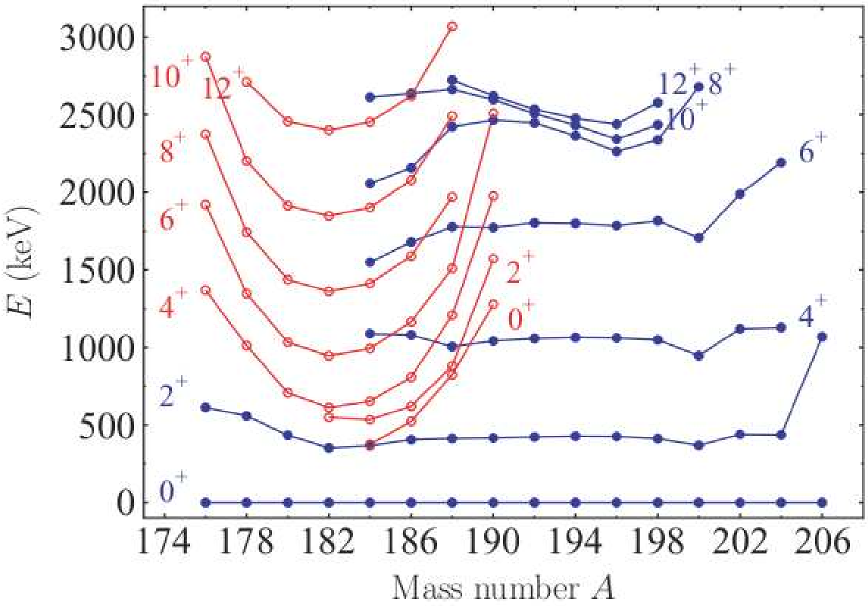

Figure 6.2: Energy level systematics for Hg isotopes. Prolate bands are depicted in red, oblate bands are depicted in blue.

from [MRH$^+$86] and [PDS73] respectively. The low $|Q_t|$ values for the 2^+ state in all four isotopes indicates a transition from the weakly deformed oblate ground state to a more deformed state. The $|Q_t|$ values from lifetime measurements cannot state whether a change from an oblate to prolate structure has occurred. When analysed in conjunction with Coulomb excitation data it can be concluded that the $|Q_t|$ value for the 2_1^+ state in ^{182}Hg is indicative of a transition from an *oblate* ground state to deformed *prolate* structure. Coulomb excitation data for ^{186}Hg leads to the conclusion that the 2_1^+ state is *oblate*, and more strongly deformed than the ground state. It is therefore clear that there is a transition from an *oblate* 2_1^+ state to a *prolate* 2_1^+ state going towards lighter nuclei in the isotopic chain. The $|Q_t|$ values in Figure 6.1 do not decrease with decreasing valence neutron space as would be expected beyond the neutron mid shell. One interpretation of this could be that the prolate intruder structure is mixing heavily with the spherical vibrational structure, as identified in ^{172}Hg [SGbuC$^+$09].

The mixing amplitude of the 2_1^+ state in ^{182}Hg can be estimated using a simple two-band mixing calculation using the $|Q_t|$ values. The lower collectivity of the

$2_1^+ \rightarrow 0_1^+$ transition compared to the other observed yrast transitions indicates that the 2_1^+ state is an admixture of prolate and oblate components. The weakly deformed oblate ground state is mixing heavily with the intruding states, which can be seen in Figure 6.2. An estimation of the mixing between the prolate and oblate structures for the 2_1^+ state was calculated using Equation 2.51. By assuming the final state of the $4_1^+ \rightarrow 2_1^+$ transition is mixed and that the average quadrupole moment of higher lying states relates to a pure rotational structure, an 80% *prolate* contribution to the wavefunction is calculated. This is in good agreement with band mixing calculations performed in [RBB$^+$97], which predict a 76% prolate contribution to the wavefunction of the 2_1^+ state in ^{182}Hg. The same work calculates a 50% prolate contribution to the wavefunction of the 2_1^+ state in ^{184}Hg and a 8% prolate contribution to the wavefunction of the 2_1^+ state in ^{186}Hg. The increasing prolate component as one decreases in neutron number is in good agreement with the Coulomb excitation data which shows a dominant oblate component to the wavefunction of the 2_1^+ state in ^{186}Hg and a mixed, but predominantly prolate structure to the 2_1^+ state in ^{182}Hg.

It can be seen in Figure 6.1 that the $|Q_t|$ value of the 4_1^+ state in ^{182}Hg is much higher than in ^{186}Hg. Looking to the level systematics in Figure 6.2 this can be accounted for by the prolate structure that reaches a minimum at $\mathrm{A} = 182$, and is consistent with high collectivity at the neutron mid shell. At $\mathrm{A} = 186$ an increase in level energies with decreasing neutron valence space indicates that it is less collective than its lighter neighbour.

Figure 6.3 shows $|Q_t|$ values of ^{182}Hg as a function of initial state spin along with the $|Q_t|$ values for neighbouring Hg and Pb isotopes. Data for ^{180,182}Hg are taken from [GPS$^+$09] whilst the data for the Pb isotopes are taken from [GDM$^+$06]. The near constant $|Q_t|$ values for the $I^\pi \geq 6^+$ states in ^{182}Hg indicates there prolate structure. The slightly lower value for $|Q_t|$ of the 4_1^+ state indicates the mixed nature of the 2_1^+ state in ^{182}Hg. The high $|Q_t|$ values indicates collective nature of ^{182}Hg. Comparing the $|Q_t|$ values of the light Hg isotopes to the light Pb isotopes in Figure 6.3, it can be concluded that the prolate bands of these

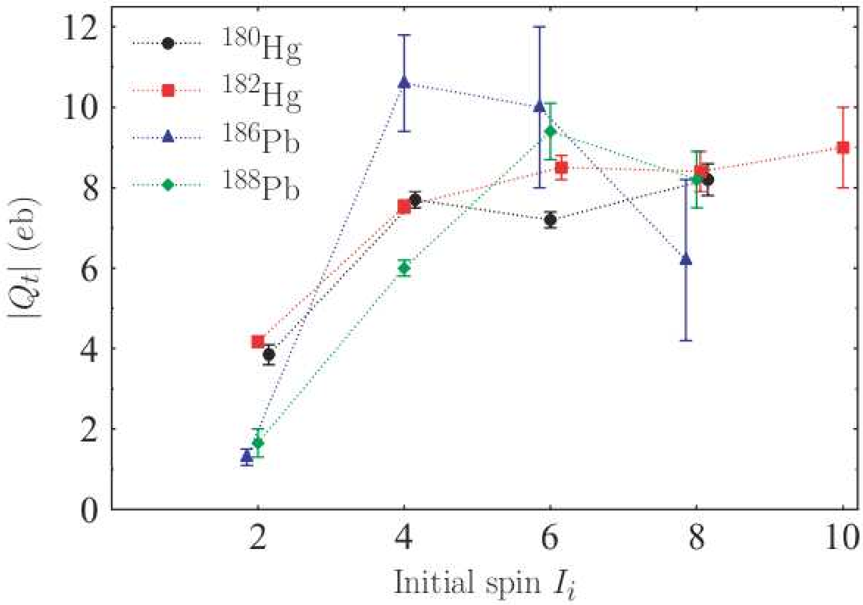

Figure 6.3: Experimental $|Q_t|$ values for neutron deficient Hg and Pb isotopes.

nuclei are similar and the behaviour in the mass region consistent.

6.2 Composition of the $2_2^+ \rightarrow 2_1^+$ Transition and the Effect on Matrix Elements

It is of interest to determine the E2, M1 and E0 components of the $2_2^+ \rightarrow 2_1^+$ transition. Though no unique solution can be found to this problem, due to insufficient data, a set of solutions can be found describing the percentage composition that can account for the observed X-ray yield.

The observed X-rays in Figure 5.7 can not be accounted for by internal conversion of the observed transitions alone. A strong E0 component to the $2_2^+ \rightarrow 2_1^+$ transition and an unobserved $0_2^+ \rightarrow 0_1^+$ E0 transition are likely to be the cause of the enhanced X-ray peak. To investigate the composition of the $2_2^+ \rightarrow 2_1^+$ transition a $\gamma\gamma$-coincidence matrix was produced. When gating on the $2_1^+ \rightarrow 0_1^+$ transition Figure 6.4 is obtained. In this spectrum the 68 keV K_α X-ray is visible, along with the 196 keV $2_2^+ \rightarrow 2_1^+$ and the 262 keV $4_1^+ \rightarrow 2_1^+$ transitions. Table 6.1

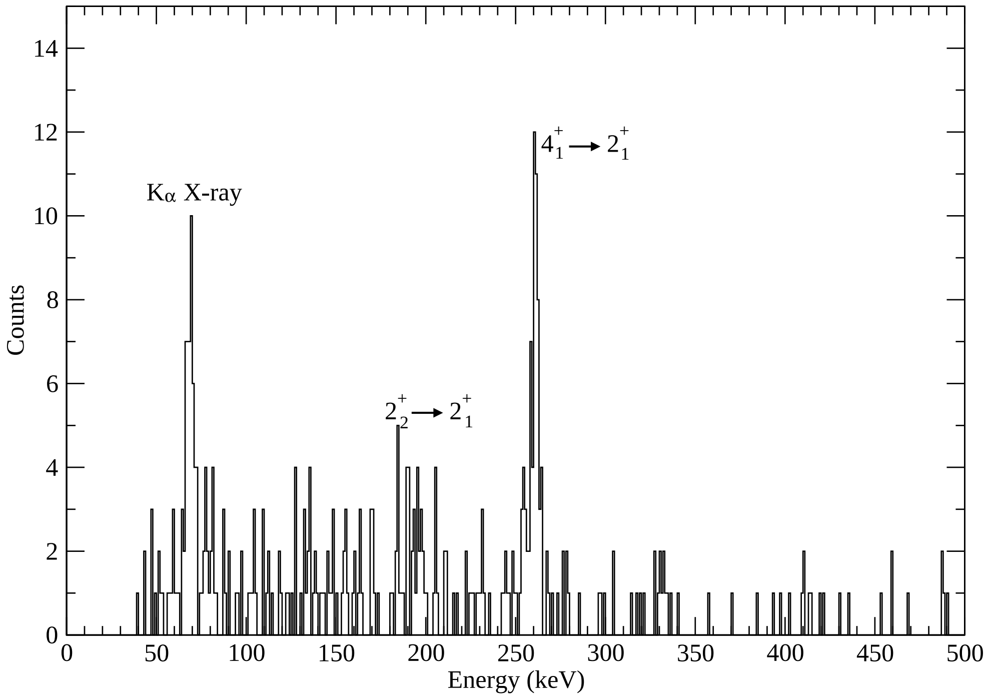

Figure 6.4: $\gamma\gamma$ coincidence spectrum when gating on the $2_1^+ \rightarrow 0_1^+$ transition. Spectrum has been Doppler corrected for ^{182}Hg.

lists the observed transitions and the efficiency-corrected counts.

The X-ray yield given in Table 6.1 is the sum of two contributing factors. X-rays due to internal conversion of the $4_1^+ \rightarrow 2_1^+$ transition can be easily calculated as this is a pure E2 transition. These account for 2.01±0.31 of the measured yield. The remaining X-ray yield originates from the $2_2^+ \rightarrow 2_1^+$ transition. The contribution to the X-ray yield from an E0 component of the $2_2^+ \rightarrow 2_1^+$ transition has been calculated using the following relation

$$X_{tot} = X_{IC_{4_1^+ \rightarrow 2_1^+}} + X_{IC_{2_2^+ \rightarrow 2_1^+}} + X_{E0_{2_2^+ \rightarrow 2_1^+}}, \tag{6.1}$$

where X_{tot} is the total X-ray yield from Table 6.1, $X_{IC_{4_1^+ \rightarrow 2_1^+}}$ are the X-rays from the internal conversion of the $4_1^+ \rightarrow 2_1^+$ transition, $X_{IC_{2_2^+ \rightarrow 2_1^+}}$ the X-rays from the internal conversion of the $2_2^+ \rightarrow 2_1^+$ transition and $X_{E0_{2_2^+ \rightarrow 2_1^+}}$ are the X-rays due to an E0 component of the $2_2^+ \rightarrow 2_1^+$ transition. As the ratio of E2 to M1 components in the $2_2^+ \rightarrow 2_1^+$ transition is unknown a range of values for δ^2 have been used. For

Transitions in Coincidence with the $2_1^+ \rightarrow 0_1^+$ transition in ^{182}Hg		
Transition	Energy (keV)	Counts
K_α X-ray	68	78 ± 15
$2_2^+ \rightarrow 2_1^+$	196	23.3 ± 5.2
$4_1^+ \rightarrow 2_1^+$	262	62.9 ± 9.6

Table 6.1: Efficiency-corrected transitions observed in coincidence with the $2_1^+ \rightarrow 0_1^+$ transition in ^{182}Hg.

each value of δ^2 the X-rays from the internal conversion of the $2_2^+ \rightarrow 2_1^+$ transition have been calculated along with the X-rays from an E0 component of the same transition. The E0 component of the $2_2^+ \rightarrow 2_1^+$ transition has been inferred for each value of δ^2 using the relation

$$E0 = \frac{X_{E0_{2_2^+ \rightarrow 2_1^+}}}{X_{tot_{2_2^+ \rightarrow 2_1^+}} + \gamma_{2_2^+ \rightarrow 2_1^+}}, \tag{6.2}$$

where $X_{E0_{2_2^+ \rightarrow 2_1^+}}$ is the X-ray yield from the E0 component of the $2_2^+ \rightarrow 2_1^+$ transition, $X_{tot_{2_2^+ \rightarrow 2_1^+}}$ is the total X-ray yield of the $2_2^+ \rightarrow 2_1^+$ transition and $\gamma_{2_2^+ \rightarrow 2_1^+}$ is the γ-ray yield of the $2_2^+ \rightarrow 2_1^+$ transition. Table 6.2 lists for each δ^2 value used the percentage composition of the $2_2^+ \rightarrow 2_1^+$ transition.

^{182}Hg $2_2^+ \rightarrow 2_1^+$ Composition				
δ^2	E0 %	M1 %	E2 %	$\rho^2 \times 10^3$
∞	72.4 ± 20.8	0	27.6 ± 20.8	66 ± 28
9.0	70.5 ± 20.6	3.0 ± 2.1	26.6 ± 18.5	63 ± 27
4.0	68.7 ± 20.4	6.3 ± 4.1	25.1 ± 16.3	59 ± 25
2.3	66.9 ± 20.2	9.9 ± 6.1	23.2 ± 14.1	58 ± 25
1.5	65.1 ± 20.0	14.0 ± 8.0	21.0 ± 12.0	50 ± 21
1.0	63.2 ± 19.8	18.4 ± 9.9	18.4 ± 9.9	50 ± 21
0.66	61.4 ± 19.7	23.1 ± 11.8	15.4 ± 7.9	45 ± 19
0.43	59.6 ± 19.5	28.3 ± 13.7	12.1 ± 5.9	40 ± 17
0.25	57.8 ± 19.4	33.8 ± 15.5	8.4 ± 3.9	35 ± 16
0.11	56 ± 19.3	39.6 ± 17.3	4.4 ± 1.9	34 ± 15
0	53.9 ± 19.2	46.1 ± 19.2	0	33 ± 15

Table 6.2: Calculated composition of the $2_2^+ \rightarrow 2_1^+$ transition in ^{182}Hg using $\gamma\gamma$-coincidence X-ray and γ-ray yields. E0 branch is calculated from the E0 X-rays required to account for the observed X-ray yield in the $\gamma\gamma$-coincidence spectrum that do not originate from internal conversion. E2 and M1 branches are calculated from the assumed δ^2 values.

Values for ρ^2 have been calculated using the equation

$$\rho^2 = \left(\frac{1}{\Omega_k}\right) \cdot \left(\frac{1}{\tau_{E0}}\right), \tag{6.3}$$

where Ω_k is the electronic factor and τ_{E0} is the E0 lifetime of the 2_2^+ state. It can be seen from Table 6.2 that there is a strong E0 component to the $2_2^+ \rightarrow 2_1^+$ transition. This is indicative of mixing between the 2_1^+ and 2_2^+ states. From this analysis a lower limit for the E0 component of 53.9 ± 19.2% can be inferred. Values of ρ^2 are high, as is expected for a transition with a strong E0 component, but are in the same range as ρ^2 values for $0_2^+ \rightarrow 0_1^+$ transitions in ^{186}Hg and neighbouring nuclei [JZR$^+$94, WZCH99]. χ^2 minimizations were performed for each value of δ^2 listed in Table 6.2. Figure 6.5 shows the effect on the matrix elements associated to the 2_1^+ and 2_2^+ states that the value of δ^2 has. The *B(E2)*

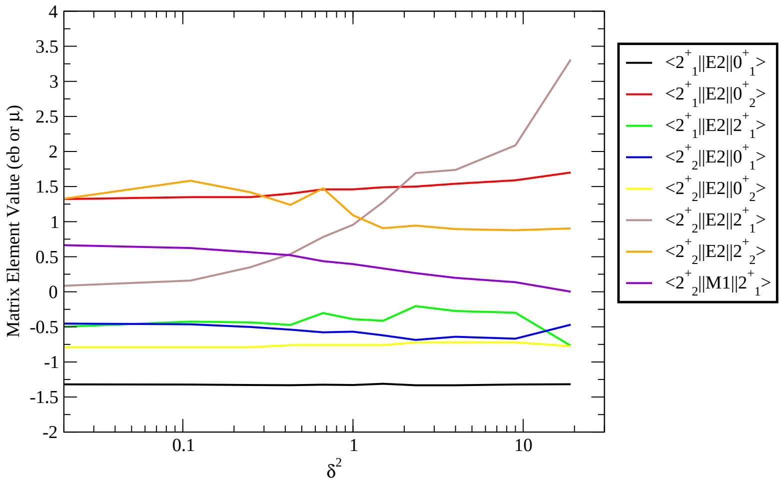

Figure 6.5: Resulting matrix elements from GOSIA χ^2 minimizations for values of δ^2 listed in Table 6.2.

value for the 2^+_1 state is not effected. This can be seen by the almost constant straight line. The diagonal matrix elements for both the 2^+_1 and 2^+_2 states are affected to some degree, though the effect is contained within the quoted errors for $\langle 2^+_1 \parallel E2 \parallel 2^+_1\rangle$ and $\langle 2^+_2 \parallel E2 \parallel 2^+_2\rangle$.

6.3 Summary

The nature of the light ^{182,186}Hg isotopes has been investigated for the first time using Coulomb excitation. In addition, RDDS lifetime measurements have been performed for ^{182}Hg. These two complementary methods have allowed the shape of the low-lying levels in these nuclei to be probed.

The magnitude and sign of the quadrupole moment for this state can be unambiguously assigned from the model independent approach undertaken. It is clear from both χ^2 minimizations and complementary shape analysis that the 2^+_1 state in ^{186}Hg has a *positive* quadrupole moment. It can be concluded from the Coulomb excitation data that in ^{186}Hg there is a clear dominant *oblate* component to the 2^+_1 state and its wavefunction. The large error bars on the diagonal matrix elements in particular show that the sensitivity to the Coulomb excitation cross section of the quadrupole moment was not as great as was hoped for.

In ^{182}Hg the lack of sensitivity to the quadrupole moment produced diagonal matrix elements again with large error bars. It can be concluded from the Coulomb excitation data alone that the 2_1^+ state in ^{182}Hg is a strong mixture of prolate and oblate structure. A relatively small quadrupole moment is a sign of strong mixing. This is supported by the conclusion that the $2_2^+ \rightarrow 2_1^+$ transition has a dominant E0 component. The negative sign of the quadrupole moment shows a *prolate* dominance of the wavefunction. RDDS lifetime measurements and band mixing calculations confirm this.

A transition from a dominant oblate component of the wavefunction of the 2_1^+ state to a prolate dominance of the wavefunction has been observed close to the neutron midshell. The 2_1^+ state in ^{186}Hg is clearly *oblate* in majority, and the 2_1^+ state in ^{182}Hg an admixture of prolate and oblate with a prolate dominance. This can be explained when considering level systematics; the prolate 2_1^+ intruder state finds its minimum at A = 180/182 and so will become the first excited 2_1^+ state in these isotopes.

The collective nature of the prolate band in the light Hg isotopes has been confirmed through the behaviour of the $|Q_t|$ values. The similarity to the light Pb isotopes confirms common behaviour in the region.

With the analysis of more accurate RDDS lifetime measurements of ^{184,186,188}Hg under way, new, improved *B(E2)* and $|Q_t|$ values for these nuclei will soon be available. The nature of collectivity and shape coexistence in the light Hg isotopes will further be investigated and the knowledge of this phenomena improved.

Bibliography

[ABD$^+$05] F. Ames, G. Bollen, P. Delahaye, O. Forstner, G. Huber, O. Kester, K. Reisinger, and P. Schmidt. *Nuclear Instruments and Methods in Physics Research Section A: Accelerators, Spectrometers, Detectors and Associated Equipment*, 538(1-3):17 – 32, 2005.

[ABH$^+$56] K. Alder, A. Bohr, T. Huus, B. Mottelson, and A. Winther. *Rev. Mod. Phys.*, 28(4):432–542, 1956.

[AHD$^+$00] A. N. Andreyev, M. Huyse, P. Van Duppen, L. Weissman, D. Ackermann, J. Gerl, F. P. Hessberger, S. Hoffmann, A. Kleinböhl, G. Münzenberg, S. Reshitko, C. Schlegel, H. Schaffner, P. Cagarda, M. Matos, S. Saro, A. Keenan, C. Moore, R. D. Page, M. Taylor, H. Kettunen, M. Leino, A. Lavrentiev, R. Wyss, and K. Heyde. *Nature*, 405:430 – 433, 2000.

[Ald75] K. Alder. *Electromagnetic excitation. Theory of Coulomb excitation with heavy ions.* North-Holland Publishing Company, Amsterdam, 1975.

[ALL$^+$76] G. Andersson, S. E. Larsson, G. Leander, P. Mller, S. G. Nilsson, I. Ragnarsson, S. berg, R. Bengtsson, J. Dudek, B. Nerlo-Pomorska, K. Pomorski, and Z. Szymanski. *Nuclear Physics A*, 268:205 – 256, 1976.

[Alv93] C. R. Alvarez. *Nuclear Physics News*, 3(3), 1993.

[AS64] K. Alder and R. M. Steffen. *Annual Review of Nuclear Science*, 14(1):403–482, 1964.

[AW66] K. Alder and W. Winther. *Coulomb Excitation.* Academic Press, New York, 1966.

[BBSD83] A. F. Barfield, B. R. Barrett, K. A. Sage, and P. D. Duval. *Z. Phys. A*, 311:205–215, 1983.

[BFF$^+$92] C. W. Beausang, S. A. Forbes, P. Fallon, P. J. Nolan, P. J. Twin, J. N. Mo, J. C. Lisle, M. A. Bentley, J. Simpson, F. A. Beck, D. Curien, G. deFrance, G. Duchne, and D. Popescu. *Nuclear Instruments and Methods in Physics Research Section A: Accelerators, Spectrometers, Detectors and Associated Equipment*, 313(1-2):37 – 49, 1992.

[BHB$^+$95] K. S. Bindra, P. F. Hua, B. R. S. Babu, C. Baktash, J. Barreto, D. M. Cullen, C. N. Davids, J. K. Deng, J. D. Garrett, M. L. Halbert, J. H. Hamilton, N. R. Johnson, A. Kirov, J. Kormicki, I. Y. Lee, W. C. Ma, F. K. McGowan, A. V. Ramayya, D. G. Sarantites, F. Soramel, and D. Winchell. *Phys. Rev. C*, 51(1):401–404, 1995.

[BHK$^+$72] J. Bonn, G. Huber, H. J. Kluge, L. Kugler, and E. W. Otten. *Physics Letters B*, 38(5):308 – 311, 1972.

[CAB$^+$04] J. Cederkall, F. Ames, P. A. Butler, P. Delahaye, V. Fedoseev, M. Lindroos, T. Nilsson, T. Sieber, F. Wenander, M. Pantea, S. Emhofer, D. Habs, O. Kester, K. Rudolph, R. von Hahn, O. Niedermaier, H. Scheit, D. Schwalm, P. van Duppen, M. Huyse, B. Jonsson, G. Nyman, J. Eberth, P. Reiter, and D. Weisshaar. *Nuclear Physics A*, 746:17 – 21, 2004.

[Cas90] Richard F. Casten. *Nuclear Structure from a Simple Perspective.* Oxford Science Publications, 1990.

[CCW83] T. Czosnyka, D. Cline, and C. Y. Wu. *Bull. Am. Phys. Soc.*, 28:745, 1983.

[Cli86] D. Cline. *Annual Review of Nuclear and Particle Science*, 36:383–716, 1986.

[DHvB89] A. Dewald, S. Harissopoulos, and P. von Brentano. *Z. Phys. A*, 334:163, 1989.

[DPS$^+$03] A. Dewald, R. Peusquens, B. Saha, P. von Brentano, A. Fitzler, T. Klug, I. Wiedenhöver, M. P. Carpenter, A. Heinz, R. V. F. Janssens, F. G. Kondev, C. J. Lister, D. Seweryniak, K. Abu Saleem, R. Krücken, J. R. Cooper, C. J. Barton, K. Zyromski, C. W. Beausang, Z. Wang, P. Petkov, A. M. Oros-Peusquens, U. Garg, and S. Zhu. *Phys. Rev. C*, 68(3):034314, 2003.

[Dra94] G. D. Dracoulis. *Phys. Rev. C*, 49(6):3324–3327, 1994.

[EKSB76] M. T. Esat, D. C. Kean, R. H. Spear, and A. M. Baxter. *Nuclear Physics A*, 274(1-2):237 – 252, 1976.

[FBH$^+$88] C. Fahlander, A. Bcklin, L. Hasselgren, A. Kavka, V. Mittal, L. E. Svensson, B. Varnestig, D. Cline, B. Kotlinski, H. Grein, E. Grosse, R. Kulessa, C. Michel, W. Spreng, H. J. Wollersheim, and J. Stachel. *Nuclear Physics A*, 485(2):327 – 359, 1988.

[Fel53] B.T. Feld. *Ann. Rev. Nuc. Sci*, 2:239, 1953.

[FP75] S. Frauendorf and V. V. Pashkkevich. *Physics Letters B*, 55(4):365 – 368, 1975.

[GDM$^+$06] T. Grahn, A. Dewald, O. Möller, R. Julin, C. W. Beausang, S. Christen, I. G. Darby, S. Eeckhaudt, P. T. Greenlees, A. Görgen, K. Helariutta, J. Jolie, P. Jones, S. Juutinen, H. Kettunen, T. Kröll, R. Krücken, Y. Le Coz, M. Leino, A. P. Leppänen, P. Maierbeck, D. A. Meyer, B. Melon, P. Nieminen, M. Nyman, R. D. Page, and J. Pakarinen. *Phys. Rev. Lett.*, 97(6):062501, 2006.

[GPS$^+$09] T. Grahn, A. Petts, M. Scheck, P. A. Butler, A. Dewald, M. B. Gómez Hornillos, P. T. Greenlees, A. Görgen, K. Helariutta, J. Jolie, P. Jones, R. Julin, S. Juutinen, S. Ketelhut, R. Krücken, T. Kröll, M. Leino, J. Ljungvall, P. Maierbeck, B. Melon, M. Nyman, R. D. Page, Th. Pissulla, P. Rahkila, J. Sarén, C. Scholey, and

A. Semchenkov. *Phys. Rev. C*, 80(1):014324, 2009.

[GYL+88] A. Ghiorso, S. Yashita, M. E. Leino, L. Frank, J. Kalnins, P. Armbruster, J. P. Dufour, and P. K. Lemmertz. *Nuclear Instruments and Methods in Physics Research Section A: Accelerators, Spectrometers, Detectors and Associated Equipment*, 269(1):192 – 201, 1988.

[HAMD71] O. Husser, T. K. Alexander, A. B. McDonald, and W. T. Diamond. *Nuclear Physics A*, 175(3):593 – 605, 1971.

[HJS49] Otto Haxel, J. Hans D. Jensen, and Hans E. Suess. *Phys. Rev.* , 75(11):1766, 1949.

[HKS+98] D. Habs, O. Kester, T. Sieber, A. Kolbe, J. Ott, G. Bollen, F. Ames, D. Schwalm, R. von Hahn, R. Repnow, H. Podlech, A. Schempp, U. Ratzinger, L. Liljeby, K. G. Rensfelt, F. Wenander, B. Jonsson, G. Nyman, P. Van Duppen, M. Huyse, A. Richter, G. Shrieder, G. Walter, and REX-ISOLDE collaboration. *Nuclear Instruments and Methods in Physics Research Section B: Beam Interactions with Materials and Atoms*, 139(1-4):128 – 135, 1998.

[JHM01] R. Julin, K. Helariutta, and M. Muikku. *Journal of Physics G: Nuclear and Particle Physics*, 27(7):R109–R139, 2001.

[JKB78] N. G. Jonsson, J. Kantele, and A. Backlin. *Nuclear Instrumentation and Methods*, 152:485, 1978.

[JZR+94] P. K. Joshi, E. F. Zganjar, D. Rupnik, S. J. Robinson, P. F. Mantica, H. K. Carter, J. Kormicki, R. L. Gill, W. B. Walters, C. R. Bingham, A. V. Ramayya, W. C. Ma, and J. H. Hamilton. *International Journal of Modern Physics E*, 3(2):757 – 767, 1994.

[KN29] O. Klein and Y. Nishina. *Z. Phys*, 52:853, 1929.

[Kno00] Glen F. Knoll. *Radiation Detection and Measurement.* John Wiley & Sons, 2000.

[Kra88] Keneth S. Krane. *Introductory Nuclear Physics.* John Wiley & Sons, 1988.

[KSE$^+$03] O. Kester, T. Sieber, S. Emhofer, F. Ames, K. Reisinger, P. Reiter, P. G. Thirolf, R. Lutter, D. Habs, B. H. Wolf, G. Huber, P. Schmidt, A. N. Ostrowski, R. von Hahn, R. Repnow, J. Fitting, M. Lauer, H. Scheit, D. Schwalm, H. Podlech, A. Schempp, U. Ratzinger, O. Forstner, F. Wenander, J. Cederkll, T. Nilsson, M. Lindroos, H. Fynbo, S. Franchoo, U. Bergmann, M. Oinonen, J. yst, P. Van Den Bergh, P. Van Duppen, M. Huyse, N. Warr, D. Weisshaar, J. Eberth, B. Jonson, G. Nyman, M. Pantea, H. Simon, G. Shrieder, A. Richter, O. Tengblad, T. Davinson, P. J. Woods, G. Bollen, L. Weissmann, L. Liljeby, and K. G. Rensfelt. *Nuclear Instruments and Methods in Physics Research Section B: Beam Interactions with Materials and Atoms*, 204:20 – 30, 2003.

[LAB$^+$01] I. H. Lazarus, D. E. Applebe, A. J. Boston, P. J. Coleman-Smith, J. R. Cresswell, M. Descovich, S. A. A. Lauer, J. Norman, C. J. Pearson, V. F. E. Pucknell, J. A. Sampson, G. Turk, and J. J. Valiente-Dobon. *IEEE Trans. Nucl. Sci.*, 48:567, 2001.

[LÄE$^+$95] M. Leino, J. Äystö, T. Enqvist, P. Heikkinen, A. Jokinen, M. Nurmia, A. Ostrowski, W. H. Trzaska, J. Uusitalo, K. Eskola, P. Armbruster, and V. Ninov. *Nucl. Instrum. Methods B*, 99:635, 1995.

[LBC69] H. F. Lutz, W. Bartolini, and T. H. Curtis. *Phys. Rev.*, 178(4):1911–1918, 1969.

[LC88] G. A. Leander and Y. S. Chen. *Phys. Rev. C*, 37(6):2744–2778, 1988.

[Lei97] M. Leino. *Nuclear Instruments and Methods in Physics Research Section B: Beam Interactions with Materials and Atoms*, 126(1-4):320 – 328, 1997.

[May49] M. G. Mayer. *Phys. Rev.*, 75(12):1969–1970, 1949.

[MMS$^+$69] W. T. Milner, F. K. McGowan, P. H. Stelson, R. L. Robinson, and R. O. Sayer. *Nuclear Physics A*, 129(3):687 – 696, 1969.

[MPC+77] M. Maynard, D. C. Palmer, J. R. Cresswell, P. D. Forsyth, I. Hall, and D. G. E. Martin. *Journal of Physics G*, 3(12):1735, 1977.

[MRH+86] W. C. Ma, A. V. Ramayya, J. H. Hamilton, S. J. Robinson, J. D. Cole, E. F. Zganjar, E. H. Spejewski, R. Bengtsson, W. Nazarewicz, and J.-Y. Zhang. *Physics Letters*, 167B(3):277–282, 1986.

[MRSF65] F. K. McGowan, R. L. Robinson, P. H. Stelson, and J. L. C. Ford. *Nuclear Physics*, 66(1):97 – 118, 1965.

[Naz93] W. Nazarewicz. *Phys. Lett. B*, 305:195, 1993.

[Nil55] S G Nilsson. *K. Dan. Vidensk. Selsk. Mat. Fys. Medd.*, 29(16), 1955.

[OCD+02] A. N. Ostrowski, S. Cherubini, T. Davinson, D. Groombridge, A. M. Laird, A. Musumarra, A. Ninane, A. di Pietro, A. C. Shotter, and P. J. Woods. *Nuclear Instruments and Methods in Physics Research Section A: Accelerators, Spectrometers, Detectors and Associated Equipment*, 480(2-3):448 – 455, 2002.

[PAA+03] R. D. Page, A. N. Andreyev, D. E. Appelbe, P. A. Butler, S. J. Freeman, P. T. Greenlees, R. D. Herzberg, D. G. Jenkins, G. D. Jones, P. Jones, D. T. Joss, R. Julin, H. Kettunen, M. Leino, P. Rahkila, P. H. Regan, J. Simpson, J. Uusitalo, S. M. Vincent, and R. Wadsworth. *Nucl. Instrum. Methods B.*, 204:634, 2003.

[Pau] E. Paul. *Nuclear Models.* Private communication.

[PDS73] D. Proetel, R. M. Diamond, and F. S Stephens. *Physics Letters*, 48B(2):102–104, 1973.

[PHD+92] P. Petkov, S. Harissopoulos, A. Dewald, M. Stolzenwald, G. Bôhm, P. Sala, K. Schiffer, A. Gelberg, K. O. Zell, and P. von Brentano. *Nucl. Phys. A*, 543:589, 1992.

[Rad95] D. C. Radford. *Nuclear Instruments and Methods in Physics Research Section A: Accelerators, Spectrometers, Detectors and Associated Equipment*, 361(1-2):297 – 305, 1995.

[Rah07] R. Rahkila, 2007. arXiv:0711.336v1 [nucl-ex].

[RBB+97] J. D. Richards, T. Berggren, C. R. Bingham, W. Nazarewicz, and J. Wauters. *Phys. Rev. C*, 56(3):1389–1397, 1997.

[Rea] Paddy Reagan. *Postgraduate Nuclear Physics Experimental Techniques.* Private communication.

[Rex] *ISOLDE Website.* http://isolde.web.cern.ch.

[RFAP78] F. Rösel, H. M. Fries, K. Alder, and H. C. Pauli. *At. Data Nucl. Data Tables*, 21:91, 1978.

[RKS+99] R. Rao, O. Kester, T. Sieber, D. Habs, and K. Rudolph. *Nuclear Instruments and Methods in Physics Research Section A: Accelerators, Spectrometers, Detectors and Associated Equipment*, 427(1-2):170 – 176, 1999.

[SAB+02] P. Schmidt, F. Ames, G. Bollen, O. Forstner, G. Huber, M. Oinonen, and J. Zimmer. *Nuclear Physics A*, 701(1-4):550 – 556, 2002.

[Sch02] C.L. Scholey. *A Spectroscopic Study of Doubly-Odd N=77 Isotones near the Proton Dripline Utilising the Recoil-Isomer Tagging Technique.* 2002. PhD Thesis.

[SGbuC+09] M. Sandzelius, E. Ganioğlu, B. Cederwall, B. Hadinia, K. Andgren, T. Bäck, T. Grahn, P. Greenlees, U. Jakobsson, A. Johnson, P. M. Jones, R. Julin, S. Juutinen, S. Ketelhut, A. Khaplanov, M. Leino, M. Nyman, P. Peura, P. Rahkila, J. Sarén, C. Scholey, J. Uusitalo, and R. Wyss. *Phys. Rev. C*, 79(6):064315, 2009.

[STSH85] K. P. Singh, D. C. Tayal, G. Singh, and H. S. Hans. *Phys. Rev. C*, 31(1):79–86, 1985.

[SW68] A. Z. Schwarzschild and E. K. Warburton. *Annual Review of Nuclear Science*, 18(1):265–290, 1968.

[SZF02] B. Singh, R. Zywina, and R. B. Firestone. *Nuclear Data Sheets*, 97(2):241 – 592, 2002.

[UBD+86] G. Ulm, S. K. Bhattacherjee, P. Dabkiewicz, G. Huber, H. J. Kluge, T. Kühl, H. Lochmann, E. W. Otten, K. Wendt, S. A. Ahmad, W. Klempt, R. Neugart, and ISOLDE Collaboration. *Z. Phys. A*, 325(3):247 – 259, 1986.

[WBD+94] J. Wauters, N. Bijnens, P. Dendooven, M. Huyse, Han Yull Hwang, G. Reusen, J. von Schwarzenberg, P. Van Duppen, R. Kirchner, and E. Roeckl. *Phys. Rev. Lett.*, 72(9):1329–1332, 1994.

[WCF+03] B. H. Wolf, J. Cederkll, O. Forstner, F. Wenander, F. Ames, K. Reisinger, L. Liljeby, . Skeppstedt, B. Jonson, and G. Nyman. *Nuclear Instruments and Methods in Physics Research Section B: Beam Interactions with Materials and Atoms*, 204:428 – 432, 2003.

[Wei35] C. F. V. Weizsäcker. *Zeitschrift fur Physik*, 96:431–458, 1935.

[Wen02] F. Wenander. *Nuclear Physics A*, 701(1-4):528 – 536, 2002.

[WHN+92] J. L. Wood, K. Heyde, W. Nazarewicz, M. Huyse, and P. van Duppen. *Physics Reports*, 215(3-4):101 – 201, 1992.

[WZCH99] J. L. Wood, E. F. Zganjar, C. De Coster, and K. Heyde. *Nuclear Physics A*, 651(4):323 – 368, 1999.

Appendix A

Tabulated Recoil Distance Doppler-Shift Measurements of ^{182}Hg

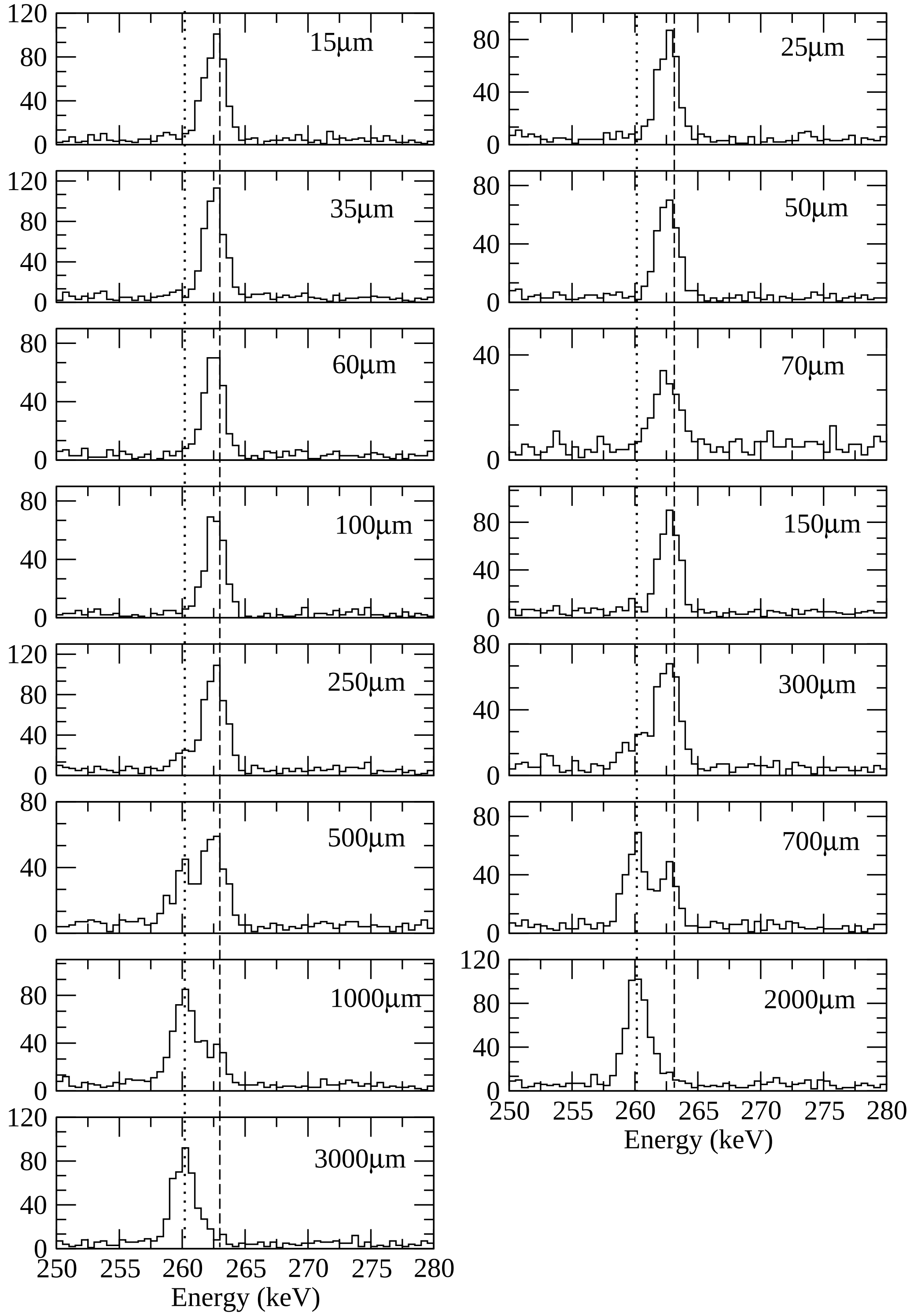

Figure A.1: Spectra showing the deconvolution of the fully Doppler shifted and degraded components of the 261.4 keV $4^+ \rightarrow 2^+$ transition, gated on the populating 333.1 keV $6^+ \rightarrow 4^+$ transition when using Ring 1 of JUROGAM. Target-to-degrader distances are listed in each panel, dashed lines indicate the degraded component whilst dotted lines indicate the fully Doppler shifted component of the transition.

261.4 keV $4^+ \rightarrow 2^+$ Transition JUROGAM Ring 1		
Distance d (μm)	Counts I_s	Counts I_d
15	5±7	393±21
25	5±6	317±19
35	7±6	429±22
50	7±5	287±18
60	8±6	274±17
70	16±8	375±20
100	18±8	224±16
150	20±7	317±19
250	62±12	417±22
300	76±12	285±19
500	148±15	232±17
700	234±18	137±15
1000	340±20	120±14
2000	432±22	35±10
3000	372±20	24±9

Table A.1: Summary of measurements of different target-to-degrader distances for the 261.4 keV $4^+ \rightarrow 2^+$ transition for RDDS measurements of ^{182}Hg. The fully Doppler shifted components, I_s and degraded components, I_d are measured with 5 JUROGAM detectors at 157.6°.

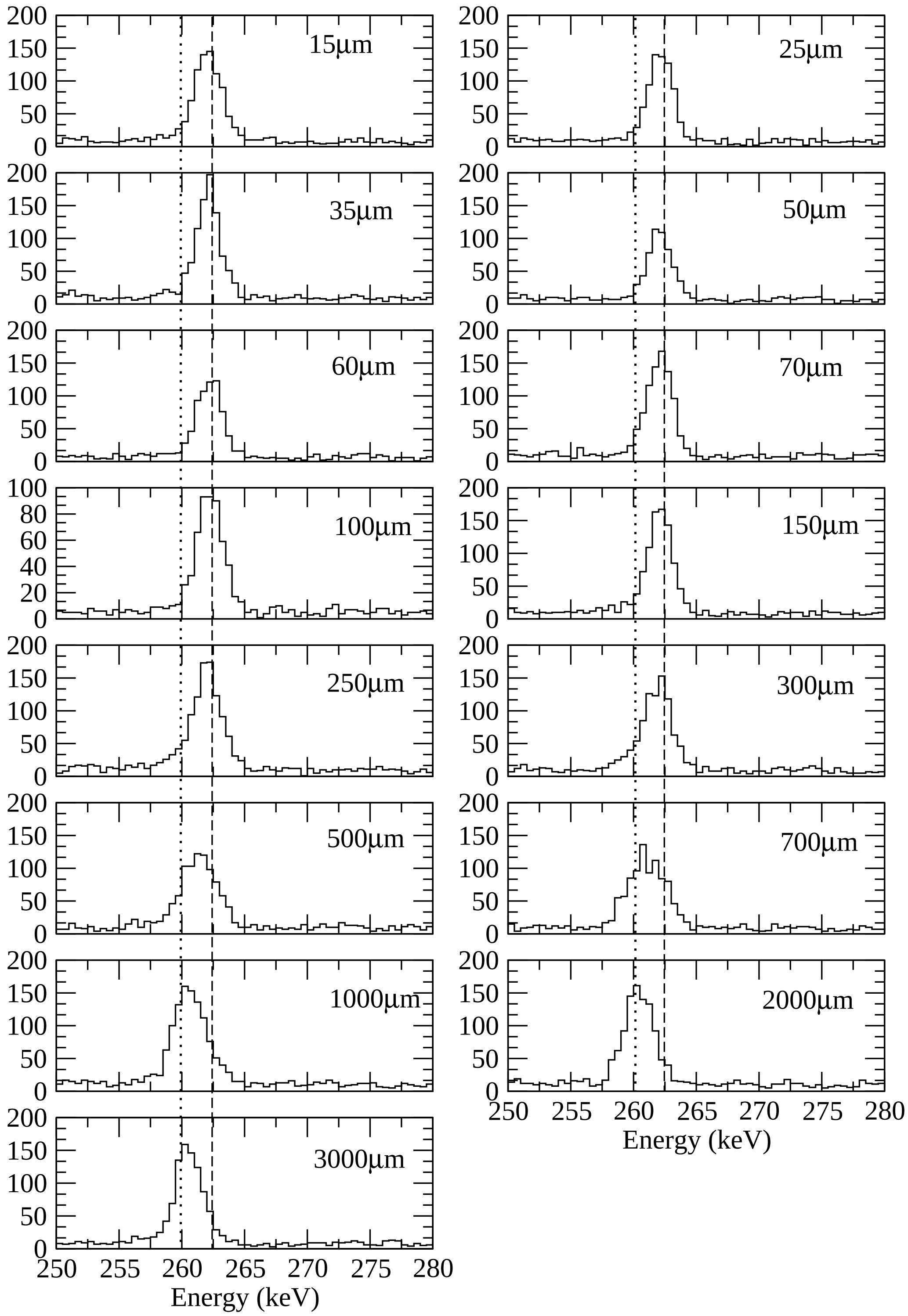

Figure A.2: Spectra showing the deconvolution of the fully Doppler shifted and degraded components of the 261.4 keV $4^+ \rightarrow 2^+$ transition, gated on the populating 333.1 keV $6^+ \rightarrow 4^+$ transition when using Ring 2 of JUROGAM. Target-to-degrader distances are listed in each panel, dashed lines indicate the degraded component whilst dotted lines indicate the fully Doppler shifted component of the transition.

261.4 keV $4^+ \rightarrow 2^+$ Transition JUROGAM Ring 2		
Distance d (μm)	Counts I_s	Counts I_d
15	9±7	719±33
25	7±6	687±31
35	10±8	779±30
50	4±5	536±27
60	6±7	629±30
70	7±6	772±33
100	5±7	490±27
150	11±9	781±34
250	114±24	786±36
300	146±24	639±32
500	354±28	443±29
700	458±30	333±28
1000	772±35	208±27
2000	809±34	52±21
3000	745±33	68±21

Table A.2: Summary of measurements of different target-to-degrader distances for the 261.4 keV $4^+ \rightarrow 2^+$ transition for RDDS measurements of ^{182}Hg. The fully Doppler shifted components, I_s and degraded components, I_d are measured with 10 JUROGAM detectors at 134.8°.

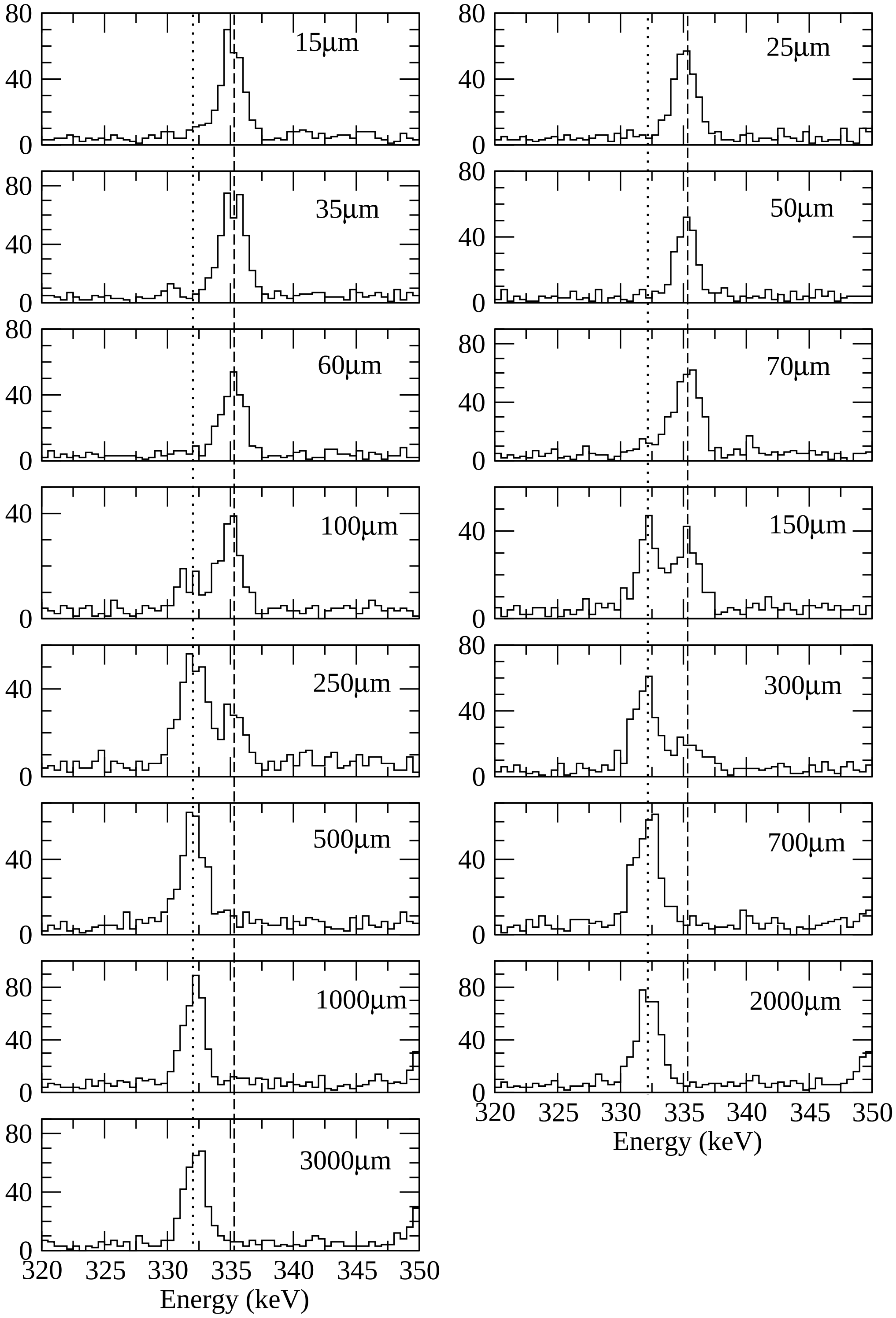

Figure A.3: Spectra showing the deconvolution of the fully Doppler shifted and degraded components of the 333.1 keV $6^+ \rightarrow 4^+$ transition, gated on the populating 414 keV $8^+ \rightarrow 6^+$ transition when using Ring 1 of JUROGAM. Target-to-degrader distances are listed in each panel, dashed lines indicate the degraded component whilst dotted lines indicate the fully Doppler shifted component of the transition.

333.1 keV $6^+ \rightarrow 4^+$ Transition JUROGAM Ring 1		
Distance d (μm)	Counts I_s	Counts I_d
15	3±7	269±17
25	5±7	248±17
35	2±6	325±19
50	7±5	197±15
60	8±5	208±15
70	43±9	285±18
100	48±9	138±13
150	148±14	145±14
250	238±17	107±13
300	227±16	79±11
500	257±17	16±6
700	278±18	16±6
1000	316±19	10±8
2000	328±19	5±6
3000	278±18	4±6

Table A.3: Summary of measurements of different target-to-degrader distances for the 333.1 keV $6^+ \rightarrow 4^+$ transition for RDDS measurements of ^{182}Hg. The fully Doppler shifted components, I_s and degraded components, I_d are measured with 5 JUROGAM detectors at 157.6°.

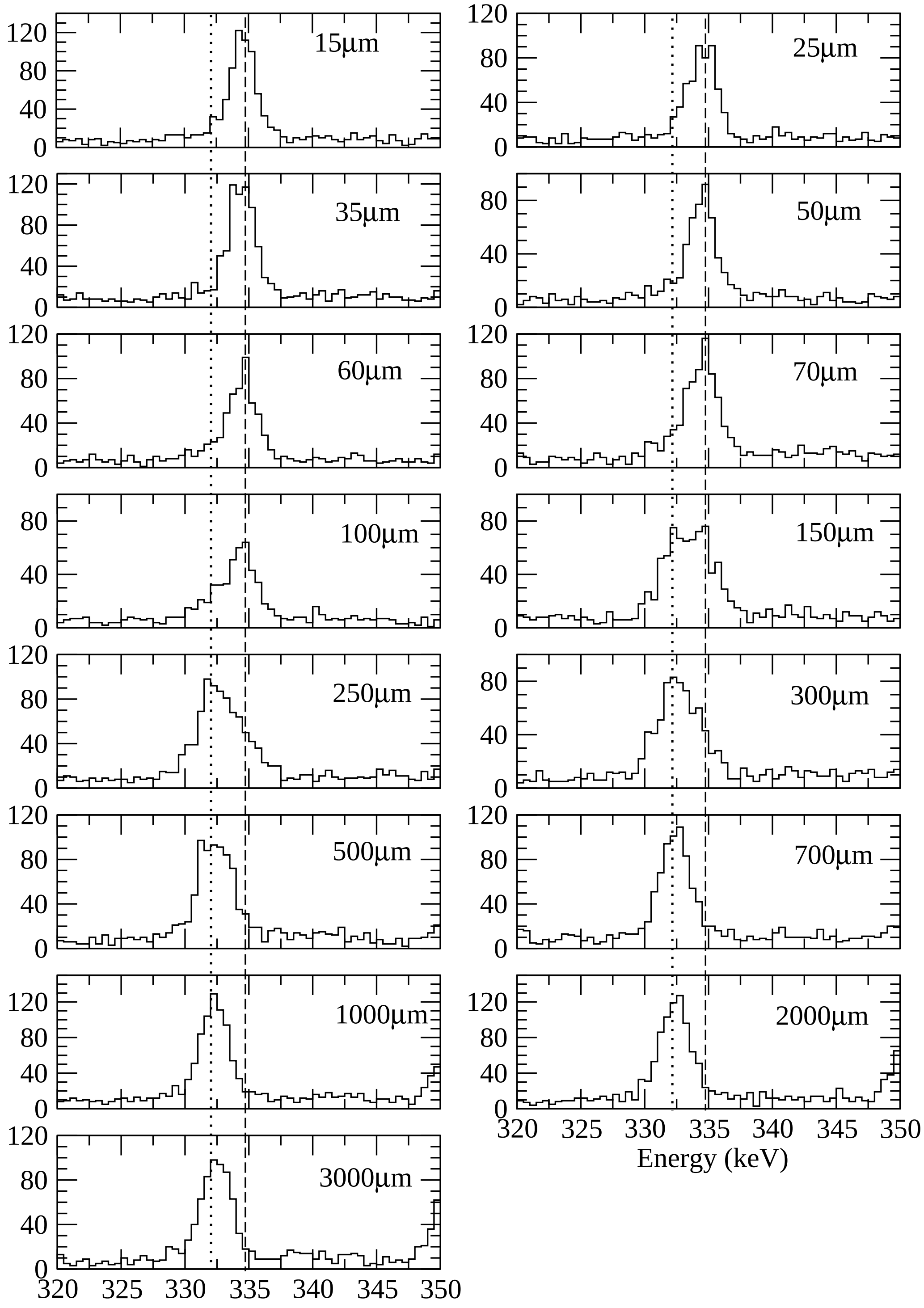

Figure A.4: Spectra showing the deconvolution of the fully Doppler shifted and degraded components of the 333.1 keV $6^+ \rightarrow 4^+$ transition, gated on the populating 414 keV $8^+ \rightarrow 6^+$ transition when using Ring 2 of JUROGAM. Target-to-degrader distances are listed in each panel, dashed lines indicate the degraded component whilst dotted lines indicate the fully Doppler shifted component of the transition.

333.1 keV $6^+ \rightarrow 4^+$ Transition JUROGAM Ring 2		
Distance d (μm)	Counts I_s	Counts I_d
15	34±16	524±26
25	40±15	407±23
35	46±16	540±27
50	67±15	374±23
60	87±16	364±23
70	112±19	451±26
100	130±17	248±20
150	339±25	235±22
250	520±29	125±21
300	470±27	84±18
500	601±29	7±16
700	595±29	2±15
1000	664±31	1±12
2000	690±32	1±11
3000	575±28	2±12

Table A.4: Summary of measurements of different target-to-degrader distances for the 333.1 keV $6^+ \rightarrow 4^+$ transition for RDDS measurements of ^{182}Hg. The fully Doppler shifted components, I_s and degraded components, I_d are measured with 10 JUROGAM detectors at 134.8°.

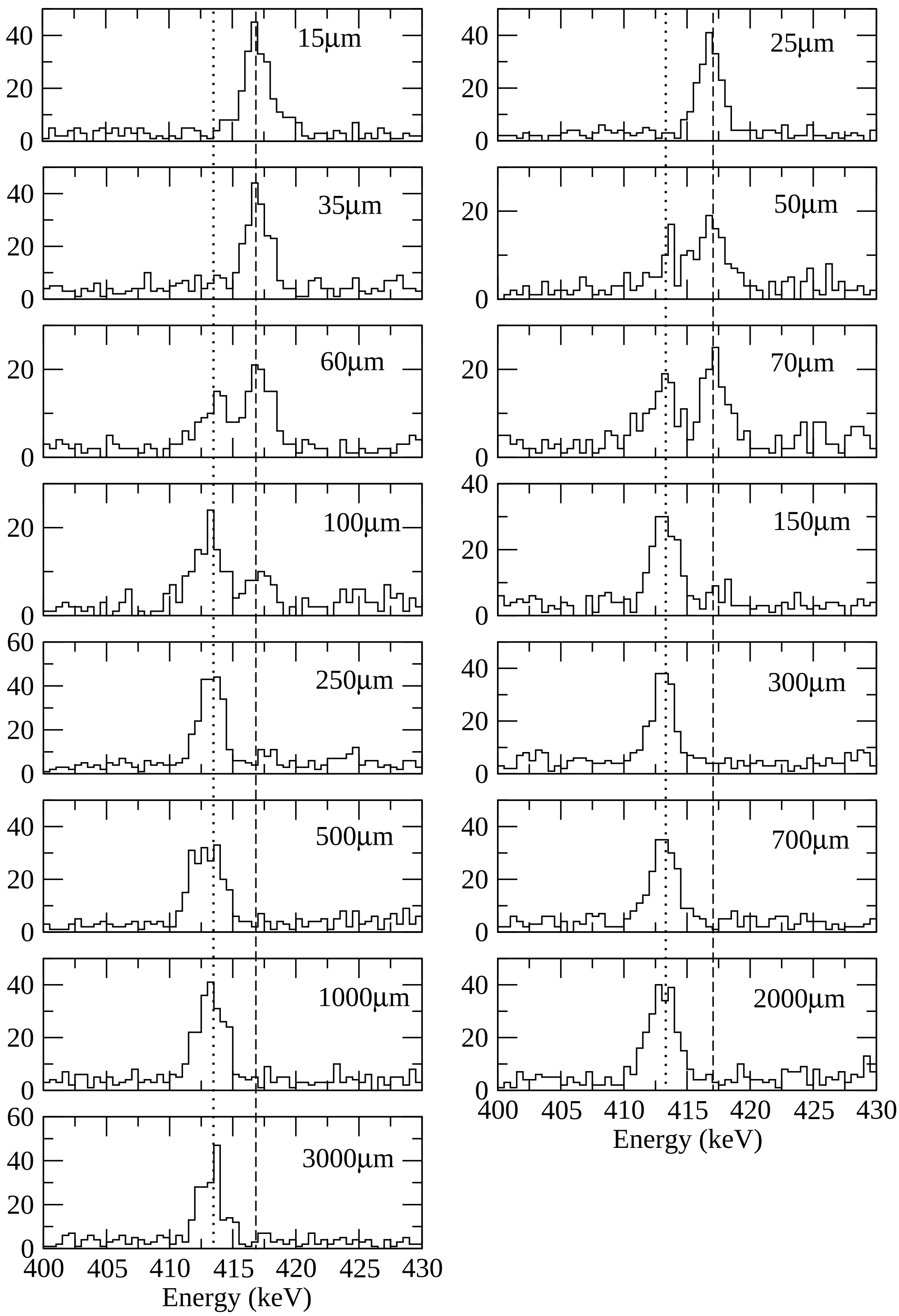

Figure A.5: Spectra showing the deconvolution of the fully Doppler shifted and degraded components of the 414.0 keV $8^+ \rightarrow 6^+$ transition, gated on the populating 487.4 keV $10^+ \rightarrow 8^+$ transition when using Ring 1 of JUROGAM. Target-to-degrader distances are listed in each panel, dashed lines indicate the degraded component whilst dotted lines indicate the fully Doppler shifted component of the transition.

414.0 keV $8^+ \rightarrow 6^+$ Transition JUROGAM Ring 1		
Distance d (μm)	Counts I_s	Counts I_d
15	1±4	190±15
25	1±4	153±13
35	15±6	165±14
50	30±7	90±11
60	48±8	98±11
70	67±10	93±11
100	86±10	31±7
150	142±13	17.7±6.1
250	201±15	22±7
300	156±13	11±6
499	157±13	6±6
700	165±14	2±4
1000	179±14	2±5
2000	184±14	1±6
3000	153±13	1±5

Table A.5: Summary of measurements of different target-to-degrader distances for the 414.0 keV $8^+ \rightarrow 6^+$ transition for RDDS measurements of ^{182}Hg. The fully Doppler shifted components, I_s and degraded components, I_d are measured with 5 JUROGAM detectors at 157.6°.

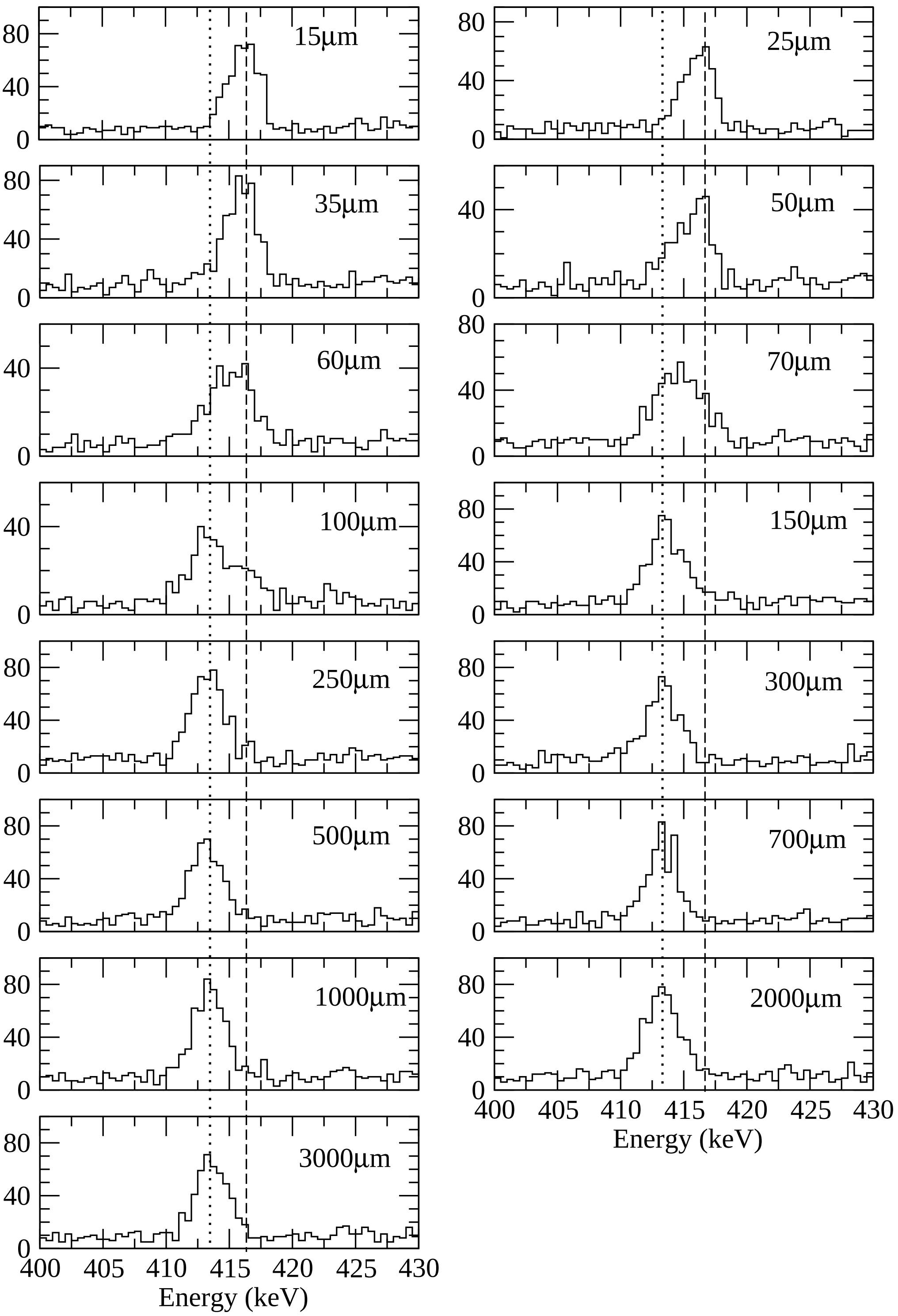

Figure A.6: Spectra showing the deconvolution of the fully Doppler shifted and degraded components of the 414.0 keV $8^+ \rightarrow 6^+$ transition, gated on the populating 487.4 keV $10^+ \rightarrow 8^+$ transition when using Ring 2 of JUROGAM. Target-to-degrader distances are listed in each panel, dashed lines indicate the degraded component whilst dotted lines indicate the fully Doppler shifted component of the transition.

414.0 keV $8^+ \rightarrow 6^+$ Transition JUROGAM Ring 2		
Distance d (μm)	Counts I_s	Counts I_d
15	49±12	319±20
25	71±12	266±18
35	108±15	301±20
50	107±13	145±15
60	155±15	114±14
70	269±20	117±15
100	205±17	62±12
150	387±22	32±12
250	397±23	12±7
300	357±22	7±8
500	351±21	3±5
700	341±21	1±5
1000	424±24	1±6
2000	409±23	1±6
3000	386±22	0±8

Table A.6: Summary of measurements of different target-to-degrader distances for the 414.0 keV $8^+ \rightarrow 6^+$ transition for RDDS measurements of ^{182}Hg. The fully Doppler shifted components, I_s and degraded components, I_d are measured with 10 JUROGAM detectors at 134.8°.

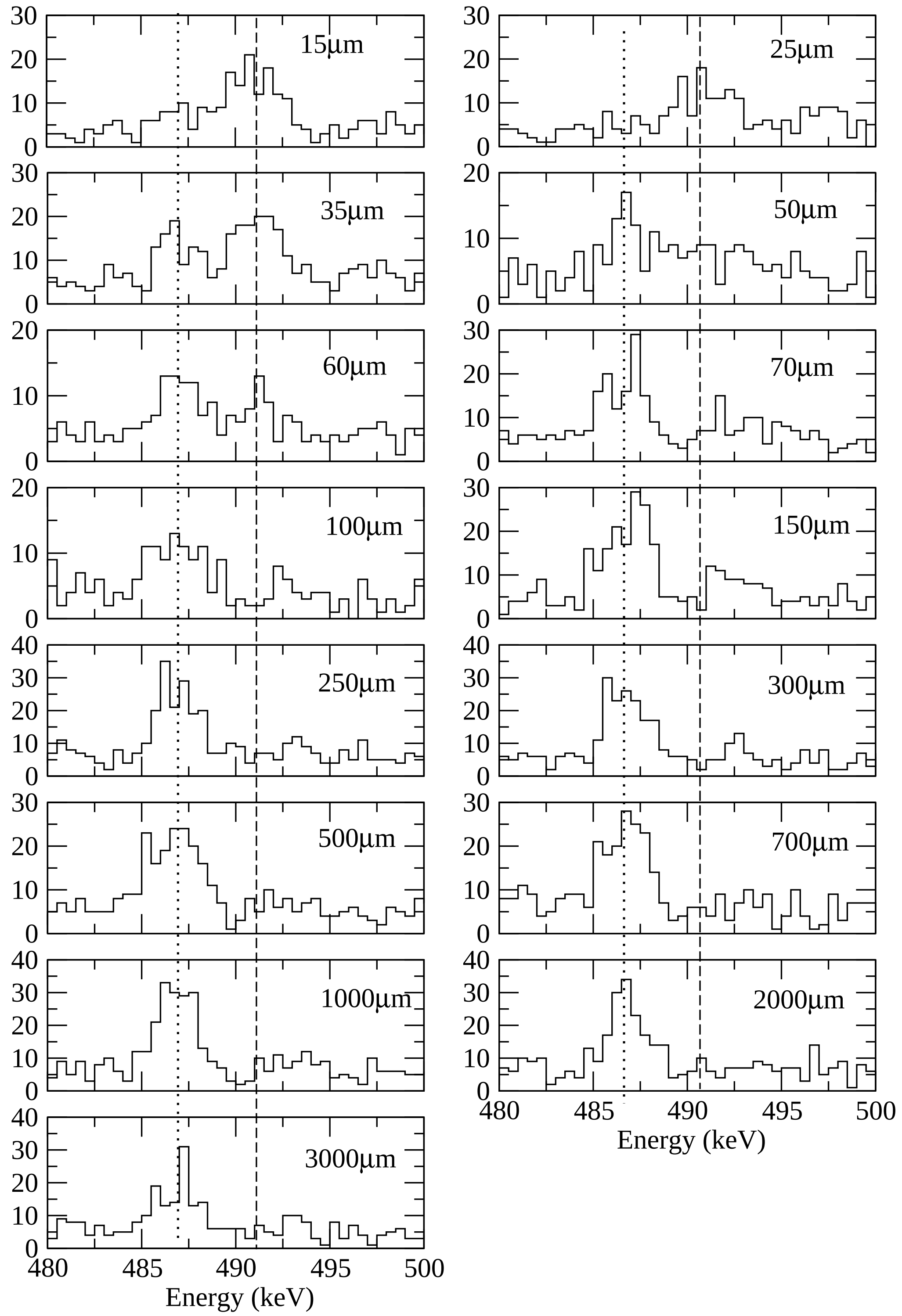

Figure A.7: Spectra showing the deconvolution of the fully Doppler shifted and degraded components of the 487.4 keV $10^+ \rightarrow 8^+$ transition, gated on the populating 553.1 keV $12^+ \rightarrow 10^+$ transition when using Ring 1 of JUROGAM. Target-to-degrader distances are listed in each panel, dashed lines indicate the degraded component whilst dotted lines indicate the fully Doppler shifted component of the transition.

487.4 keV $10^+ \rightarrow 8^+$ Transition JUROGAM Ring 1		
Distance d (μm)	Counts I_s	Counts I_d
15	6±8	84±11
25	15±6	66±10
35	49±10	105±12
50	51±9	36±8
60	62±10	35±8
70	94±11	21±7
100	66±10	5±5
150	118±13	10±7
250	129±13	16±8
300	133±13	9±6
500	129±13	5±6
700	126±13	5±7
1000	154±14	2±6
2000	132±13	1±8
3000	93±11	0±9

Table A.7: Summary of measurements of different target-to-degrader distances for the 487.4 keV $10^+ \rightarrow 8^+$ transition for RDDS measurements of ^{182}Hg. The fully Doppler shifted components, I_s and degraded components, I_d are measured with 5 JUROGAM detectors at 157.6°.

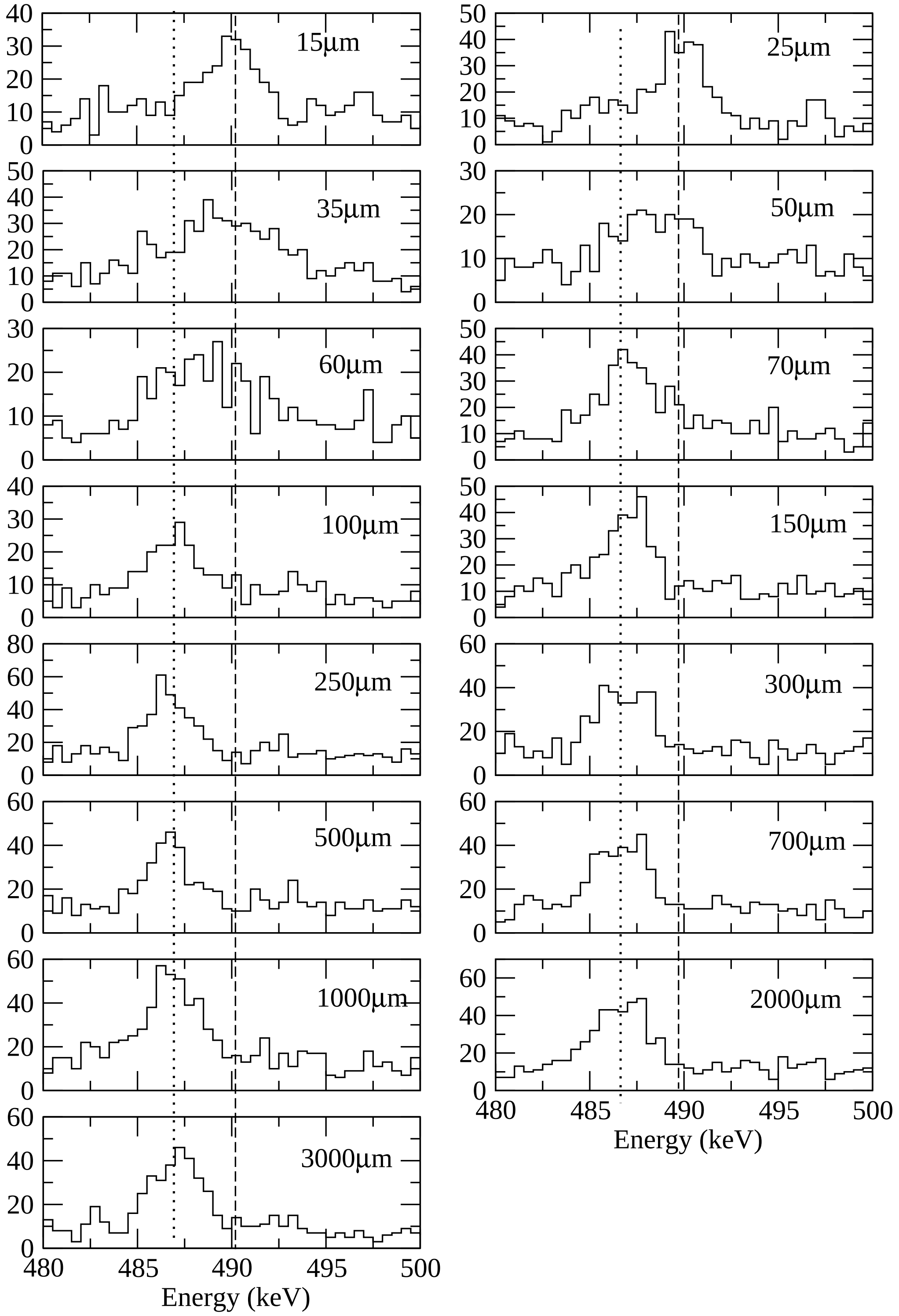

Figure A.8: Spectra showing the deconvolution of the fully Doppler shifted and degraded components of the 487.4 keV $10^+ \rightarrow 8^+$ transition, gated on the populating 553.1 keV $12^+ \rightarrow 10^+$ transition when using Ring 2 of JUROGAM. Target-to-degrader distances are listed in each panel, dashed lines indicate the degraded component whilst dotted lines indicate the fully Doppler shifted component of the transition.

487.4 keV $10^+ \rightarrow 8^+$ Transition JUROGAM Ring 2		
Distance d (μm)	Counts I_s	Counts I_d
15	28±11	130±15
25	58±12	162±16
35	99±14	147±15
50	93±12	68±11
60	94±13	44±11
70	190±17	36±11
100	134±14	15±8
150	195±17	6±10
250	236±19	7±7
300	209±17	7±7
500	187±17	2±5
700	215±18	3±7
1000	275±20	2±6
2000	231±19	1±7
3000	230±18	0±8

Table A.8: Summary of measurements of different target-to-degrader distances for the 487.4 keV $10^+ \rightarrow 8^+$ transition for RDDS measurements of ^{182}Hg. The fully Doppler shifted components, I_s and degraded components, I_d are measured with 10 JUROGAM detectors at 134.8°.

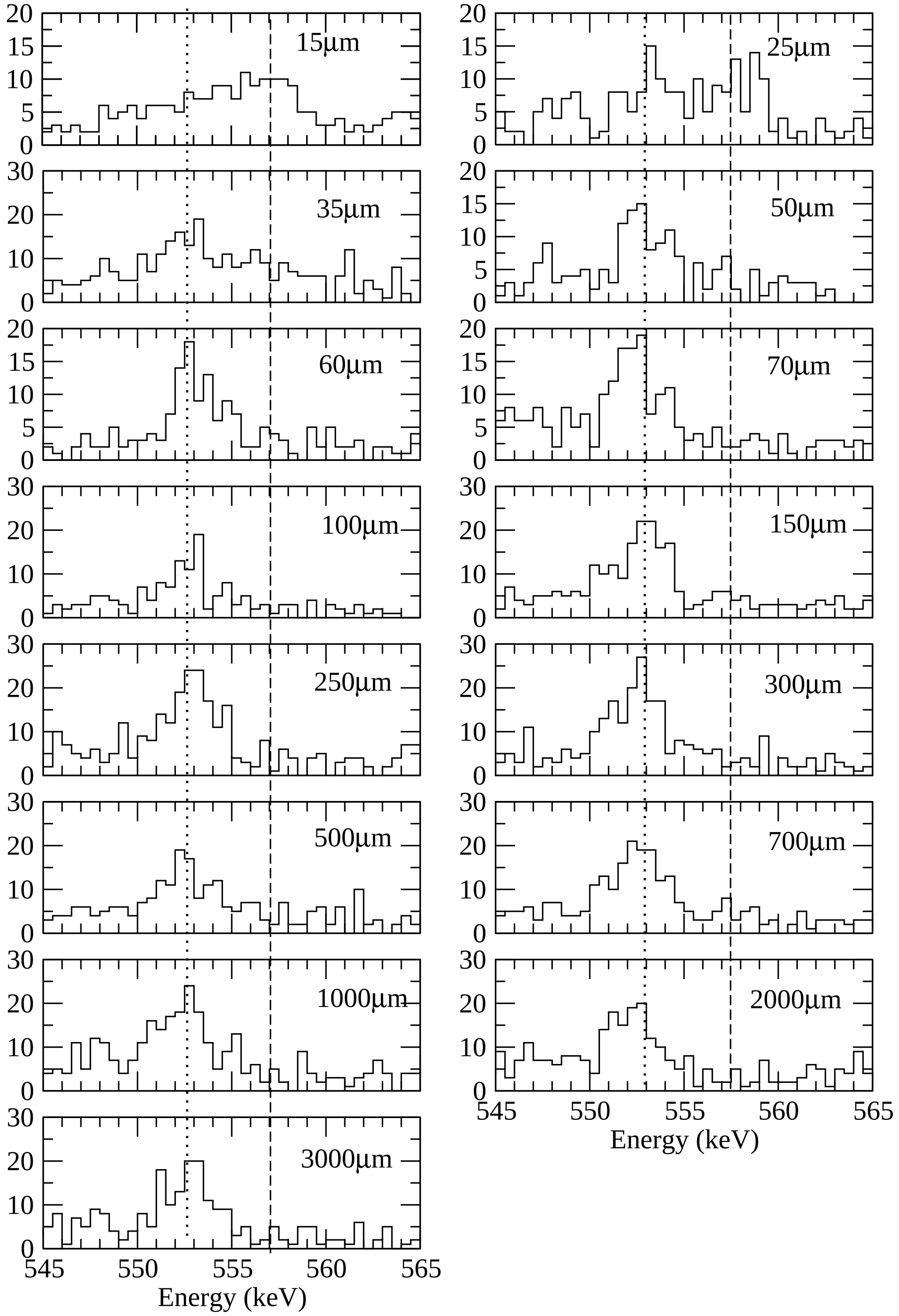

Figure A.9: Spectra showing the deconvolution of the fully Doppler shifted and degraded components of the 553.1 keV $12^+ \rightarrow 10^+$ transition, gated on the populating 611.3 keV $14^+ \rightarrow 12^+$ transition when using Ring 1 of JUROGAM. Target-to-degrader distances are listed in each panel, dashed lines indicate the degraded component whilst dotted lines indicate the fully Doppler shifted component of the transition.

553.1 keV $12^+ \rightarrow 10^+$ Transition JUROGAM Ring 1		
Distance d (μm)	Counts I_s	Counts I_d
15	36±8	62±10
25	40±9	43±8
35	94±11	39±9
50	47±7	2±2
60	74±9	1±2
70	81±11	2±6
100	54±8	1±4
150	111±12	3±6
250	143±13	0±4
300	121±12	0±6
500	87±11	1±7
700	119±12	1±7
1000	122±12	0±4
2000	96±11	0±5
3000	101±11	0±5

Table A.9: Summary of measurements of different target-to-degrader distances for the 553.1 keV $12^+ \rightarrow 10^+$ transition for RDDS measurements of ^{182}Hg. The fully Doppler shifted components, I_s and degraded components, I_d are measured with 5 JUROGAM detectors at 157.6°.

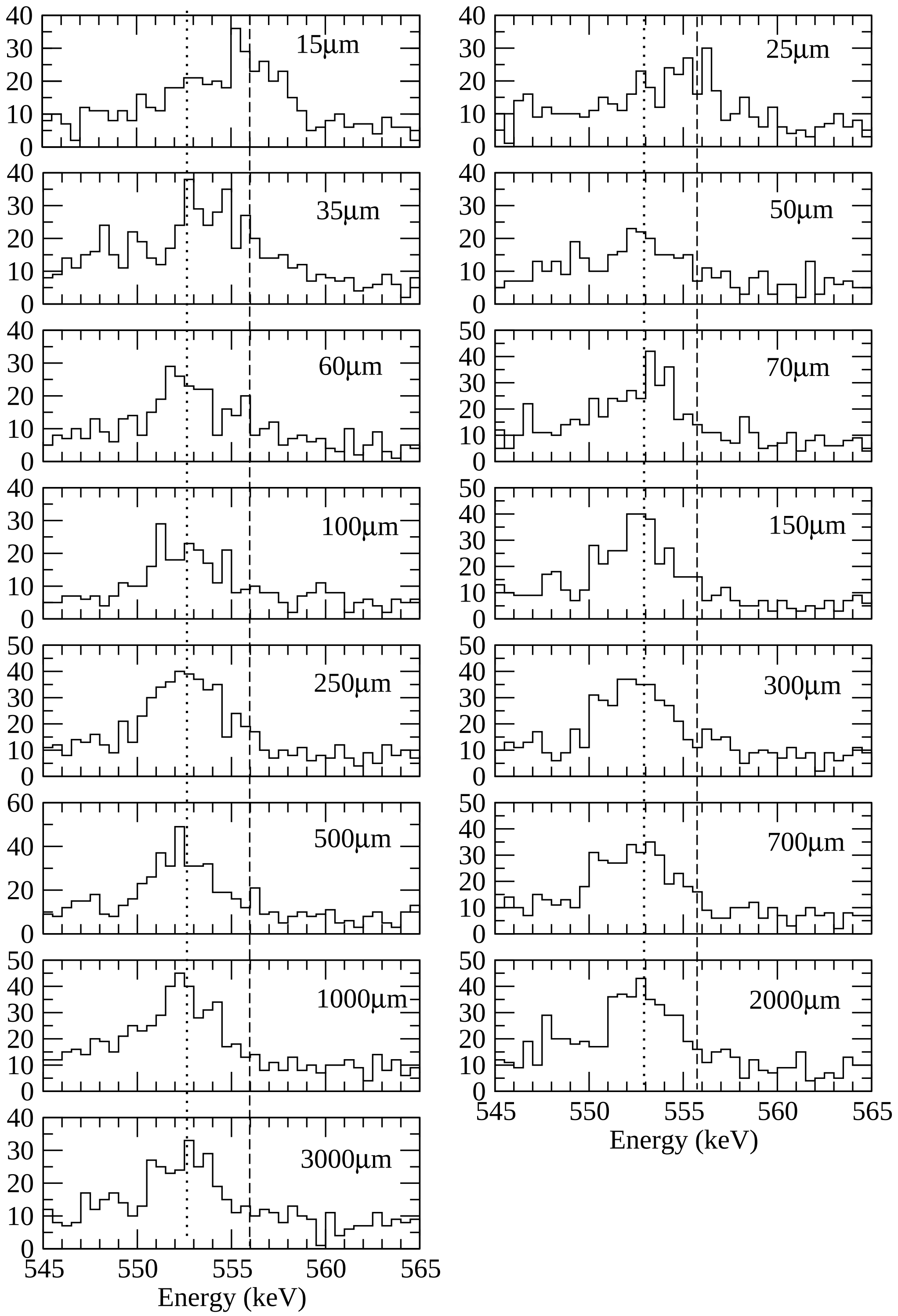

Figure A.10: Spectra showing the deconvolution of the fully Doppler shifted and degraded components of the 553.1 keV $12^+ \rightarrow 10^+$ transition, gated on the populating 611.3 keV $14^+ \rightarrow 12^+$ transition when using Ring 2 of JUROGAM. Target-to-degrader distances are listed in each panel, dashed lines indicate the degraded component whilst dotted lines indicate the fully Doppler shifted component of the transition.

553.1 keV $12^+ \rightarrow 10^+$ Transition JUROGAM Ring 2		
Distance d (μm)	Counts I_s	Counts I_d
15	94±13	159±16
25	84±13	95±13
35	138±15	101±14
50	126±13	36±10
60	145±15	44±11
70	190±16	46±11
100	143±14	30±9
150	217±18	15±10
250	256±19	31±12
300	243±18	27±13
500	240±18	26±12
700	223±17	22±10
1000	239±19	16±11
2000	239±19	15±12
3000	178±16	11±11

Table A.10: Summary of measurements of different target-to-degrader distances for the 553.1 keV $12^+ \rightarrow 10^+$ transition for RDDS measurements of ^{182}Hg. The fully Doppler shifted components, I_s and degraded components, I_d are measured with 10 JUROGAM detectors at 134.8°.